Title
DISLOCATION DIPOLES IN DEFORMED MAGNESIUM OXIDE

Author
Cass, Thomas Robert.

Publication Date
1965-11-01

UCRL-11996

University of California

Ernest O. Lawrence Radiation Laboratory

DISLOCATION DIPOLES IN DEFORMED MAGNESIUM OXIDE

Berkeley, California

DISCLAIMER

UCRL-11996

UNIVERSITY OF CALIFORNIA

Lawrence Radiation Laboratory
Berkeley, California

AEC Contract No. W-7405-eng-48

DISLOCATION DIPOLES IN DEFORMED MAGNESIUM OXIDE

Thomas Robert Cass

November 1965

DISLOCATION DIPOLES IN DEFORMED MAGNESIUM OXIDE

Thomas Robert Cass

Inorganic Materials Research Division, Lawrence Radiation Laboratory,
and Department of Mineral Technology, College of Engineering,
University of California, Berkeley, California

November 1965

ABSTRACT

The major goal of this work was to identify the microscopic processes connected with the plastic deformation of magnesium oxide by a careful study of the dislocation substructures developed during deformation. However, the application of transmission electron microscopy, the experimental technique used, was limited because no complete theory of the diffraction contrast of dislocation dipoles was available. Thus, calculations of dislocation dipole contrast were made using the Dynamical Theory of Howie and Whelan. Besides this primary application of the computations the following auxiliary topics were treated: The transition from kinematical to dynamical diffraction conditions, differentiation between a narrow dipole and a single dislocation, determination of the nature, i.e., interstitial or vacancy, of a dipole, and determination of which surface a line defect lies closer to.

In order to best utilize the results of the calculations, all experimental conditions were standardized. In particular, specimens were prepared from platelets diamond-sawed parallel to an active {110} slip plane, and observations were always made when only the {220} family of planes was responsible for the diffraction contrast. Almost all the visible damage

Chapter 2

Dislocation Configurations in Deformed Magnesium Oxide

PREFACE

This study is divided into two chapters. In the first chapter, theoretical calculations of the diffraction contrast, as observed by transmission electron microscopy, due to dislocation dipoles are presented. Further, the results of the calculations are compared with experimental observations in order to determine the reliability, applicability, and usefulness of the calculations. The second chapter contains an experimental study of the dislocation substructure developed during the deformation of magnesium oxide specimens. Since the dislocation dipole is the most prevalent form of line defect present in these specimens, use is made of the principles developed in Chapter 1 in interpreting the experimental observations. The combination of the theoretical and experimental studies yields new information on the mechanisms of dislocation dipole formation during plastic deformation.

respect to the transmitted beam. It thus became necessary to make calculations of dislocation dipole contrast using the more exact dynamical theory of Howie and Whelan[2] that takes into account absorption. With suitable values of the parameters, the theory also may be used to produce results valid for kinematical diffraction conditions, i.e., when the Bragg angle deviation parameter, W, is large.*

The first step in the calculations was to attempt to duplicate the results of single dislocation contrast obtained by previous investigators.[2] These preliminary computations served the purpose of verifying the computing techniques and also allowed a thorough familiarity to be gained with the dynamical theory. It also was expected that many properties of the images of single dislocations would apply to dislocation dipoles. Thus, bright-field (transmitted) and dark-field (diffracted) contrast profiles were calculated, under a variety of conditions, for infinitely long single screw and edge oriented dislocations lying in the plane of the thin foil.

---

* Strictly speaking, this statement is not correct because the dynamical equations still carry over absorption parameters, and the kinematical theory neglects absorption altogether. Thus, when we speak of kinematic diffraction conditions and kinematic images, we really mean dynamical theory with absorption, at large deviations from $W = 0$, as no calculations made with the kinematical theory are presented. However, the distinction is only important in certain cases, as most of the features of the kinematical theory are retained in spite of the absorption. When necessary, differences arising solely from the inclusion of absorption will be indicated.

It was of further interest to study the transition from dynamical to kinematical diffraction conditions, i.e., the change of dislocation images as W is increased. Great use has been made of the kinematical theory of diffraction contrast of Hirsch, Howie, and Whelan[1] in interpreting dislocation substructures. This theory is developed under the assumption that the transmitted beam is dominant in the crystal and that the intensity of the diffracted beam is always small with respect to it. Because of this fact, consideration of the local lattice curvature at a dislocation enables one to predict at which side of the actual position of the dislocation its image will occur. In the dynamical theory with W = 0, the side at which the image occurs and the distance the image is displaced from the dislocation is a function of the depth of the dislocation in the thin foil. In the kinematical theory the image also occurs to one side of the dislocation, but the image position is only a function of the deviation from the Bragg angle and is not a function of the dislocation depth. The depth independent one-sided nature of dislocation contrast in the kinematical approximation has been used to determine the sense of bending introduced by an edge dislocation in a thin foil,[4] the side of the slip plane which contains the extra half plane of an edge dislocation,[5] the nature of loops formed by the annealing of dislocation substructures in magnesium oxide,[6] the nature of fission irradiation loops in platinum,[7] and the nature of loops in alpha-particle bombarded aluminum.[8] All the aforementioned works assumed the reliability of the "kinematical theorem" which states that, irrespective of a dislocations depth, its image lies on the side of the dislocation at which $\underset{\sim}{g} \cdot \underset{\sim}{R}$ is of opposite sign to $S_g Z$ where $\underset{\sim}{g}$ is the reciprocal lattice vector associated with the diffracting plane, $\underset{\sim}{R}$ is the displacement vector of the dislocation

strain field, S_g is the magnitude of the deviation parameter in the reciprocal lattice (and is proportional to the dynamical deviation parameter W), and Z is the depth coordinate in the thin foil with origin at the dislocation. Physically, the kinematical theorem states that, in a crystal not at the Bragg angle, the image of a lattice defect will occur on that side of its actual position where the lattice tilts caused by the defect locally bring the lattice closer to the Bragg angle. Although the kinematical theory is not quantitatively valid until $W \geq 3$,[9] the determination of the value of W for which the kinematical theorem of depth independent one-sided contrast becomes valid was deemed worthwhile.

For the screw dislocation case, two strain fields derived from linear elasticity theory were used. The first corresponded to the strain field of a screw dislocation in an infinite medium,[10] the second corresponded to that of a screw dislocation in a thin plate[11] with an infinite series of images and was exact. The infinite medium strain field[10] alone, and with a single image were used in the edge dislocation case. The exact strain field of an edge dislocation in a thin plate is not obtainable in closed form,[12] but it has been shown that the presence of the dislocation produces a bending which is a maximum when the dislocation is at the exact center of the plate.[13] The induced bending only has the effect of causing a discontinuity in the background intensity on alternate sides of the dislocation core,[4] but does not affect the other features of the contrast. This bending is not reproduced by the simplified treatment used in these calculations for single edge dislocations.

Edge dislocation dipole images were calculated using infinite medium strain fields plus simple images for each component dislocation. In the dipole case, this approximation is certainly more valid than in

the single dislocation case because the lattice bending discussed above is restricted to the interior of the dipole, and essentially is cancelled outside either of the dislocations of the dipole. The effect of dipole spacing, depth of the dipole in the foil, deviation from the Bragg angle, and value of $\underset{\sim}{g} \cdot \underset{\sim}{b}$ were all considered. During the course of the dipole contrast study, it was noted that the strain field of a narrow dipole approximates to that of an included platelet. Hence, the strain contrast theory of Ashby and Brown[14] was investigated to see what similarities existed between images of narrow dipoles and those of included strain centers.

Details of Calculations

The two-beam dynamical equations of diffraction contrast in a deformed lattice may be written in the form:[2]

$$\frac{dT'}{dZ} = \frac{-\pi}{\xi_0'} T' + \pi \left(\frac{i}{\xi_g} - \frac{1}{\xi_g'} \right) S' \qquad (1)$$

$$\frac{dS'}{dZ} = \pi \left(\frac{i}{\xi_g} - \frac{1}{\xi_g'} \right) T' + \left\{ \frac{-\pi}{\xi_0'} + 2\pi i (S_g + N\beta) \right\} S' \qquad (2)$$

ξ_0' determines the mean (uniform mode) absorption coefficient which is $\frac{2\pi}{\xi_0'}$. ξ_g is the extinction distance and is twice the distance in which the transmitted beam loses all its intensity to the diffracted beam in a crystal oriented exactly at the Bragg angle. (For a discussion, see Heidenreich.[15]) ξ_g' is, by analogy, the absorption distance which phenomenologically characterizes localized (anomalous) absorption processes. S_g is a parameter proportional to the deviation from the Bragg angle, and is related to W by $W = S_g \xi_g$, and N is equal to $\underset{\sim}{g} \cdot \underset{\sim}{b}$, usually 1 or 2. Finally, β^* describes the strain field of the deformed

---

* As defined by Howie and Whelan, the strain field parameter β'_{HW} was equal to $\frac{d}{dZ}(\underset{\sim}{g} \cdot \underset{\sim}{R}(Z))$. In the present notation, however, $N\beta = \beta'_{HW}$.

lattice and is the derivative with respect to depth of the lateral displacement field of the defect. The direction of the positive Z-axis was taken parallel to and in the direction of travel of the electron beam, assuming that it impinges perpendicular to the plane of the thin foil. The positive X-axis was taken to lie perpendicular to the Z-axis, and pointing towards the right. The diffraction vector $\underset{\sim}{g}$ was taken parallel to the positive X-axis for edge dislocations and pointing into the plane of the figure for screw dislocations. In any case where β is not constant, the equations must be numerically integrated from the top surface of the foil ($Z = 0$) to the bottom surface ($Z = D$). The observable quantities, $|T'|^2$ and $|S'|^2$, the transmitted and diffracted intensities, respectively, are then computed from the amplitudes T' and S' at the lower surfaces.

An IBM 7094 was used to numerically integrate the dynamical equations. It was convenient to separate the original equations into their real and imaginary parts, yielding four linear simultaneous differential equations. Starting with the boundary condition real part of $T' = 1$, and imaginary part of $T' = |S'| = 0$, the numerical integration was done by the fourth-order Adams-Moulton Method with a variable step size, utilizing the Runge-Kutla Method for the starting process. The SHARE routine, D2 RW INT was used for this integration; the mathematical formulation is described in the SHARE abstract.[16]

The functions describing the strain fields, the β functions, depend on the position of the defect they represent. The position of single dislocations was always taken as $X = 0$, $Z = \eta$; the same position was used for the geometric center of dipoles. Two dipoles orientations were studied. In the first, the component dislocations were immediately

above one another. The second orientation was the equilibrium configuration for edge dislocations, i.e., the dislocations were at 45° to each other, with the left-hand dislocation always further from the upper surface than the right-hand dislocation. The W = 0 (exact Bragg angle) images of dipoles of the alternate equilibrium configuration can always be deduced from the computed images by reflecting the abscissa, i.e., by letting $X \rightarrow -X$. The β functions, which are the vertical derivatives, $\frac{\partial R_X(X,Z)}{\partial Z}$, of the lateral displacement functions depend on both Z and X. The dynamical Eqs. (1) and (2) are derived under the assumption that X may be considered as a parameter. Thus, the numerical integration was carried out by letting Z range through its values (0 to D) while holding X constant. The integration then yields $T'(X_i)$ and $S'(X_i)$. About 60 values of the parameter X_i were used to produce one set of intensity profiles ($|T'|^2$ or $|S'|^2$ vs. X); the lateral limits on X were $\pm\xi_g$. ΔX_{ij}, the spacing of the X_i's was taken smaller near the center of the dislocation since the intensities varied more rapidly there as a result of the larger absolute values of β.

Because of the possible erroneous values of $|T'|^2$ and $|S'|^2$ that could arise near a dislocation core due to the large values of $|\beta|$ there, a criterion was needed to determine whether the calculated results were accurate. It was noted that if the lower limit of the variable numerical integration step size, ΔZ, was made too large, the intensity profiles would often be discontinuous in the vicinity of the dislocation core. As a practical solution, the step size was decreased until a further decrease no longer produced a change in the image profile. In this sense, the calculated curves are free from numerical integration errors, as they represent the transmitted and diffracted intensities in

the limit of infinitely small numerical integration step size. Also, the numerical integrations were never carried out any closer than 2 Burgers vectors from the core of the dislocation; the curves were simply interpolated across the origin. This technique avoided the $\frac{1}{r}$ divergence in the strain field at the core of the dislocation.

The aforementioned treatment of X as a parameter is known as the column approximation.[2] This assumption means that $\frac{\partial R_X(X,Z)}{\partial X}\Big/_Z \approx 0$ across a narrow column whose dimensions are wide enough to contain all the transmitted and diffracted beams that contribute intensity to the point $X = X_i$, $Z = D$, on the bottom surface of the thin foil. In addition, the two beams are considered approximately plane so that $\frac{\partial R_X(X,Z)}{\partial Z}$ is small. In the dynamical theory, then, the column is parallel to the diffracting planes. Because of the repetitive intensity interchange that results from dynamical interaction, neither beam travels very far laterally. When a crystal of magnesium oxide is oriented exactly at the Bragg angle for diffraction of 100 KV electrons from the {220} planes, a column width of about 6Å is sufficient to contain the lateral excursions of the two beams. Thus, for purposes of calculation, the continuously deformed crystal has been divided into narrow columns. Each column is assumed to have the diffracting properties of a crystal of infinite lateral extent composed of extremely thin slabs, perpendicular to the electron beam, with each slab displaced laterally from its neighbors. Inside each slab, i.e., for a certain value of Z, there is no lateral variation of the displacement function, $R_X(X,Z)$. However, $R_X(X,Z)$ is allowed to vary as Z varies, i.e., as we pass vertically from a given slab to the one below it. The width of the numerical integration step, ΔZ, determines the practical width of thin slabs assumed, since only

one value of Z per slab is desired.

In all cases, both the Burgers vector and the dislocation lay parallel to the plane of the foil. Contrast profiles were calculated for several strain functions. The exact formulae for the β's are given in Appendix I, and an explanatory list is given in Table I.

Because all experimental observations were carried out under controlled conditions, selected values of the parameters occurring in the dynamical equations were used. For convenience, the fundamental unit of length was chosen as a Burgers vector. Poisson's ratio was taken as $\gamma = 0.18$.[17] Magnesium oxide extinction distances were calculated at 100 KV from the tables in Thomas:[18] $\xi_{200} = 186\ \underset{\sim}{b}$, $\xi_{220} = 254\ \underset{\sim}{b}$, $\xi_{222} = 376\ \underset{\sim}{b}$. The {220} reflection was chosen as a standard because it was the lowest order strong reflection available in the specimen geometry to which the calculations were to be compared. The foil thickness was standardized at 6 extinction distances, which is a typical value. Foil thickness has little effect on the calculations as long as it is sufficiently large for anomalous absorption effects to be important. A value of $\frac{\xi_g}{\xi_0'} = 0.157$ was adopted; this figure was obtained from the measurements of ξ_0' and ξ'_g for {200} beams by Watanabe et al.[19] The value of ξ_0' obtained experimentally should, in principle, be independent of the diffracting plane utilized in measuring it. There were no data for ξ'_g at 100 KV in the {220} case. Therefore, the {200} value was assumed, and it yielded $\frac{\xi_g}{\xi_g'} = 0.113$. Thus, instead of the usual assumption of $\frac{\xi_0'}{\xi_g'} = 1$, we have $\frac{\xi_0'}{\xi_g'} = 0.71$. By taking the value of ξ_g' for {200}, the amount of anomalous absorption present when using a {220} beam has been overestimated.

Table I Description of Strain Fields Studied

Strain Field	Boundary Conditions
β_1 (X, Z, η) screw dislocation	infinite body
β_2 (X, Z, η) screw dislocation	thin plate (exact)
$\beta_3 = \beta_2(X+X_0, Z, \eta+X_0) - \beta_2(X-X_0, Z, \eta-X_0)$ screw dislocation dipole center of dipole at (0, n), component dislocations at $(-X_0, \eta+X_0)$ and $(X_0, \eta-X_0)$	thin plate (exact)
β_4 (X, Z, η) edge dislocation	infinite body
β_7 (X, Z, η) edge dislocation	infinite body plus simple image across surface Z=0; shear stress is zero at Z=0; normal stress $\neq$ 0
$\beta_8 = \beta_7(X+X_0, Z, \eta+X_0) - \beta_7(X-X_0, Z, \eta-X_0)$ edge dislocation dipole equilibrium configuration: center of dipole at (0, η), component dislocations at $(-X_0, \eta+X_0)$ and $(X_0, \eta-X_0)$	infinite body plus simple image across surface Z=0; shear stress is zero at Z=0; normal stress $\neq$ 0
β_{10} (X, Z, η, D) edge dislocation	infinite body plus simple image across surface Z=D; shear stress is zero at Z=D; normal stress $\neq$ 0
$\beta_{11} = \beta_{10}(X+X_0, Z, \eta+X_0, D) - \beta_{10}(X-X_0, Z, \eta-X_0, D)$ edge dislocation dipole equilibrium configuration: center of dipole at (0, η), component dislocations at $(-X_0, n+X_0)$ and $(X_0, \eta-X_0)$	infinite body plus simple image across surface Z=D; shear stress is zero at Z=D; normal stress $\neq$ 0

Table I (continued)

Strain Field	Boundary Condition
$\beta_{12} = \beta_7(X, Z, \eta + X_0) - \beta_7(X, Z, \eta - X_0)$ edge dislocation dipole centered at $(0, \eta)$ with component dislocations at $(0, \eta + X_0)$ and $(0, \eta - X_0)$, one exactly above the other	infinite body plus simple image across surface Z=0; shear stress is zero at Z=0; normal stress $\neq 0$
$\beta_{13} = \beta_{10}(X, Z, \eta + X_0, D) - \beta_{10}(X, Z, \eta - X_0, D)$ edge dislocation dipole centered at $(0, \eta)$ with component dislocations at $(0, \eta + X_0)$ and $(0, \eta - X_0)$, one exactly above the other	infinite body plus simple image across surface Z=D; shear stress is zero at Z=D; normal stress $\neq 0$

Results of Calculations

It is to be expected that many properties of the images of single dislocations will also apply to dislocation dipoles. It is therefore desirable to consider first the calculated intensity profiles for single dislocations.

I Single Dislocation Images

Figure I illustrates several features of single dislocation images. The intensity ordinates are identical in these and all subsequent contrast profiles. The dislocation line is normal to the plane of the figure; the plots extend to an extinction distance on either side of the dislocation core, i.e., ± 254 Burgers vectors. The horizontal line that is approached by the intensity function is the background intensity, i.e., the intensity observed in perfect crystal. All profiles in Fig. 1 are bright-field images for the N = 1 case. As illustrated by Fig. 1(a), the width of a screw dislocation lying near a surface (one-half extinction distance from the upper surface in this case) is considerably decreased if the strain field is treated exactly. However, the tail of the contrast function is apparently the only part affected by the presence of images, as the two strain fields yield equivalent results near the center of the dislocation. Close examination of the two strain field formulae, β_1, and β_2 shows that they approach the same limit as X becomes small, so this behavior is not surprising.

Figure 1(b) is a contrast profile of an edge dislocation at the same depth in the foil as the screw dislocation in Fig. 1(a), under the same diffracting conditions, i.e., W = 0. The greater width of the edge dislocation image is apparent.[2] The conditions producing Fig. 1(c) are identical to those of Fig. 1(b) with the exception that

the crystal is deviated slightly from the Bragg angle, such that W = 1. It is important to notice that in deviating the crystal from the Bragg angle the apparent position of the dislocation changes from one side of the dislocation core to the other. This effect will be discussed in more detail later, when the N = 2 case is described. The intensity profile in Fig. 1(c) indicates that the region to the right of the dislocation would appear darker than the left-hand region. This effect is a general one for single dislocation images in crystals slightly deviated from the Bragg angle. The contrast difference is not associated with the bending of the foil caused by the edge dislocation, as can be seen from the following three facts. First, the amount of bending introduced, and hence the intensity difference, goes to zero as the dislocation position approaches the surface. Therefore there should be very little bending introduced by an edge dislocation one-half extinction distance from the surface. Second, no bending is involved in the infinite body plus single image approximation to the edge dislocation strain field used in the present calculations. Finally, the effect also occurs in the intensity profiles of screw dislocations, for which there is no possibility of bending.

Figures 1(d) and (e) and 1(f) and (g) are two sets of screw and edge dislocation profiles for W = 0, at depths of 2.75 and 3.0 extinction distances in the foil, respectively. The greater width of the edge dislocation images is thus also apparent in the central regions of the foil.

Figure 2 illustrates the change of apparent position and intensity in the bright-field image (N=2) of an edge dislocation one-half extinction distance from the top surface as the deviation from the exact Bragg angle

bright- and dark-field images; it also causes the strength of bright- and dark-field images to be dependent not only on the value of W, but also its sign.

II Edge Dislocation Dipole Images

No attempt was made to subdivide the section on single dislocation images because of the interdependency of the variables that affect diffraction contrast. The same interrelations exist in this section, but its greater length requires that some subdivision be made.

II-1 Kinematical Dipole Contrast

Before discussing the results of the present calculations for edge dislocation dipoles, the main features of Wilkens' kinematical dipole contrast calculations[3] will be described. In the kinematical approximation the image of a dislocation lies to one side of the actual position of the dislocation. Under otherwise identical imaging conditions, dislocations of opposite sign will have their images on opposite sides. Thus, the images of the component dislocations will either be both inside or both outside the dipole. Wilkens calculated the kinematical scattered intensity of both types of dipole image as a function of the parameter $2X_0W$,* where W is the deviation parameter and $2X_0$ the horizontal spacing of the dipole in units of extinction lengths. For outside contrast, he found that, as $2X_0W$ decreased, the diffracted intensity decreased continuously from the value representative of an isolated dislocation. In the case of

---

* Wilkens actually considered the parameter $2X_0S_g$. In order to use W throughout this work, his parameter has been converted to the present one by taking X_0 in units of ξ_g, so that $2X_0\xi_g = 2\left(\frac{X}{\xi_g}\right)(\xi_g S_g) = 2X_0'W$.

inside contrast, however, the scattered intensity initially increased as the parameter $2X_0W$ decreased. Eventually, a strong single maximum occurred at $2X_0W = 0.5$; then the diffracted intensity decreased for smaller values. Wilkens presented no data for values of $2X_0W$ less than 0.25, because according to the kinematical approximation, the diffracted intensities became quite low at that point. Thus, his results are restricted in the sense that if the images of very narrow dipoles were desired, they could only be obtained accurately at large deviations from the Bragg angle; conversely if images at smaller deviations were required, they only could be calculated for dipoles of rather large spacing. Also, Wilkens used strain fields of screw dislocations; as has been shown, edge dislocations have considerably wider images than do screw dislocations and hence conceivably could interact over a wider range of dipole spacings. In order to further simplify the calculations, Wilkens limited his calculations to $|N| = 2$ and treated only a dipole exactly at the foil center. Thus, there remained several important questions to be answered by the dynamical calculations of dipole contrast. The following parameters were accordingly studied: position of the dipole in the foil, spacing of the dipole, amount of deviation from the Bragg angle, value of N.

II-2 Dynamical Dipole Contrast

The present calculations are limited in that they treat only the range of dipole spacings in which there is a strong interaction between the strain fields of the component dislocations. That is to say, we are not interested in dipoles of such large spacing that their contrast can be predicted entirely from the relevant calculations for single dislocations.

II-2.1 Depth Symmetry Properties

There are certain symmetry relations which hold for images of defects in crystals oriented exactly at the Bragg angle; these relations have been deduced from the dynamical theory for bright-field[2] and dark-field[20] images. Briefly, there are two classes of defects grouped according to their displacements and lattice tilts. In the first group, the bright-field image is the same whether the defect lies at a depth η or D-η, where D is the foil thickness. Included in this group are screw dislocations in the plane of the foil and edge dislocations in the plane of the foil whose Burgers vector also lies therein (compare Fig. 4(c) and (h)). The dark-field images for these positions are reflections of each other in the plane formed by the dislocation and a line drawn normal to the foil surface. To the second group belong edge dislocations lying in the plane of the foil with Burgers vector perpendicular to the foil surface, spherical inclusions, and planar inclusions whose major strain axis lies in the plane parallel to the foil surface. Here, the dark-field image is identical for defects at η or D-η. Conversely, the bright-field images at these positions are reflections of each other. Calculations show that the strain field of a dipole of narrow spacing approximates to that of a planar inclusion, at least as far as the symmetry properties of the dynamical equations are concerned. Figure 6 illustrates the symmetry principles described above. The upper four profiles are for a single edge dislocation (extra half-plane down) at depths of 1 and 5 extinction distances in a foil 6 extinction distances thick. The lower four curves are for a vacancy edge dislocation dipole centered at the same depths. The two component dislocations are exactly above each other and are separated by 20 Burgers vectors. The same symmetry properties are valid

if the two edge dislocations are taken in their equilibrium configurations, i.e., at 45° to each other; in this case, however, the curves are not quantitatively identical. In all that follows, we shall describe results for edge dislocation dipoles in the equilibrium configuration, realizing that these results will also be qualitatively valid for the other dipole configuration.

II-2.2 Effect of Dipole Depth

Figures 7 and 8 are the bright- and dark-field images ($|N| = 2$) for a vacancy edge dislocation dipole of 20 Burgers spacing ($X_0 = 10\underset{\sim}{b}$) at various depths in a crystal oriented at the exact Bragg angle. Figures 9 and 10 are images for an interstitial edge dislocation dipole, with all other conditions unchanged from the above. Figures 7(c) and (h), and 8(c) and (h) show the depth symmetry properties previously described. At $W = 0$, the distinctive difference in apparent widths, i.e., inside and outside contrast, present under kinematical conditions, does not occur. Narrow dipoles such as these also show alternating contrast, similar to that observed with single dislocations (Fig. 4). The strongest black-white image is at a depth of one-half extinction distance. Intensities of the black-white image are weaker for dipoles further from the surface. The symmetry of the strongest black-white image is such that, in dark-field at $W = 0$, the black side is towards positive $\underset{\sim}{g}$ for vacancy dipoles; the white side is towards positive $\underset{\sim}{g}$ for interstitial dipoles. The rule is exactly the reverse of that described by Ashby and Brown,[14] but the reason for the difference is easily understood. Ashby and Brown treated dark-field images of loops that actually intersected the foil surface. Thus, their computed profiles were really those of single edge dislocations (see Fig. 12 of Ashby and Brown[14]). For

example, an interstitial loop intersecting the upper surface of a foil can be represented by a single edge dislocation near that surface, with its extra half-plane closer to the upper surface. If the interstitial loop intersects the lower surface, the sign of the dislocation is reversed and the extra half-plane is towards the lower surface. It can be deduced from Fig. 6 that both these configurations have the same black-white orientations, irrespective of which surface is intersected by the loop. As the position of the single dislocation representing the loop comes closer than about one-quarter of an extinction distance from the surface, an intense black-white image ("anomalously" wide image) results. Ashby and Brown suggested that loops and inclusions intersecting the surface could be detected by the presence of an anomalously wide image; the criterion of the image orientation could then be applied to determine the nature of the loop or inclusion. In the dipole case, because both dislocations are in the foil, it is not the innermost dislocation that determines the black-white orientation, but rather the dislocation nearest the surface. For any dipole, this latter dislocation has opposite sign and hence opposite diffracting properties than the single dislocation that would represent the dipole contrast if the dipole intersected the surface. Also note that as the dipole nears the surface, there is no anomalously wide black-white image, but rather one that gradually diminishes in intensity as the surface is approached. Although one could, in principle, determine the nature of a dipole lying very close to the surface, it is considered more reliable to study thin sections in which dipoles intersect a surface at a very small angle, such as sections prepared parallel to an active slip plane. Because there will be difference in length of the component dislocations of a dipole intersecting a surface, the innermost

dislocation can easily be selected and the Ashby-Brown criterion applied to it. This possibility will be discussed further in the experimental section.

II-2.3 Transition to Depth-Independent One-Sided Contrast

Figures 11 and 12 are dipole images under similar conditions to those occurring in Figs. 7 and 9, respectively, except for the fact that these images are representative of a crystal deviated from the Bragg angle such that W = 1. The dark-field profiles (not shown) are similar but of a lower intensity. In Fig. 11, the configuration of the vacancy dipole is such that outside contrast is obtained, i.e., the respective images of the dislocations lie outside the actual positions of the dislocations. The interstitial dipole images in Fig. 12 exhibit inside contrast. The complex variation of the W = 1 dipole images with depth is not important. The chief feature is that a deviation as small as W = 1 gives the inside and outside contrast behavior calculated by Wilkens[3] from the kinematical theory. It should be further noted that Figs. 11 and 12 represent values of the product $2X_0W$ equal to 0.08, whereas Wilkens presented curves for values down to only 0.25. According to his calculations, the diffracted intensity should be almost zero at 0.08. The images in Fig. 12 would all appear as a single dark line. The images in Fig. 11 show that, in principle, the dipole should appear as two fainter dark lines; whether or not the region of increased transmission between the two images would in fact be resolvable cannot be decided on the basis of these calculations alone, as other experimental conditions would be the determining factors.

II-2.4 Effect of Dipole Spacing

It is necessary to note that there are depth positions of the dipole for which the image is either symmetric or asymmetric (see Figs. 7

through 11). Only the symmetric image case shall be discussed in detail. From the properties of images of single dislocations located at equal distances from the foil center (see Fig. 6), dipoles whose geometrical center coincides with the foil center should have symmetrical bright-field images and asymmetrical dark-field images. This is indeed the calculated result, as can be seen in Fig. 13, which shows the N = 1 dynamical images of vacancy edge dislocation dipoles of 10, 20, and 50 Burgers vectors spacing situated at the foil center. If the dipole is moved $\frac{1}{4}\xi_g$ from the foil center, the bright-field image becomes asymmetric and the dark-field symmetric (see Figs. 7 through 11). The bright-field profiles for an interstitial dipole under the conditions of Fig. 13 are identical to the vacancy profiles for the two narrower dipoles and almost identical for the widest dipole; the dark-field profiles have reversed asymmetry, i.e., they are reflections of the vacancy dark-field profiles about the line X = 0. Figure 14 presents results for the N = 2 case, and is otherwise analogous to Fig. 13 except that an additional set of profiles, corresponding to a dipole with a spacing of 100 Burgers vectors has been included. Figures 15 and 16 are bright- and dark-field profiles, for the N = 2 case, of centrally located interstitial edge dislocation dipoles of spacings, $2X_0$, 6, 10, 20, 40, 50, 60, and 100 Burgers vectors.

Several statements can be made on the basis of the calculations presented in Figs. 13 through 16. The images of vacancy and interstitial dipoles of the same spacing and located at the foil center essentially are identical in the limit of narrow dipole spacings for both N = 1 and N = 2. By a spacing of 50 Burgers vectors, a slight difference in apparent width of these two kinds of dipole becomes noticeable. This width difference is associated with the onset of

independent image properties of the two component dislocations of the dipole. Also, for all spacings, the contrast in the region in the interior of the dipole differs slightly between vacancy and interstitial types for the N = 2 case. However, this latter difference probably is not experimentally observable. Thus, when observed under dynamical conditions, narrow dipoles do not exhibit inside or outside contrast. Because this is true, the way in which a dynamical image of a narrow dipole changes as the dipole spacing decreases depends only upon whether the image is symmetrical or asymmetrical, i.e., only on its depth in foil. It does not depend, as Wilkens found for kinematical images, on whether the dipole exhibits inside or outside contrast, as this distinction does not exist for dynamical images of narrow dipoles.

As the dipole spacing decreases, there is a difference in behavior of the intensity minima of symmetric dynamical images according to whether N = 1 or N = 2. For N = 1, the depth of the intensity minima continuously decrease, with decreasing dipole spacing, from that of an isolated single dislocation at the same depth. For N = 2, as the dipole spacing decreases, the depth of intensity minima first increases above that of an isolated single dislocation, reaches an extreme value at about 40 to 50 Burgers vectors spacing, then continuously decreases. It is expected that asymmetrical images, consisting of a strong and a weak intensity minima, behave similarly to symmetric images. The primary difference is that, as the dipole spacing increases, the strong image returns to the intensity representative of an isolated single dislocation first, followed by the weak image.

Because images formed with N = 2 reflections are more intense at all spacings less than about 50 Burgers vectors, utilization of N = 2

rather than N = 1 reflections is more favorable for imaging dipoles in the limit of decreasing dipole spacing. On the basis of the calculated curves it is estimated that at W = 0, a centrally located dipole of 10 Burgers vectors spacing should just be visible for N = 1; for N = 2, the value is 6 Burgers vectors. These values do not hold for a dipole lying very close to a surface. Figures 17 and 18 illustrate the effect of dipole spacing for a vacancy or interstitial dipole, respectively, lying $\frac{1}{2}\xi_g$ from the upper surface. The left-hand column is calculated for W = 0, the right-hand column for W = 1.0. Only bright-field images are included because, in the former case, the dark-field images are identical to those shown and, in the latter case, the dark-field images are very weak. The W = 1.0 curves represent values of the parameter $2X_0W$ = 0.04, 0.08, and 0.2 respectively. It is difficult to imagine the W = 1.0 image Fig. 18(c) increasing in intensity, although according to Wilkens, if W = 2.0, the diffracted intensity would quadruple. It is obvious, however, that in the limit of narrow dipole spacings, inside contrast should be more visible than outside contrast. The curves also show that at a dipole spacing as large as 50 Burgers vectors, for N = 2, inside contrast produces an intense single image, while outside contrast yields a resolvable pair of images. Finally, the strongly asymmetric W = 0 vacancy and interstitial images are similar only at the narrowest dipole spacings because of the proximity of the surface.

II-2.5 Effect of Bragg Angle Deviation on Dark-Field Images

The discussion of the dipole calculations will be concluded with a consideration of the effect of Bragg angle deviation on the computed dipole images. This segment of the calculations is particularly relevant to any discussion of Ashby-Brown techniques, because it has

always been assumed that the validity of the technique was unaffected by a small deviation from the Bragg angle. Because of the greater utility of dark-field observations for investigating strain contrast, and the fact that the contrast produced by deviations of equal magnitude but opposite sense can only be compared in dark-field, we shall restrict ourselves to this mode of operation. Concerning bright-field images it is sufficient to note that they always became very weak if the deviation from the Bragg angle becomes significantly negative. This point is illustrated in Fig. 19, which portrays images of an interstitial dipole of 10 Burgers vector spacing at a depth of 1 extinction distance from the upper foil surface. Both the bright-field background intensity and the bright-field image intensity decrease as W becomes increasingly negative. The lower graphs, Fig. 19(e) represent the deviation of W = -0.50. The dark-field background intensity is the same at either ±W, whatever the value of W; however, it can be seen from Fig. 19 that the dark-field image intensity is stronger for W negative than for W positive. This property is a general one for defects near the upper surface of a foil, and was noted previously in connection with the single dislocation images in Fig. 3. If the deviation is changed to W = -1.0, a reversal of the black-white orientation occurs in the dark-field images. Figure 20 shows the reversal for an interstitial dipole of 20 Burgers vectors spacing. The left column is for the dipole at a depth of one-half extinction distance; the right column is for a depth of 1 extinction distance. The values of W are -1.0 for the upper row, 0 for the middle row and 1.0 for the lower row. The W = 1.0 images would be essentially invisible in dark-field, but the W = -1.0 images would appear bright. Note also that if the dipole is at a depth of one-half extinction

distance, the white image does not change sides as the crystal is deviated in the direction of negative W. Thus we obtain a sort of kinematical one-sided image, if the Bragg angle deviation is large enough. This behavior is analogous to the transition from alternating to one-sided contrast that occurs for both single dislocations and narrow dipoles in bright field. Dipoles and single dislocations at depths greater than 1 extinction distance display increasingly weaker white images. Figure 21 shows the calculated dark-field images of a vacancy dipole of 20 Burgers vectors spacing. The images for W = -1.0 are not simple black-white images. Thus, no attempt will be made at formulating a general rule about the shift of a black-white strain image. We shall only remark that there are defect depths near the foil surface where a dark-field black-white image orientation may reverse itself as the deviation from the Bragg angle is increased. It is true, however, that due to the decreased background intensity at W = -1.0, the reversed image would probably appear almost completely white, rather than black-white.

Figures 20 and 21, with some modification, also are valid for dipoles near the lower surface of a thin foil. Let the left and right columns of each figure represent depths of one-half and 1 extinction distances from the lower surface. Calculations made for single dislocations and dipoles at these positions show that the white image persists for W positive and disappears for W negative. The upper row in these figures now represents W = 1.0, the middle row, W = 0, and the lower row, W = -1.0. The calculations also show that Figs. 20 and 21 are exactly identical to the images of vacancy and interstitial dipoles, respectively, at the depths mentioned, if the images are reflected about X = 0, i.e., $X \rightarrow -X$. The same results holds for the dipole orientation

with the component dislocations one above the other.

We may conclude two facts about dark-field images. First, for $|W| \geq 1$, defects near the upper surface are imaged strongly only for W negative, and defects near the lower surface only for W positive. Kinematical theory without absorption predicts that images should be of equal intensity for a given value of W, irrespective of the sense of the deviation. Because the values of W are large enough so that the kinematical theory should otherwise reproduce, at least qualitatively, the same features as the dynamical theory, it is essential to ascribe the difference in calculated results to the one factor that the dynamical equations alone take into account, namely anomalous absorption.

Second, the dark-field image of a vacancy (interstitial) dipole at a depth η in a foil of thickness D at a Bragg angle deviation -W, is the reflection ($X \rightarrow -X$) of the image of an interstitial (vacancy) dipole of the same orientation at $D-\eta$ with the Bragg angle deviation +W. This rule is a generalization of the W = 0 symmetry law described previously and illustrated by Fig. 6. Figures 8(h) and 10(c) representing the equilibrium dipole orientation, are further examples. The analogous bright-field symmetry law is that the image of a dipole at η, in a crystal with Bragg angle deviation parameter, W, is the reflection ($X \rightarrow -X$) of the image of the same dipole at $D-\eta$, where D is the foil thickness.

The occurrence of image depth symmetry properties for crystals not at the Bragg angle is somewhat unexpected, but not unreasonable. Similar relations hold for single defects, but these are simpler since the important lattice tilts (β functions) are usually either even or odd functions. In the case of an edge dipole in the equilibrium orientation, the β function is neither pure odd nor pure even over all its domain, so

that the symmetry relations are more complicated.

Comparison of Calculations with Experimentally Observable Images

In the preceding section, the results of calculations were presented without regard to possible application. In this section, however, there are two definite goals: first, to establish the reliability of the calculations, and second, to point-up useful applications that may be derived from them.

In order to attain the first goal, it was necessary to standardize not only the parameters of the dynamical equations, but also all experimental conditions that could possibly cause ambiguous interpretations. Single crystal specimens were prepared from {110} slip plane sections that had been diamond-sawed from deformed magnesium oxide crystals (see Chapter 2 for details of specimen preparation). The change in the image of a line defect with depth in a thin foil occurs very gradually in the slip plane section geometry because the defects are almost parallel to the foil surface. This feature simplifies the correlation of experiment with theory. During examination in the electron microscope, the specimens were always oriented such that the {220} planes were the only strongly diffracting planes; thus, a "two-beam" situation for which $g \cdot b = 2$ always obtained.

Before considering possible applications, we must first list the important features of kinematical or dynamical images. Then we shall treat such questions as how to distinguish between a single dislocation and a narrow dipole, how to determine the nature of a dipole and how to determine which surface a line defect lies closer to.

I. Kinematical Diffraction Conditions

When looking at the general features of a dislocation substructure,

it is preferable to work in bright field with $W \approx 1$. In this way, the transmitted intensity is maximized;[2] also, resolution is increased because of the smaller kinematical image widths relative to dynamical images. Finally, one is then able to apply confidently the kinematical theorem of one-sided contrast. As an example, Fig. 22 shows a long wide dipole in a crystal deformed at 1000°C. By changing the sense of the diffraction vector, the dipole contrast changes from inside to outside. Close examination of the component images shows another feature predicted by the kinematical theory[1] when $g \cdot b = 2$, and observed for $W \geq 1$. The image profiles are not symmetric, but have a rather diffuse tail on one side. The diffuse side of the image is always on the side away from the actual dislocation position. This property permits one to differentiate between inside and outside contrast if only one micrograph is available, provided the component dislocations are resolved.

There are two equilibrium configurations for edge and near edge orientation dipoles and there are two types of dipole, vacancy and interstitial, making a total of four possibilities. Determination of whether the dipole is outside or inside contrast and correlating that fact with the sense of the diffraction vector allows one to eliminate two of the four possibilities. Unfortunately, of the two remaining choices, one will always be a vacancy dipole and the other an interstitial one. Thus, the <u>type</u> of dipole cannot be determined from the knowledge of whether the dipole is in outside or inside contrast alone.

II Dynamical Diffraction Conditions

As convenient as bright-field observations are to make, dark-field observations at $W = 0$ usually must be relied upon to supply quantitative information. When $W = 0$, dipoles near a surface should exhibit an

alternating contrast in both bright- and dark-field (see Figs. 7 through 10). Figure 23 shows a dynamical (bright-field) and kinematical image of a dipole in a <111> slip plane section of copper. Note also the intensity discontinuity across the long single dislocation in the kinematical micrograph. Figure 24 is of a long dipole in magnesium oxide as viewed under both kinematical bright-field and dynamical dark-field conditions. The dipole runs out of the foil; the difference in length of the component dislocations is accentuated because the end of the dipole that intersects the surface runs perpendicular to the thickness gradient, as can be seen from the equal thickness fringes. The slip plane of the dipole is, within a few degrees, the plane of the foil surface. It is therefore reasonable to assume that the slip plane bisects the wedge angle of the foil edge. Because the foil increases in thickness 1 extinction distance between like thickness fringes, the dipole changes its depth from the surface by one-half extinction distance between like fringes. As can be seen from Figs. 8 and 10, a change in depth of one-half extinction distance causes the black-white image of a dipole to reverse its orientation. It is indeed observed that the black-white orientation reverses between like thickness fringes. Although the dipole calculations upon which Figs. 8 and 10 are based were carried out for a foil of 6 extinction distances thickness, and the volume enclosing the dipole shown in Fig. 24 ranges in thickness from 3 to 6 extinction distances, the depth periodicity property of images in the dynamical theory justifies the comparison. Images of identical defects that are like distances from a surface have identical black-white image orientations, irrespective of the thickness of the foil that contains them, as long as the foil is thick enough for anomalous absorption

effects to be important.[21]

III Differentiation Between a Narrow Dipole and a Single Dislocation

Figure 25 of a specimen deformed at room temperature shows several dipoles of such narrow spacing that they appear as a single dark line. It is often necessary to trace a dipole a great distance before the two component dislocations are resolvable, if ever. Frequently, the very long dipoles intersect a surface and then it is quite easy to distinguish a dipole from a single dislocation. In the case that an image appears as a single dark line over all of its visible length, the sense of the diffraction vector should be reversed (and W kept positive in bright-field) in order to determine whether the original image was a single dislocation or a dipole in inside contrast. A very narrow dipole, e.g., < 20 Burgers vectors spacing, in outside contrast will usually not have resolvable images either. However, in changing from inside to outside contrast or vice versa, there should be a change in image intensity. This will not occur for a single dislocation.

A further method for differentiating between dipoles and single dislocations is based on the difference in background intensity that occurs on either side of a single dislocation. As has been mentioned previously, this contrast discontinuity applies to screw as well as to edge dislocations, and is not associated with the bending introduced by the latter. In fact, very few single edge dislocations can be seen in the magnesium oxide slip plane sections; the single dislocations are predominately of screw character. Figures 5 and 12 in Chapter 2 illustrate the contrast discontinuities across single dislocations. Low and Turkalo[22] also have several examples of these discontinuities in their paper on Fe-3% Si. This technique is quite useful when the dipole

spacing is small enough that a dipole might be confused with a single dislocation. There is, of course, no contrast discontinuity across a narrow dipole. The presence of a contrast discontinuity is considered proof of a single dislocation, but the absence of such a discontinuity is not always proof of a dipole. The only other restriction to this technique is that it requires slip plane sections so that long single dislocations are available; the effect is masked if the single dislocations run obliquely through the foil.

The observed asymmetry of single dislocation images when $N = 2$ is not present for narrow dipoles. Thus, a dipole in inside contrast should have a relatively distinct image width, with no asymmetrical tail on one side or the other. If the dipole spacing is too narrow, the weakness of the image may make it difficult to determine whether an asymmetrical image is present. In the case of very narrow dipoles, however, it is their weak image that may be used to distinguish them from single dislocations. The many very faint images in Fig. 25 and Fig. 5 in Chapter 2 are short dipoles of spacing narrow enough that their images are relatively much weaker than the single dislocation images present. Figure 26, a dark-field micrograph taken at $W \approx 0$, shows that the very narrow dipoles, particularly in the vicinity of the micron marker, are more perceptible here than under normal bright-field conditions (compare Fig. 7 in Chapter 2 which shows the same area as viewed in bright-field). This enhanced visibility of weak strain fields, e.g., narrow dipoles, is a result of the greater intensity of dynamical images relative to kinematical images.

Besides changing the sense of the operating diffraction vector, to change from inside contrast to outside or vice versa, the kinematical

theory predicts that changing the sign of the Bragg angle deviation will accomplish the same thing. This latter technique is not feasible in bright-field; furthermore the curves of Figs. 20 and 21 show that it is also not applicable to dark-field images in crystals with strong anomalous absorption. However, if high order reflections are utilized, and regions less than about 2 or 3 extinction distances in thickness are examined, it is possible to utilize both senses of W. Figure 27 illustrates this possibility on a narrow dipole. The frame with the scale marker is a bright-field image ($W > 0$), and the rest are dark-field images with a diffraction vector opposite to that used to obtain the bright-field image. The dipole spacing is of the order of 50 Burgers vectors, but tapers to a smaller spacing towards its end. The image intensities are equivalent for both $W < 0$ and $W > 0$ indicating the absence of strong anomalous absorption. There is some activity on the $\{1\bar{1}0\}$ slip plane normal to the foil surface. At E in Fig. 27 there are a few end-on screw dislocations; the orientation of their black-white image reverses as the sign of W is changed. This is in contradiction to the predictions of Tunstall, et al.,[23] but again the discrepancy probably is related to the lack of anomalous absorption.

IV Determination of the Nature of a Dipole

Appendix II contains various schemes for the determination of the type of a dipole that intersects a surface. Techniques (A) and (B) of Appendix II both indicate that the long dipole of Fig. 24 is of the vacancy type. The white side of the black-white image of the innermost dislocation is towards the direction of g, indicating a vacancy dipole by method (A). The kinematical image is one of a dipole in outside contrast, and the similarity of the black-white image orientations in

bright and dark field indicate the dipole intersects the upper surface. Again, a vacancy dipole is the only possiblity according to scheme (B). The short dipole at A in Fig. 24 has a very strong black-white image in dark field; its bright-field image seems to indicate that it lies very close to the surface, but does not intersect it. For a dipole lying at a depth one-half extinction distance from either surface viewed in dark field, the Ashby-Brown image orientation criterion is reversed. Thus we draw the conclusion that the dipole at A in Fig. 24 is of the vacancy type. This particular result is subject to the criticism that it is based on circumstantial evidence, i.e., the exact depth of the dipole has been deduced only from the intensity of its image, as no direct way of determining it is available. The reversal of the black-white image orientation criterion, however, is a genuine effect. Note that the orientation of the first black-white image of the long dipole in Fig. 24 is the reverse of that of the innermost single segment, where the latter intersects the foil surface.

V Determination of Which Surface a Line Defect Lie Closer To

The ability to distinguish which surface is intersected by a dipole or dislocation is often useful when performing quantitative diffraction experiments. The standard method has been by comparison of bright- and dark-field images.[21] Without anomalous absorption, bright- and dark-field images would always be complementary. Under the influence of absorption, defect images in bright- and dark-field are identical at the upper surface and opposite at the lower surface. In order to differentiate between surfaces by this method, at least two micrographs and a diffraction pattern are always necessary. In addition, it is rather inconvenient to alternate between bright and dark field if the electron

gun tilt technique is used for the latter. With the results indicated by Figs. 19 through 21, it should be possible to perform all experiments in dark field. Bright-field micrographs may be taken subsequently as a check of the consistency of the experimental conclusions. As an example, scheme (C) of Appendix II may be altered so that bright-field micrographs are unnecessary.

Figure 28, a magnesium oxide specimen deformed at room temperature, illustrates the effect predicted by the calculations of Figs. 19 through 21. The bright-field micrograph (lower right) was taken with a diffraction vector opposite in sign to that used for the three dark-field micrographs (denoted by the direction of the arrow on the micron marker). The micrographs for $W < 0$ and $W > 0$ are generally complementary; defects that appear in good contrast in one, are weak in the other. Defects that intersected a surface, as indicated by the presence of an anomalous image, always are well imaged in only one of the two micrographs. Although no calculations were made, it is expected that centrally located defects would be equally visible in both $W < 0$ and $W > 0$ micrographs. However, in this case, the image intensity should be very much lower than a defect in the proximity of a surface under favorable imaging conditions. There are a few dislocations, notably in the upper right-hand corner, that appear of equally strong intensity in both micrographs. However, this region of the foil may be too thin for anomalous absorption effects to be important. Figures 6 and 8 in Chapter 2 show that if the specimen is too thin, there may be very little difference in intensity between $W < 0$ and $W > 0$ dark-field images. Only in the thicker regions of these specimens is a difference in the image intensities apparent.

Discussion

I The Column Approximation

The column approximation, which is made in the development of both the kinematical and dynamical theories, cannot be formally justified in the vicinity of the dislocation core. The usual justification put forth is simply the surprisingly good agreement between theory and experiment. In making the column approximation, it is assumed that the lateral variation of the lattice displacements is small across a unit column. Because the lattice displacements caused by a dislocation used in diffraction contrast calculations are derived from linear elasticity, they contain a $\frac{1}{r}$ divergence where r is the distance from the dislocation core. Howie[24] noted that it is only at distances close to a dislocation that the strain field varies rapidly enough to cause the scattering from one branch of the dynamical dispersion surface to the other that is necessary for diffraction contrast. It seems paradoxical that the regions where the column approximation is weakest are the ones that theoretically account for the observed contrast.

Examination of the limit of β_2 as the dislocation position was approached proved that it was identical to the limit of β_1. That is to say, the inclusion of an infinite series of images to the strain field of a screw dislocation in an infinite medium did not remove the singularity at the dislocation core. The single image added to the infinite solid edge dislocation strain field produced a similar result. On the other hand, β_2 was proportional to $\exp(-\pi D/X)$ for large X as opposed to $\frac{1}{X}$ for β_1. This dependency accounts for the narrower dislocation image that results from a proper treatment of the surfaces. The conclusion to be drawn is that addition of images in no way weakens or strengthens

the column approximation because the strain field dependence in the region where the column approximation is poorest is not changed.

The situation for the strain field of a dipole is somewhat more complicated. Outside the dipole it may be shown that the strain field goes as $\frac{1}{r^{1+c}}$ where $c \ll 1$ for r close to the dislocation core. At a distance large with respect to the dipole spacing, c approaches 1. Inside the dipole, the strain field varies as $\frac{1}{r}$ close to either of the dislocations, and less rapidly between them. It is only important to note that the column approximation is no less valid near the dislocation positions of a dipole than near the core of a single dislocation. In the tails of the dipole strain field, where the dependence is as $\frac{1}{r^2}$ the value of the strain field is already so small that the only thing that possibly could be affected would be the width of the contrast profile. This portion of the image is the least informative and any slight inaccuracy there would be of trivial consequence. In this regard, Ashby and Brown,[14] in computing images of inclusions, used displacement fields that varied as $\frac{1}{r^3}$ outside the inclusion and still were able to correlate their calculated image widths with experimental results. Again the inference is that the dynamical calculations appear to be reliable even though the column approximation may be in question.

II Transition from Kinematical to Dynamical Diffraction Conditions

The most important result of this part of the investigation was the determination that the limit of applicability of the kinematical theorem of one-sided contrast occurs for a value of W as low as 0.75. Quantitatively, the kinematical theory (see Appendix III) predicts the position of maximum scattered intensity for N = 2 will be at either $\frac{X}{\xi_g} = \pm \frac{1}{2\pi W}$, the sign depending on the sign of the dislocation. The

intensity maximum is proportional to $\frac{1}{W^2}$. The movement of an edge dislocation image towards the actual position of the dislocation with increasing W only can be seen in Fig. 2 (g) where W = 3, indicating that the above formulae become valid for $2 < W < 3$.

Although, in the kinematical theory the position of the image depends only on the deviation from the Bragg angle, being inversely proportional to it, the image position as calculated by the dynamical theory depends on both W and the depth of the dislocation in the foil. We can thus construct this picture of how the image position changes with W. For large W, the image is very close to the actual dislocation core, as predicted by the kinematical theory. As W decreases, the image moves further away, but reaches some maximum value, probably near the limits of validity of the kinematical theory. As W tends to zero, the image position may move to the other side of the dislocation, crossing the core at some value of W between 0 and 1 (see Fig. 2), it may move closer to the core, remaining on the same side, or it may not move at all. The W = 0 image position depends solely on the depth of the dislocation in the foil. Furthermore, the W = 0 image positions for bright- and dark-field images will only be the same near the upper surface,[21] whereas in the kinematical treatment, the bright- and dark-field image positions always coincide for all values of W. In both theories, the maximum distance the image of a dislocation can be from the position of the dislocation is proportional to N.

III Kinematical Theory of Dipole Contrast

The present theoretical and experimental results have shown that the kinematical theory as applied by Wilkens correctly predicts the qualitative behavior of dislocation dipole contrast, and in particular the occurrence

of outside and inside contrast, if the Bragg angle deviation parameter is greater than about 1. With respect to this transition to one-sided contrast, the kinematical theory is equally applicable to single dislocations and dipoles. In the same way, the limitations of applicability of the kinematical theory are quite the same for single dislocations and dipoles. For example, the predicted diffracted intensities and image positions are incorrect in both cases for $W < 3$. As an extreme case, consider a narrow dipole of fixed spacing, $2X_o$, and decrease only the Bragg angle deviation parameter, W, so that the product $2X_oW$ decreases to 0.1. According to the kinematical theory, the scattered intensity would be very low, but in fact, the opposite will be true for $W \approx 1$. This example indicates the inability of the kinematical theory to deal with a strongly diffracting crystal. A second source of error might be the inaccuracies in image position as predicted by the kinematical theory. The amount of mutual enhancement or cancellation of the component images of a dipole depends on the distance the images lie from the actual dislocation positions and from each other. When W is small, the kinematical images lie quite far from the dislocations. In the dynamical region, the images need not lie so far removed from their respective dislocations, so that cancellation may not be as complete. Figures 17 and 18 show cases where the depth of the dipole is such that the dynamical and kinematical image sides do not coincide. Thus, for the interstitial dipoles with the largest spacing, the W = 1.0 image is in inside contrast and the W = 0 image is in a sort of dynamical outside contrast. The reverse situation occurs for the vacancy dipole.

IV Dynamical Theory of Dipole Contrast

The inherent limitation in applying the dynamical theory to experimental observations of lattice defects is that, because of the strong

depth dependence of a dynamical image, a knowledge of the depth of the defect being studied is necessary. One way to circumvent this problem is to study defects that intersect the foil surface. This technique provides a point of reference to study dynamical contrast effects, and has the added advantage that images are usually strongest there. The only fact that then needs to be determined is which surface, upper or lower, the defect intersected. Absorption effects allow the surfaces to be differentiated by a number of methods, so that this remaining question provides little difficulty. As an application of these general considerations, the nature (interstitial or vacancy) of dipoles that intersect a foil surface can easily be determined.

One objection to the application of the dynamical equations near surfaces has been made by Bell.[25] Dynamical equation 1) (see section on Details of Calculations) has a term involving the contribution of the diffracted beam to the transmitted beam. A simple geometrical argument shows that a beam diffracted at the upper surface must travel down into the foil a distance $y = \frac{2a_o^2}{\lambda (h^2 + k^2 + \ell^2)}$ before it can be rediffracted from an adjacent diffracting plane and hence be converted to a beam travelling parallel to the original transmitted beam. In the above equation a_o is the lattice constant, λ is the wavelength of the electrons and $(h\ k\ \ell)$, the diffracting plane. A similar argument can be made for the lower surface. This situation arises because Howie and Whelan replaced the original difference equation by differential equations under the approximation of a continuum of scatterers. Bell thus reached the conclusion that the dynamical theory of contrast only applies for defects located at depths between y and D - y, where D is the foil thickness. In the present work $\underline{g} = \langle 220 \rangle$ and hence y is about 120 Å or $\frac{\xi_{220}}{6}$; therefore,

this effect is not very important. Also, using slip plane sections, the dipole contrast can be followed up to the point where the contrast weakens, and the image orientation criterion applied there; it is immaterial whether the image disappears exactly at the surface or at a depth y. On the other hand, if localized defects, such as small dislocation loops, are being studied, the uncertainty of their depth with relation to y is an important consideration in attempting to apply the dynamical theory.

A further result of the theoretical calculations is to provide a semi-quantitative limit on the visibility of very narrow dipoles. The strain functions used in the calculation were derived from linear elasticity theory, so that the values obtained are probably a lower limit. Due to lattice relaxation, the strain fields around dipoles in real crystals are expected to be somewhat weaker than in an isotropic elastic medium; this difference would mean that, at a given spacing, the dipole image would be somewhat weaker than is predicted. Finally, dark-field dynamical images are to be preferred over kinematical bright-field images when studying the distribution of narrow dipoles because of their relatively greater intensity when the dipole spacing is less than 40 Burgers vectors.

APPENDIX I

Strain Field Formulae

$$\beta_1 (x,z,\eta) = \frac{b}{2\pi} \frac{x}{x^2+(z-\eta)^2} \tag{I-1}$$

$$\beta_2 (x,z,\eta,D) = \frac{b}{8D} \left[\frac{\sinh \frac{\pi}{D} x \quad \sin \frac{\pi}{D} z \sin \frac{\pi}{D}}{\{(\sinh^2 \frac{\pi}{2D} x+\sin^2 \frac{\pi}{2D}(z-\eta)\}(\sinh^2 \frac{\pi}{2D}x+\sin^2 \frac{\pi}{2D}(z+\eta))} \right] \tag{I-2}$$

$$\beta_4 (x,z,\eta) = \beta_1 + \frac{bx}{4\pi(1-\nu)} \left[\frac{x^2 - (z-\eta)^2}{[x^2 + (z-\eta)^2]^2} \right] \tag{I-3}$$

$$\S \quad \beta_7 (x,z,\eta) = \frac{b}{2\pi} \frac{4 x z\eta}{[x^2+(z-\eta)^2][x^2+(z+\eta)^2]} + \frac{bx}{4\pi(1-\nu)} \left[\frac{(x^2-(z-\eta)^2)}{[x^2+(z-\eta)^2]^2} - \frac{(x^2+(z+\eta)^2)}{[x^2+(z+\eta)^2]^2} \right] \tag{I-4}$$

$$\S \ \beta_{10} (x,z,\eta,D) = \frac{b}{2\pi} \frac{4 x (D-z) (D-\eta)}{[x^2+(z-\eta)^2][x^2+(2D-\eta-z)^2]} + \frac{bx}{4\pi(1-\nu)} \left[\frac{x^2-(z-\eta)^2}{[x^2+(z-\eta)^2]^2} - \frac{x^2-(2D-\eta-z)^2}{[x^2+(2D-\eta-z)^2]^2} \right] \tag{I-5}$$

§ The exact treatment of an edge dislocation in a semi-infinite medium has yet another term in each of the displacements, R_x and R_z. The sum of the normal derivatives of these displacements times the appropriate constants cancel the residual normal stress on the surface z = 0. The cross derivatives $\frac{\partial R_x}{\partial z}$ and $\frac{\partial R_z}{\partial x}$ are equal and opposite and hence do not contribute to the shear stress. See Pfeiffer[26] for a more complete discussion.

In any case, the additional term in the expression for β_7 (or β_{10}) is small even for single dislocations and completely neglectable for dipoles. A more valuable inclusion for single edge dislocations would be the exact treatment of both surfaces.

APPENDIX II

Methods for the Determination of the Nature of a Dipole that Intersects a Foil Surface

The dipole should intersect the surface at as shallow an angle as possible, e.g., in a slip plane section, in order to maximize the difference in lengths of the two component dislocations.

1. Experimental Requirements

   a. Dark-field micrograph (gun tilt, $W = 0$) and sign of $\underset{\sim}{g}$ from diffraction pattern.

   b. Dark-field micrographs for $W < 0$ and $W > 0$. Anomalous absorption must be present.

   c. Bright-field micrograph ($W > 0$) and sign of $\underset{\sim}{g}$ from diffraction pattern.

   d. Knowledge of whether dipole is in outside or inside contrast in (c). Determined by changing the sign of $\underset{\sim}{g}$ or W, or by examination of dislocation image asymmetry ($N = 2$) for $W \gtrsim 1$. The diffuse side of the image is always on the side away from the actual position of the dislocation.

   e. Supplementary bright-field micrographs and diffraction pattern taken with same $\underset{\sim}{g}$ as in (c) after specimen has been tilted in a known direction through a large angle, e.g., 35°. This can be effected in a large tilt-angle goniometric stage, taking care to tilt about the perpendicular to the diffracting planes of (c). In this way, constancy of diffraction conditions is obtained.

2. Techniques

   A. Use 1(a) and Ashby-Brown criterion: if white side of black-

white image is towards the direction of g, then the dipole is of the vacancy type; if vice versa, then dipole is of the interstitial type. Use anomalous image of longer of the two dipole segments, i.e., the dislocation closer to foil center.

B. Use 1(c) and 1 (d) to eliminate two of four possible dipole configurations by application of the kinematical theorem. Then, by comparing 1(a) and 1(c), determine which surface is intersected by the dipole. This comparison will eliminate one of the two remaining dipole configurations, since they have opposite senses. One of the senses will be consistent with the dipole intersecting the upper surface, and the other, with it intersecting the lower surface.

C. Same as (B), but use 1(b) to determine which surface of the dipole intersects.

D. Use 1(c) and 1(d) as in (B). Then determine the sense of the dipole from the geometrical shape change of the dipole observable in (e). The direction of rotation must be known to do this. As mentioned in (B) only one dipole configuration will be consistent with change produced by the rotation. Technique D has the advantage of not requiring the dipoles sampled to intersect the surface. In fact, if there is a high density of dipoles in a given area, a large number of determinations may be carried out in one operation. In magnesium oxide observed in {110} slip plane sections, the only convenient $\underset{\sim}{g}$ is <220>. Since $\underset{\sim}{g}$ and $\underset{\sim}{b}$ are exactly parallel in this orientation, pure edge dipoles rotated about their Burgers vector will show only a decrease in length and no change in projected width. Thus, this technique requires, at least for the magnesium

oxide geometry used, dipoles with significant screw character; fortunately, these are available.

APPENDIX III

Derivation of Kinematical Scattered Intensity for a Screw Dislocation (Infinite Body Strain Field) When N = 2.

This is the case treated by Wilkens.[3]

Consider the kinematical diffracted intensity[1]

$$A = \frac{i\pi}{\xi_g} A_o \int_{-Z_1}^{Z_2} e^{-2\pi i \underset{\sim}{g} \cdot \underset{\sim}{R}} e^{-2\pi i S_g Z} \, dZ. \qquad \text{(III-1)}$$

The screw dislocation is at the origin of coordinates in a foil of thickness $D = Z_1 + Z_2$, at a depth Z_1.

Now,

$$R = \frac{b}{2\pi} \tan^{-1} \frac{Z}{x} \qquad \text{(III-2)}$$

so that

$$2\pi i g R = igb \tan^{-1} \frac{Z}{x} = N \tanh^{-1} \left[\frac{iZ}{x} \right] ; \qquad \text{(III-3)}$$

but,

$$\tanh^{-1} \frac{b}{a} = \frac{1}{2} \ell n \frac{a + b}{a - b} . \qquad \text{(III-4)}$$

Thus,

$$2\pi i g R = \frac{N}{2} \ell n \left[\frac{x + iZ}{x - iZ} \right] , \qquad \text{(III-5)}$$

and since $e^{\ell n x} = x$ we have finally that

$$A = \frac{i\pi}{\xi_g} A_o \int_{-Z_1}^{Z_2} e^{-2\pi i S_g Z} \left[\frac{x - iZ}{x + iZ} \right]^{\frac{N}{2}} dZ. \qquad \text{(III-6)}$$

We now change the limits of integration to move the origin to the upper surface of the foil. The approximation of replacing the upper limit D by ∞ is also made, as was done in the original kinematical theory.[1] This corresponds to replacing the original crystal with a semi-infinite one, and has the effect of eliminating any constant background intensity.

The resulting integral can be found in closed form by a routine contour integration if N is even. We choose N = 2, and find

$$A = \frac{i\pi A_o}{\xi_g} \int_o^\infty e^{-2\pi i S_g (Z-Z_1)} \left(\frac{x - i(Z-Z_1)}{x + i(Z-Z_1)} \right) d\,(Z-Z_1) \qquad \text{(III-7)}$$

The integrand has a simple pole at $Z = Z_1 + ix$ in the upper half plane. We can distinguish two cases, according to the sign of S_g. If S_g is positive, we must close the contour in the lower half plane in order that the contribution of the integral along the semi-circular contour be zero in the limit of $|Z| \to \infty$. However, there is no pole in the lower half plane amd therefore A = 0. If S_g is negative, we must close the contour in the upper half plane, and here A is non-zero. After computing the residue we have

$$A = \frac{i\pi A_o}{\xi_g} \left(\pi i \left[2x\, e^{2\pi S_g x} \right] \right) = -2\pi^2 A_o \frac{x}{\xi_g} e^{2\pi S_g x}, \quad S < 0. \qquad \text{(III-8)}$$

The scattered intensity is $|A|^2$ and is equal to

$$I = 4A_o^2 \pi^4 \left(\frac{x}{\xi_g} \right)^2 e^{4\pi S_g x}, \qquad S_g < 0 . \qquad \text{(III-9)}$$

and occurs <u>only</u> on one side of the dislocation, for a given value of S_g. The scattered intensity is zero at both x = 0 and $x = \infty$, and also has a zero slope at these points. The intensity maximum, which is usually taken as the position of the dislocation image, occurs at

$$X_m = - \frac{1}{2\pi S_g} \; ; \qquad \text{(III-10)}$$

in terms of the dynamical deviation parameter, this is

$$\left(\frac{X_m}{\xi_g} \right) = - \frac{1}{2\pi W} . \qquad \text{(III-11)}$$

The amplitude of the maximum is

$$I_{max} = \frac{A_o^2 \pi^2 e^{-2}}{W^2} \qquad \text{(III-12)}$$

If the sign of the dislocation is reversed, the exponential in (III-9) becomes negative and (III-10) and (III-11) each change sign. The final result is that if either the sign of W or of $\underset{\sim}{g} \cdot \underset{\sim}{b}$ change, the position of the image changes from one side of the dislocation to the other.

REFERENCES

1. P. B. Hirsch, A. Howie and M. J. Whelan, Phil. Trans. Roy. Soc. A 252, 499 (1960).
2. A. Howie and M. J. Whelan, Proc. Roy. Soc. A 263, 217 (1961); Ibid. A 267, 206 (1962).
3. M. Wilkens and E. Hornbogen, Phys. Stat. Sol. 4, 557 (1964).
4. R. Siems, P. Delavignette and S. Amelinckx, Phys. Stat. Sol. 2, 421 (1962).
5. G. W. Groves and M. J. Whelan, Phil. Mag. 7, 1603 (1962).
6. G. W. Groves and A. Kelly, Phil. Mag. 6, 1527 (1961); Ibid. 7, 892 (1962) erratum.
7. E. Ruedl, P. Delavignette and S. Amelinckx, Proc. I.A.E.A. Symp. on Radiation Damage in Solids and Reactor Materials, Venice, Italy, 1962, 1, 363 (I.A.E.A., Vienna), (1962).
8. D. J. Mazey, R. S. Barnes and A. Howie, Phil. Mag. 7, 1861 (1962).
9. R. Bullough and R. C. Newman, United Kingdom AEA Harwell Research Group Report, AERE R 4551 (1964).
10. J. Friedel, Dislocations, Pergamon Press, Oxford (1964).
11. G. Leibfried and H-D. Dietze, Z. Phys. 126, 790 (1949).
12. H.-D. Dietze, Diplomarbeit, Göttingen, (1949).
13. F. Kroupa, Czech. J. Phys. 9, 488 (1959).
14. M. P. Ashby and L. M. Brown, Phil. Mag. 8, 1083 and 1649 (1963).
15. R. D. Heidenreich, Fundamentals of Transmission Electron Microscopy, J. Wiley and Sons, New York (1964).
16. FORTRAN Language Subroutine, Space Technology Laboratories Programming Handbook for the IBM 704 (1958).
17. D. H. Chung, Phil. Mag. 8, 833 (1963).

18. G. Thomas, Transmission Electron Microscopy of Metals, J. Wiley and Sons, New York (1962).

19. J. Watanabe, A. Fukuhara and K. Kohra, Proc. Int. Conf. on Magnetism and Crystallography, Kyoto, Japan, 1961, J. Phys. Soc. Japan 17, B-II, 195 (1962).

20. C. J. Ball, Phil. Mag. 9, 541 (1964).

21. H. Hashimoto, A. Howie and M. J. Whelan, Proc. Roy. Soc. A 269, 80 (1962).

22. J. R. Low and A. M. Turkalo, Acta Met. 10, 215 (1962).

23. W. J. Tunstall, P. B. Hirsch and J. Steeds, Phil. Mag. 9, 99 (1964).

24. A. Howie, Proc. Roy. Soc. A 271, 268 (1963).

25. W. Bell, M. S. Thesis, University of California, Berkeley, California, UCRL-16024 (1965).

26. W. Pfeiffer, Z. Naturforschg. 19 a, 294 (1964).

FIGURE CAPTIONS

Fig. 1 Bright-field images of single edge and screw dislocations: a) N = 1, β_1 and β_2 W = 0, $\eta = \frac{1}{2}$; b) same as a) but β_7; c) same as b) but W = 1.0; d) N = 1, β_2, W = 0, $\eta = 2\frac{3}{4}$; e) same as d) but β_7; f) same as d) but $\eta = 3$; g) same as f) but β_7.

Note: In these and all the plots that follow: W is the Bragg angle deviation parameter; N is $\underset{\sim}{g} \cdot \underset{\sim}{b}$; β is the relevant strain function; η is the depth of the defect in extinction distances (the foil thickness is 6 extinction distances). Plot a) is always the upper left plot, with b) below it, etc.

Fig. 2 Bright-field images of an edge dislocation (extra half-plane down) illustrating effect of deviation from the Bragg angle. N = 2, β_7, $\eta = \frac{1}{2}$: a) W = 0; b) W = 0.25; c) W = 0.5; d) W = 0.75; e) W = 1.0; f) W = 2.0; g) W = 3.0

Fig. 3 Dark-field images corresponding to Fig. 2. N = 2, β_7, $\eta = \frac{1}{2}$: a) W = 0; b) W = 0.25; c) W = 0.50; d) W = 0.75; e) W = 1.0; f) W = -1.0

Fig. 4 Dynamical bright-field images of an edge dislocation (extra half-plane down) illustrating effect of depth in foil on the images. N = 2, β_7, W = 0: a) $\eta = \frac{1}{4}$; b) $\eta = \frac{1}{2}$; c) $\eta = 1$; d) $\eta = \frac{3}{2}$; e) $\eta = 2$; f) $\eta = 2\frac{3}{4}$; g) $\eta = 3$; h) $\eta = 5$.

Fig. 5 Kinematical bright-field images corresponding to Fig. 4, N = 2, β_7, W = 1.0 (in all but c)): a) $\eta = \frac{1}{4}$; b) $\eta = \frac{1}{2}$; c) $\eta = 1$, W = 0.5; d) $\eta = 1$; e) $\eta = \frac{3}{2}$; f) $\eta = 2$; g) $\eta = 2\frac{3}{4}$; h) $\eta = 3$

Fig. 6 Dynamical bright-and dark-field images for single edge dislocations and edge dipoles symmetrically positioned with respect to the foil

center, W = 0, left column - bright-field, right column - dark-field: a) β_7 (extra half-plane down), $\eta = 1$; b) β_{11}, $\eta = 5$; c) β_{12} (vacancy dipole), $\eta = 1$; d) β_{13}, $\eta = 5$

Fig. 7 Dynamical bright-field vacancy edge dislocation diople images as a function of depth: N = 2, W = 0, β_8, dipole spacing $2X_o = 20\underset{\sim}{b}$: a) $\eta = \frac{1}{4}$; b) $\eta = \frac{1}{2}$; c) $\eta = 1$; d) $\eta = \frac{3}{2}$; e) $\eta = 2$; f) $\eta = 2\frac{3}{4}$; g) $\eta = 3$; h) $\eta = 5$

Fig. 8 Dynamical dark-field vacancy edge dislocation dipole. Images as a function of depth. Dark-field images corresponding to Fig. 7, with all conditions the same.

Fig. 9 Dynamical bright-field interstitial edge dislocation dipole. Images as a function of depth. N = 2, W = 0, β_8, dipole spacing $2X_o = 20\underset{\sim}{b}$; a) $\eta = \frac{1}{4}$; b) $\eta = \frac{1}{2}$; c) $\eta = 1$; d) $\eta = \frac{3}{2}$; e) $\eta = 2$; f) $\eta = 2\frac{3}{4}$; g) $\eta = 3$

Fig.10 Dynamical dark-field interstitial edge dislocation. Dipole images as a function of depth. Dark-field images corresponding to Fig. 9 with all conditions the same.

Fig.11 Kinematical bright-field vacancy edge dislocation dipole images as a function of depth. N = 2, W = 1.0, β_8, dipole spacing $2X_o = 20\underset{\sim}{b}$. Kinematical images corresponding to Fig. 7. Outside contrast: a) $\eta = \frac{1}{4}$; b) $\eta = \frac{1}{2}$; c) $\eta = 1$; d) $\eta = \frac{3}{2}$; e) $\eta = 2$; f) $\eta = 2\frac{3}{4}$; g) $\eta = 3$

Fig.12 Kinematical bright-field interstitial edge dislocation dipole; images as a function of depth. N = 2, W = 1.0, β_8, dipole spacing $2X_o = 20\underset{\sim}{b}$. Kinematical images corresponding to Fig. 9. Inside contrast; dipole depth values are the same as in Fig. 11.

Fig.13 Dynamical bright- and dark-field vacancy edge dislocation dipole images as a function of spacing, $N = 1$, $W = 0$, β_8, $\eta = 3$. Left column - bright-field; right column - dark-field: a) $2X_o = 10\underset{\sim}{b}$; b) $2X_o = 20\underset{\sim}{b}$; c) $2X_o = 50\underset{\sim}{b}$

Fig.14 Dynamical bright- and dark-field vacancy edge dislocation dipole images as a function of spacing $N = 2$, $W = 0$, β_8, $\eta = 3$. Left column - bright-field; right column - dark;field: a) $2X_o = 10\underset{\sim}{b}$; b) $2X_o = 20\underset{\sim}{b}$; c) $2X_o = 50\underset{\sim}{b}$; d) $2X_o = 100\underset{\sim}{b}$

Fig.15 Dynamical bright-field interstitial edge dislocation dipole images as a function of spacing. $N = 2$, $W = 0$, β_8, $\eta = 3$: a) $2X_o = 6\underset{\sim}{b}$; b) $2X_o = 10\underset{\sim}{b}$; c) $2X_o = 20\underset{\sim}{b}$; d) $2X_o = 40\underset{\sim}{b}$; e) $2X_o = 50\underset{\sim}{b}$; f) $2X_o = 60\underset{\sim}{b}$; g) $2X_o = 100\underset{\sim}{b}$

Fig.16 Dynamical dark-field interstitial edge dislocation dipole images as a function of spacing. These images correspond to those of Fig.15.

Fig.17 Dynamical and Kinematical bright-field vacancy edge dislocation dipole images as a function of spacing; $N = 2$, β_8, $\eta = \frac{1}{2}$. Left column - $W = 0$; right column - $W = 1.0$: a) $2X_o = 10\underset{\sim}{b}$; b) $2X_o = 20\underset{\sim}{b}$; c) $2X_o = 50\underset{\sim}{b}$

Fig.18 Dynamical and Kinematical bright-field interstitial edge dislocation dipole images as a function of spacing. All parameters the same as in Fig. 17.

Fig.19 Bright- and dark-field interstitial edge dislocation dipole images as a function of the Bragg angle deviation parameter W; $N = 2$, β_8, $\eta = 1$, $2X_o = 10\underset{\sim}{b}$. Left column - bright-field; right column - dark-field: a) $W = 0.5$; b) $W = 0.25$; c) $W = 0$; d) $W = -0.25$; e) $W = -0.50$

Fig.20 Dark-field interstitial edge dislocation dipole images as a function of the Bragg angle deviation parameter W; Left column - $\eta = \frac{1}{2}$;

right column - $\eta = 1$. $N = 2$, β_8, $2X_o = 20\underset{\sim}{b}$: a) $W = -1.0$; b) $W = 0$; c) $W = 1.0$

Fig.21 Dark-field vacancy edge dislocation dipole images as a function of deviation from the Bragg angle. All parameters the same as in Fig. 20.

Fig.22 Kinematical bright-field images of a wide dipole in a {110} slip plane section from a magnesium oxide crystal deformed at 1000°C: a) inside contrast; b) outside contrast.

Note: In the following micrographs, the black markers are one micron in length unless otherwise noted and are parallel to the active Burgers vector in the plane of the foil. The direction of the arrowhead, when shown, indicates the direction of the diffraction vector $\underset{\sim}{g}$. Micrograph a) is always the upper one.

Fig.23 Dynamical and kinematical bright-field images of a dipole in a {111} copper slip plane section: a) kinematical; b) dynamical. (Courtesy G. Murty).

Fig.24 Kinematical bright-field and dynamical dark-field image of dipoles in a {110} slip plane section from a magnesium oxide crystal deformed at 750°C: a) kinematical - The long dipole intersects the surface in the upper right corner of the figure. The outer and inner component dislocations of the dipole intersect the surface near the left and right sides of the oval stain, at O and I, as can be determined from the anomalous width of the black images there. b) dynamical - The component images are at the limit of resolution, indicating a dipole spacing of 30 - 40 $\underset{\sim}{b}$. The sense of the diffraction vector is the same in a) and b).

Fig.25 Kinematical bright-field images in a {110} slip plane section from a magnesium oxide crystal deformed at room temperature. There are several examples of the pronounced contrast effect that occurs when a dipole intersects the surface (at I). Several narrow dipoles, $< 20\underset{\sim}{b}$ spacing, are faintly visible in the central portion of the figure.

Fig.26 Dynamical dark-field images in a {110} slip plane section from a magnesium oxide crystal deformed at 500°C. The many faint images near the micron marker are very narrow dipoles imaged only by their residual strain.

Fig.27 Comparative kinematical and dynamical images of an edge dipole attached to a screw dislocation in a {110} slip plane section a magnesium oxide crystal deformed at 750°C along a [001] axis: a) bright field, $+\underset{\sim}{g}$; b) dark field, $-\underset{\sim}{g}$, $W < 0$; c) dark field, $-\underset{\sim}{g}$, $W = 0$; d) dark field, $-\underset{\sim}{g}$, $W > 0$. End-on screw dislocations are visible at E.

Fig.28 Comparative kinematical and dynamical images in a slip plane section of a magnesium oxide crystal deformed at room temperature: a) dark field, $+\underset{\sim}{g}$, $W > 0$; b) dark field, $+\underset{\sim}{g}$, $W = 0$; c) dark field, $+\underset{\sim}{g}$, $W < 0$; d) bright field, $-\underset{\sim}{g}$, $W > 0$.

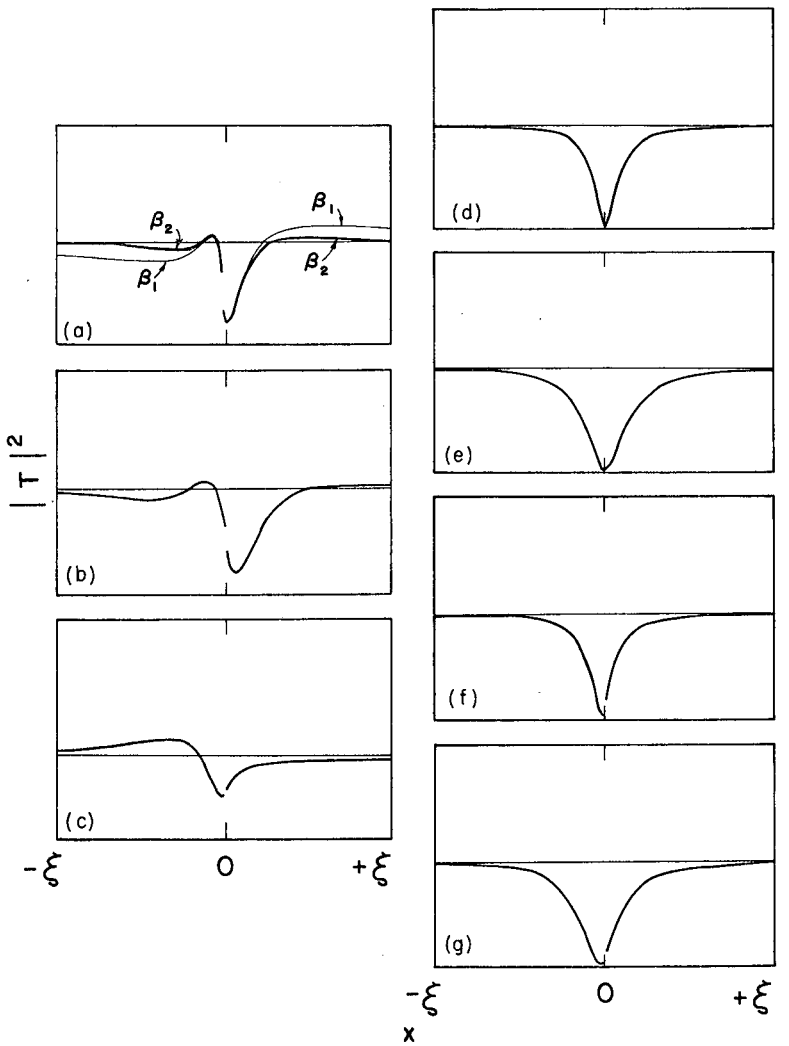

Fig. 1

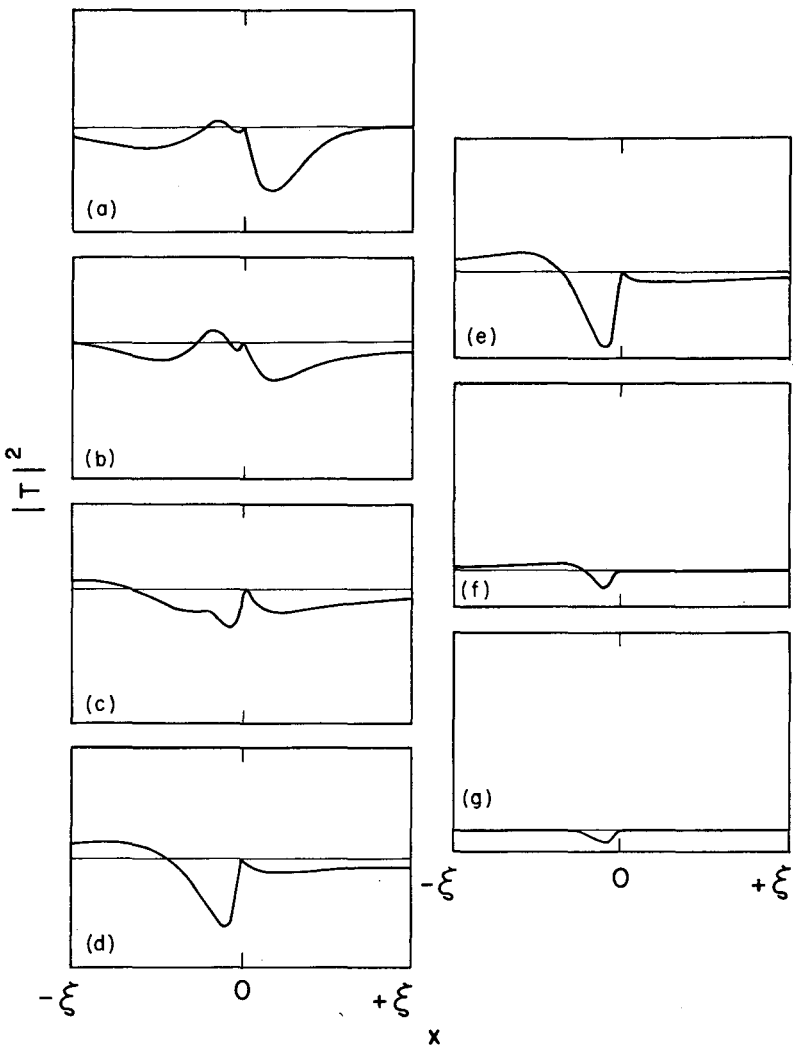

Fig. 2

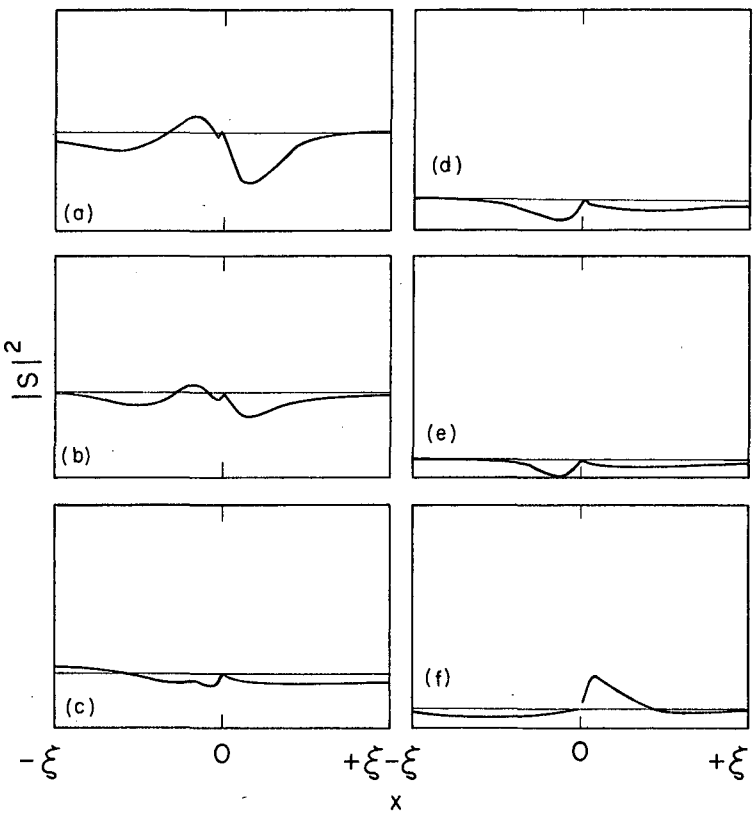

Fig. 3

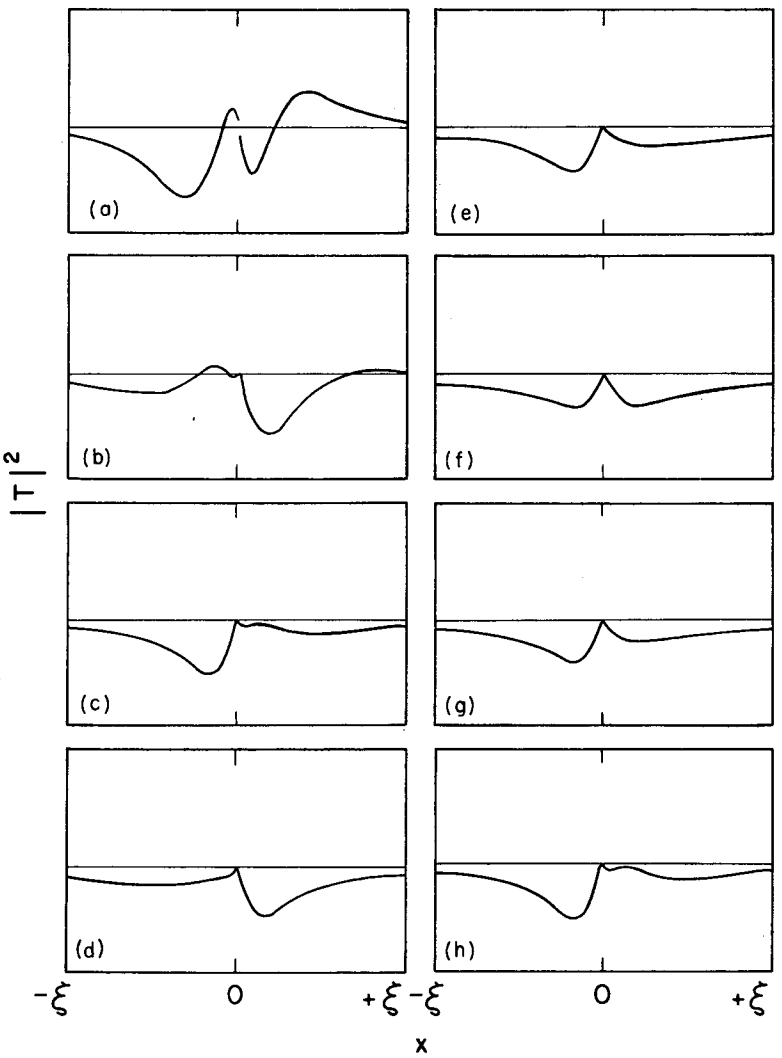

Fig. 4

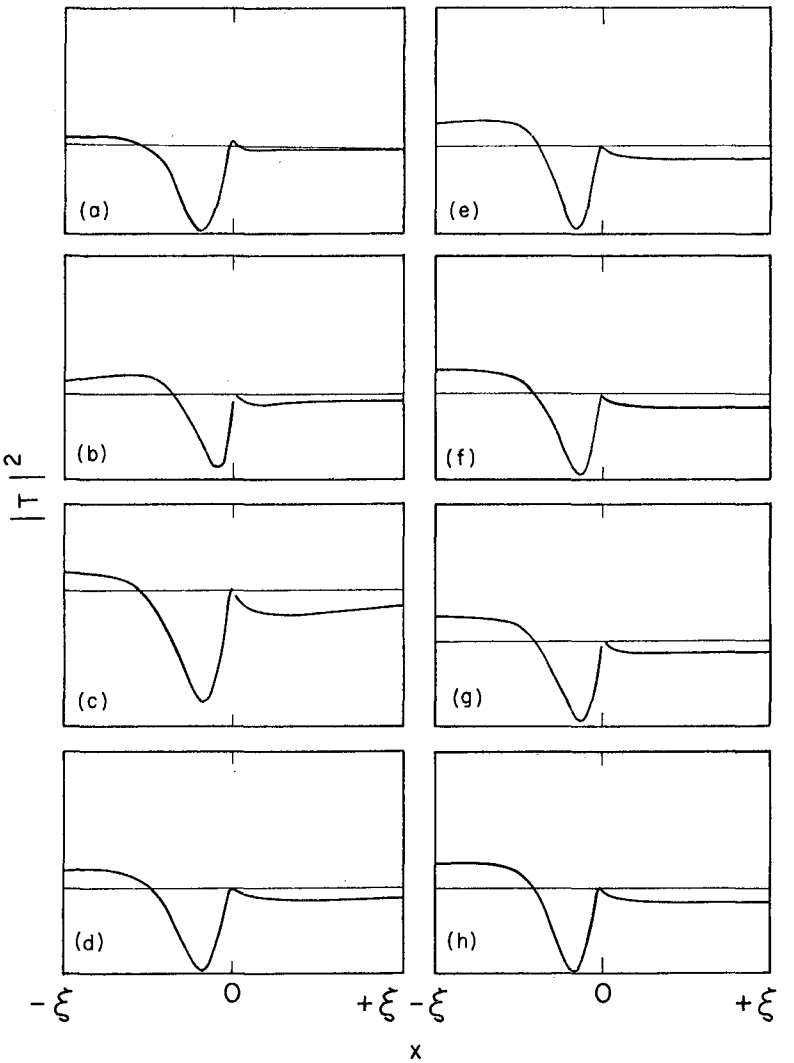

Fig. 5

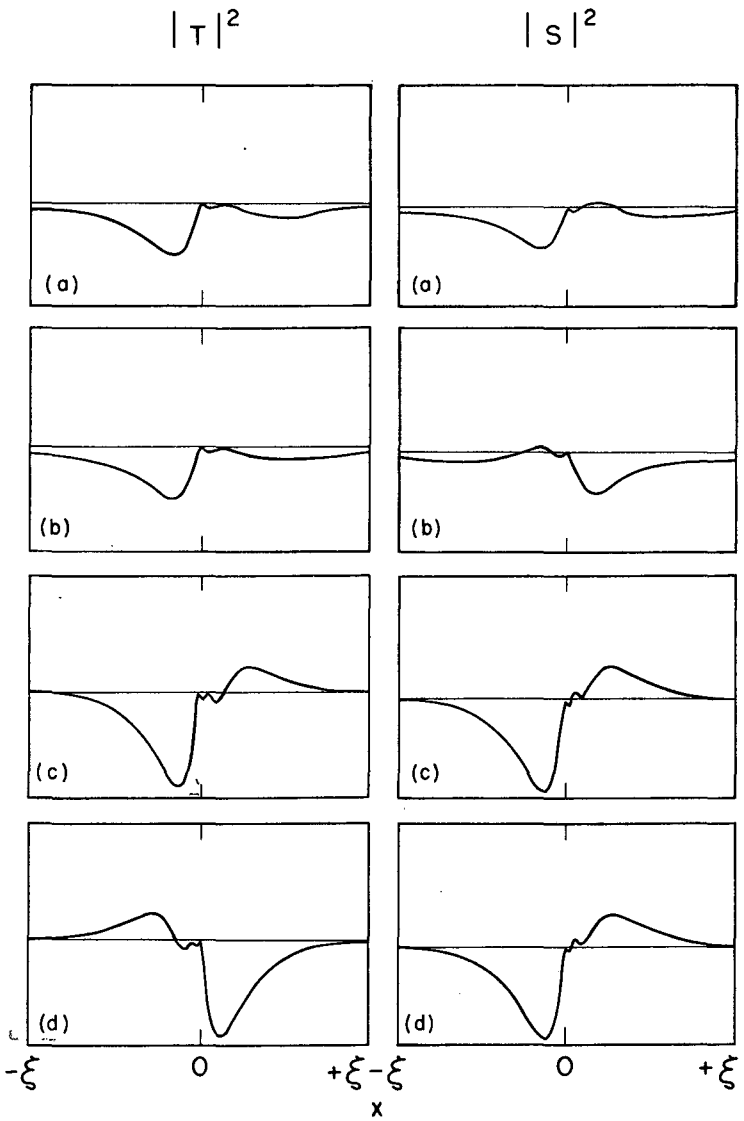

Fig. 6

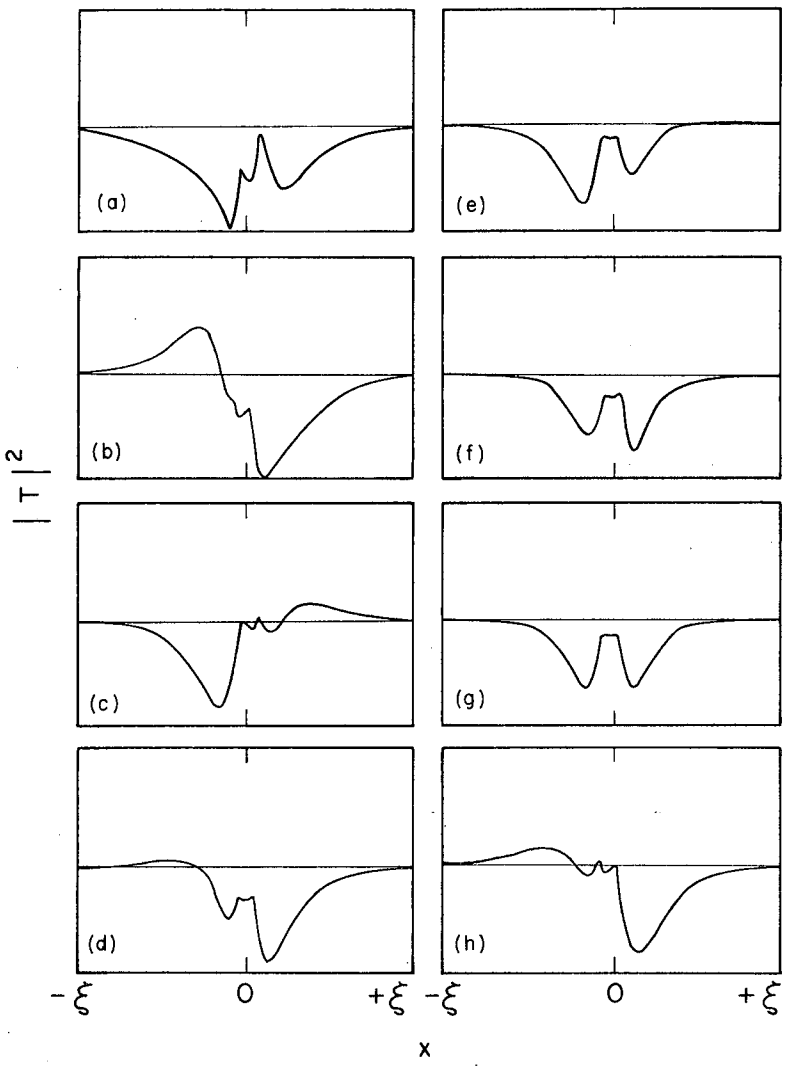

Fig. 7

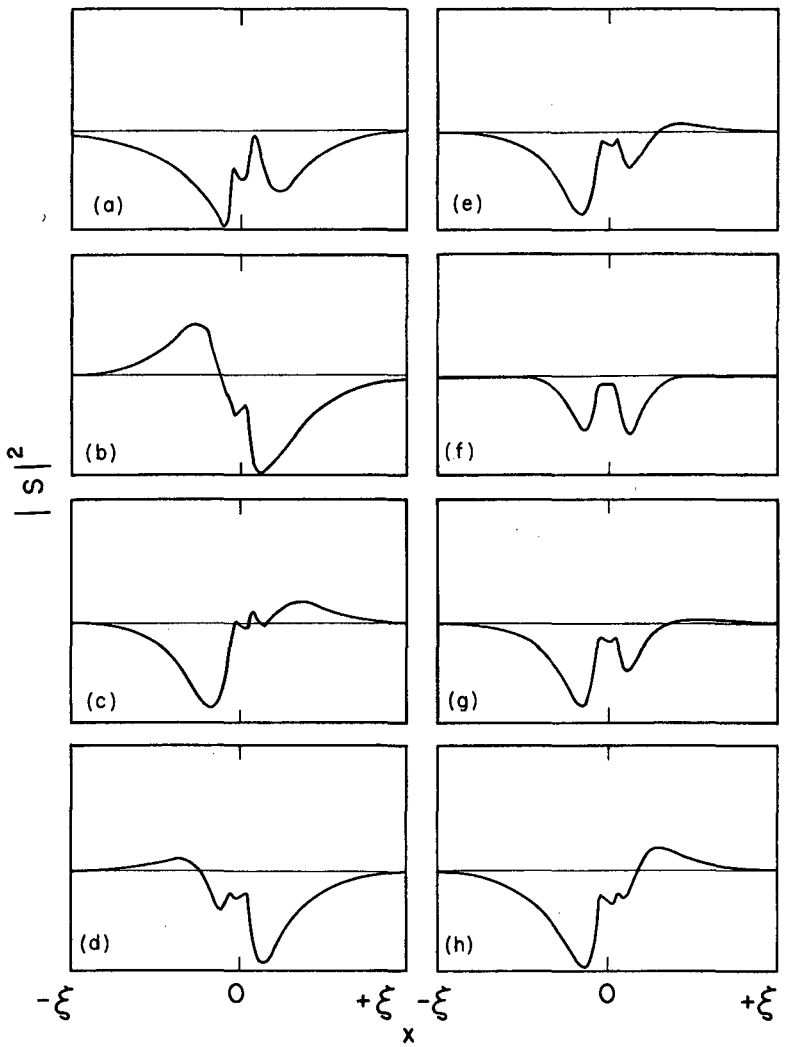

Fig. 8

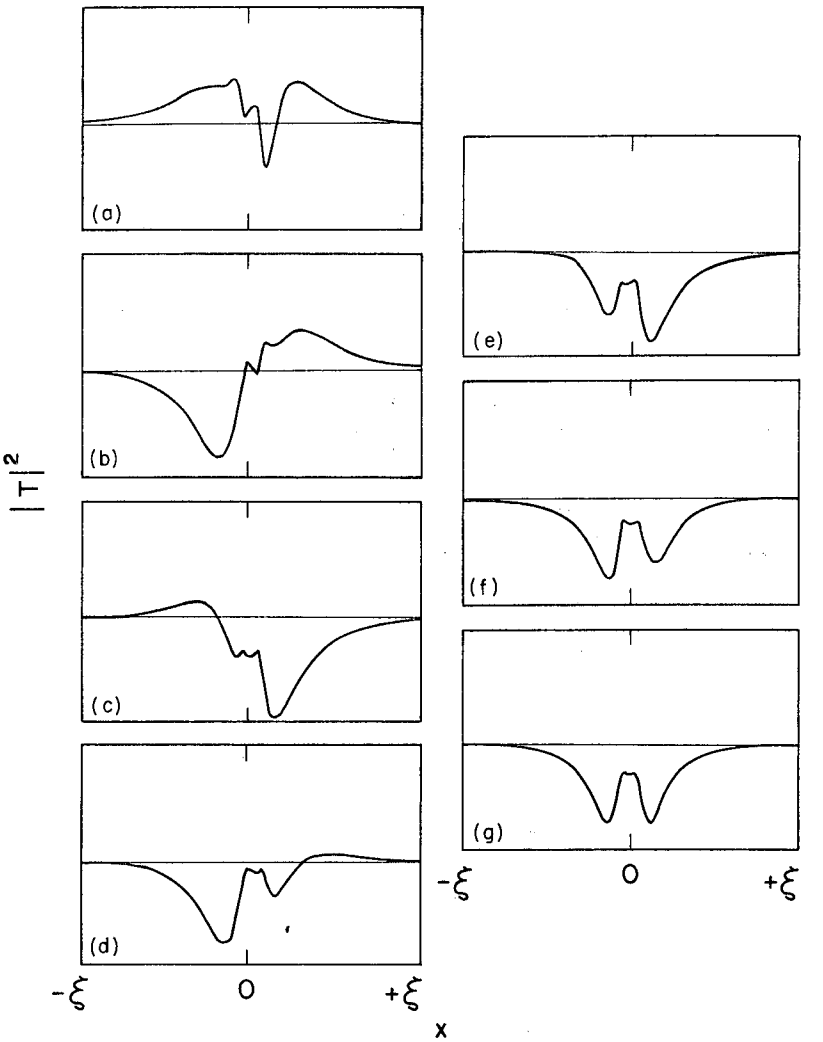

Fig. 9

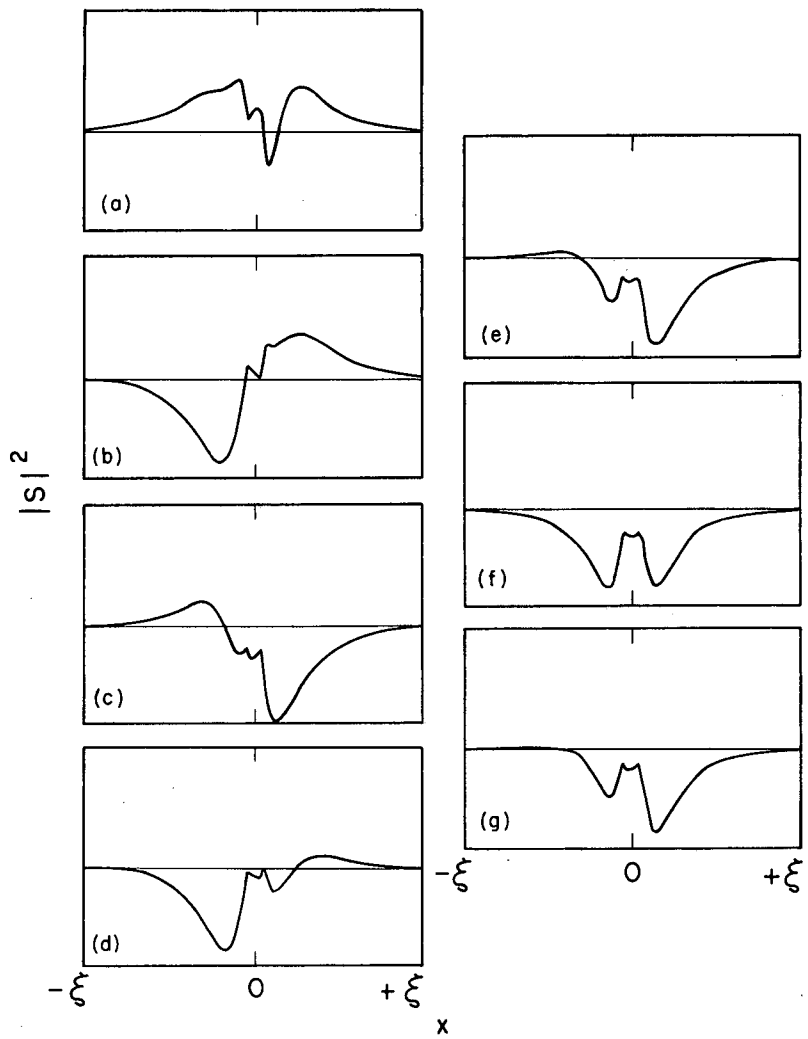

Fig. 10

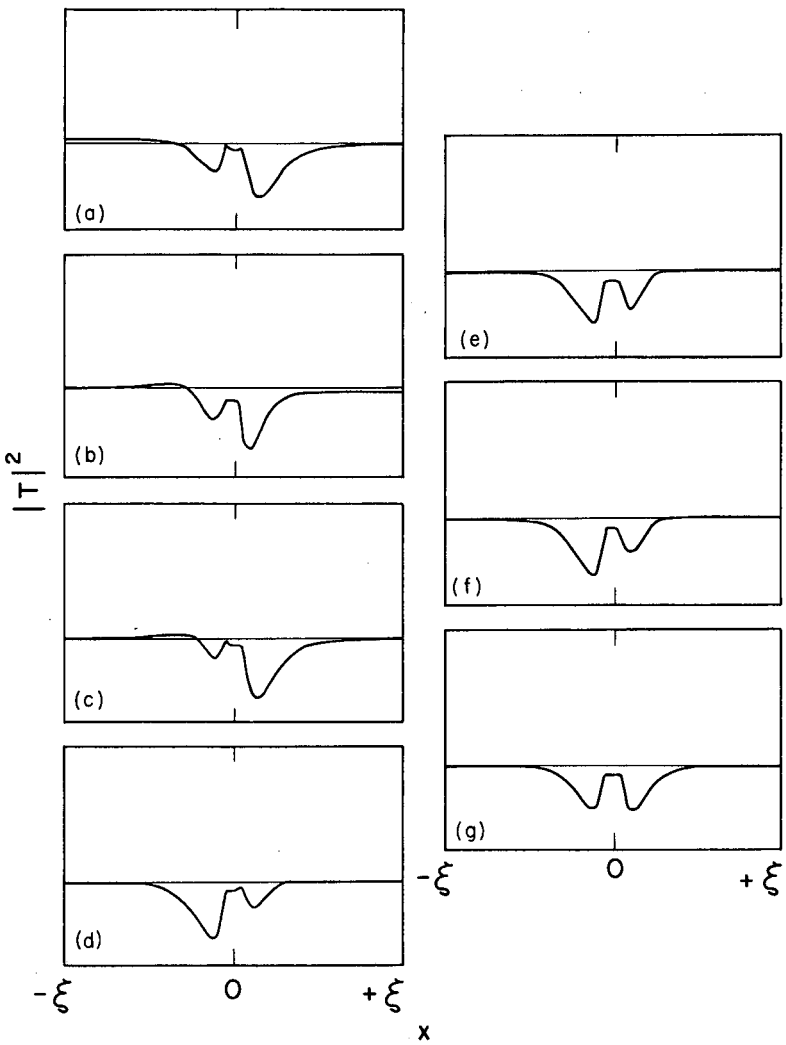

Fig. 11

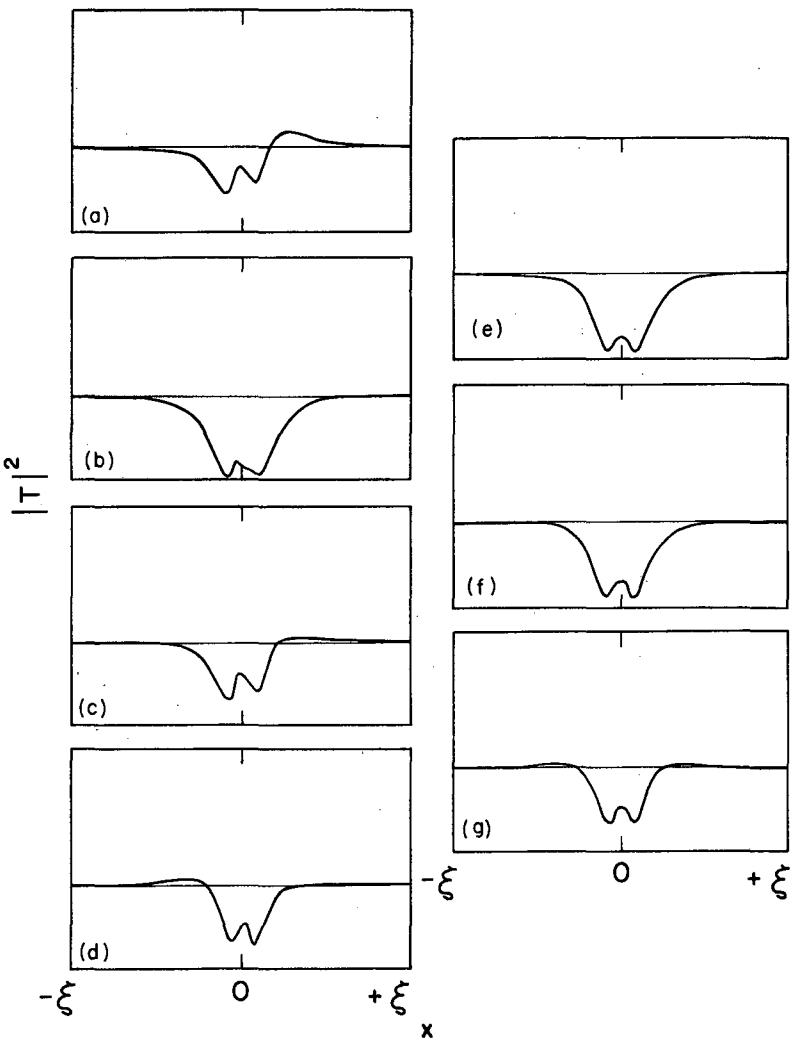

Fig. 12

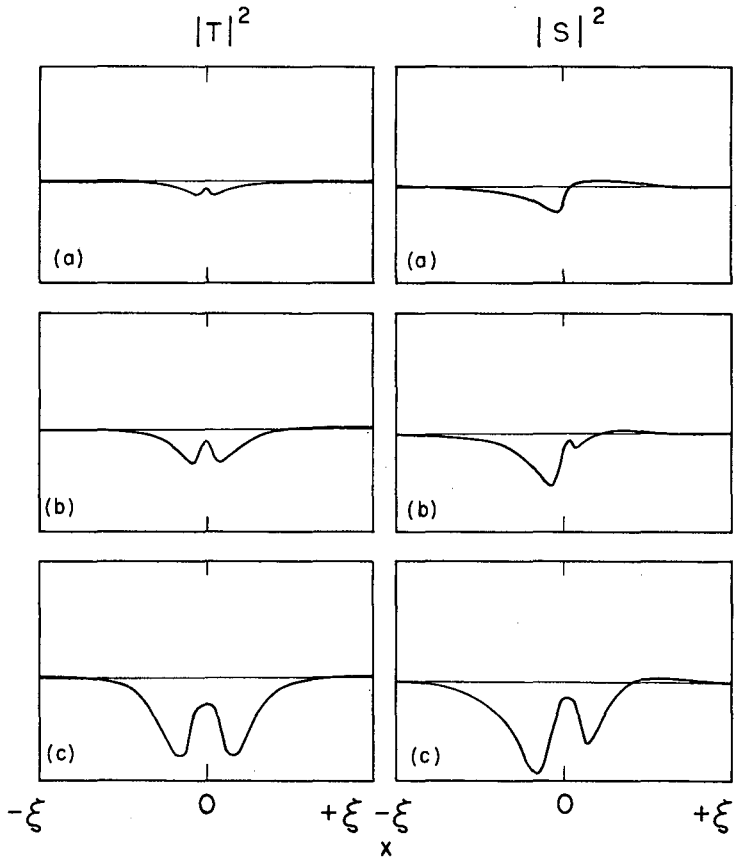

MU-35346

Fig. 13

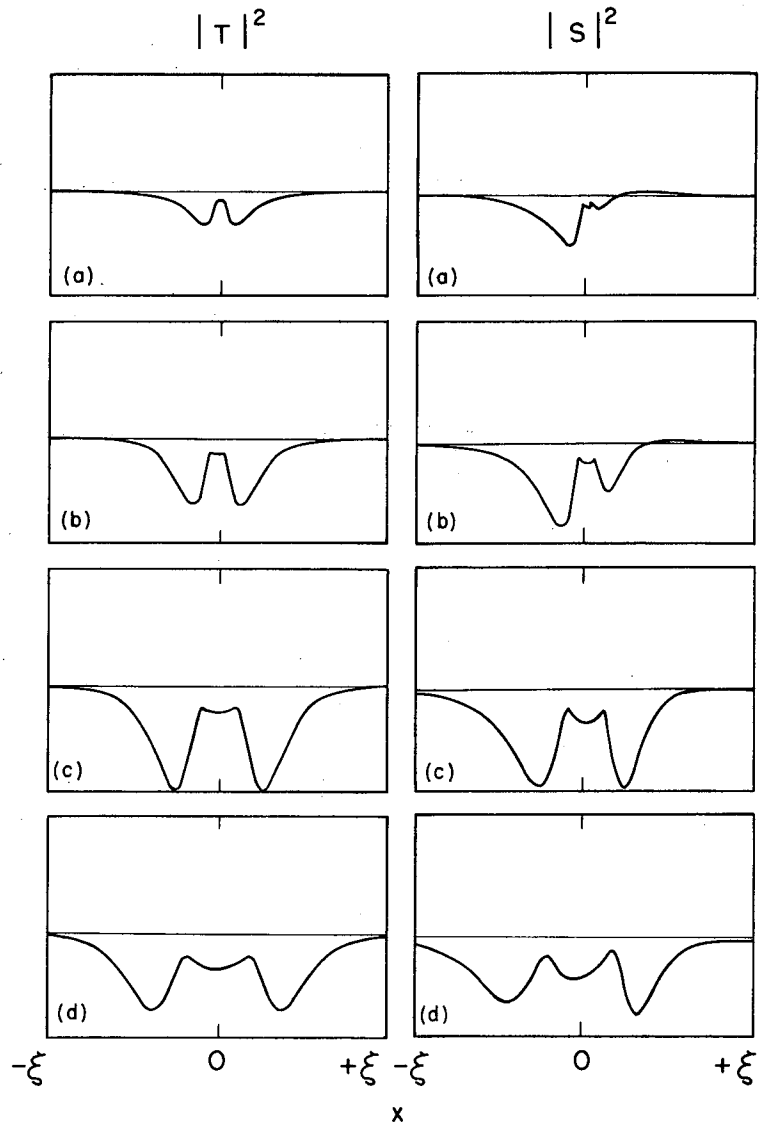

Fig. 14

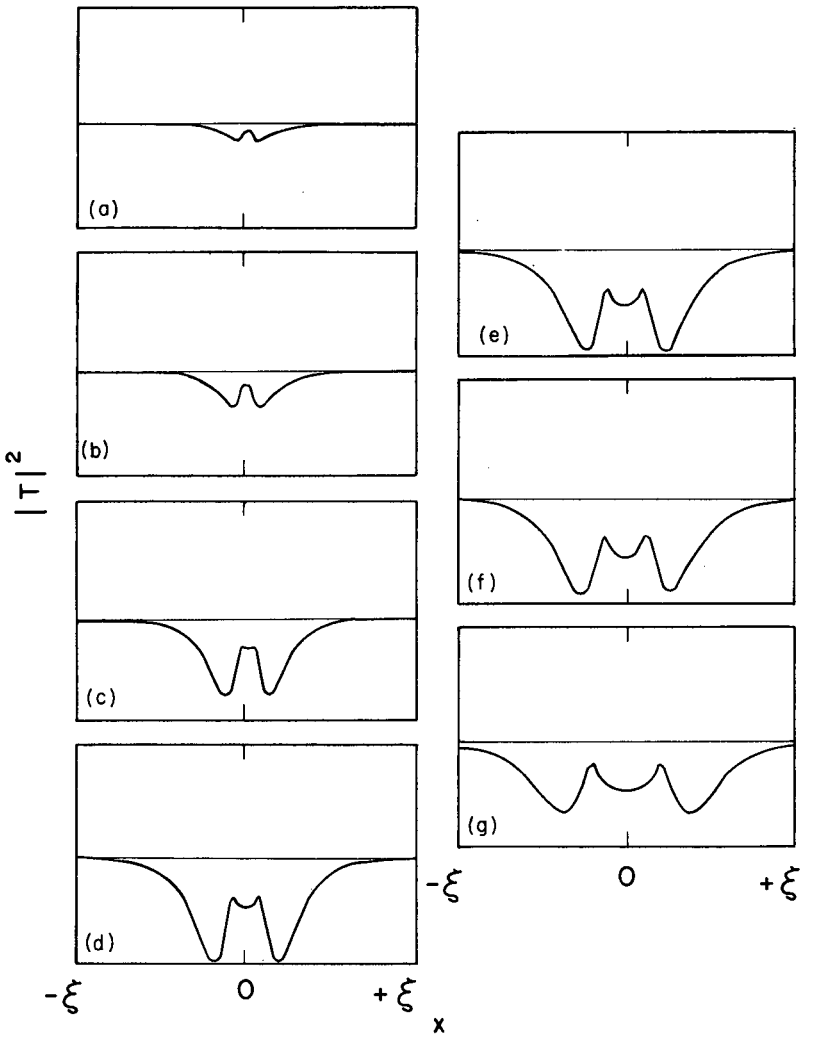

Fig. 15

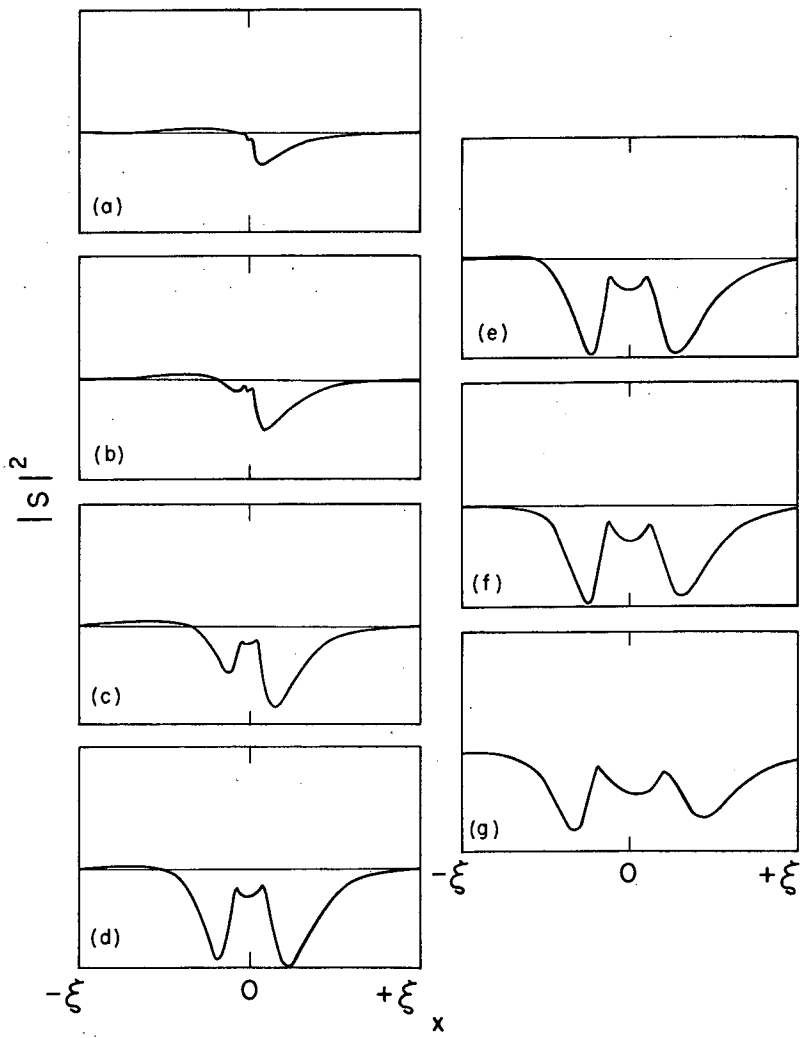

Fig. 16

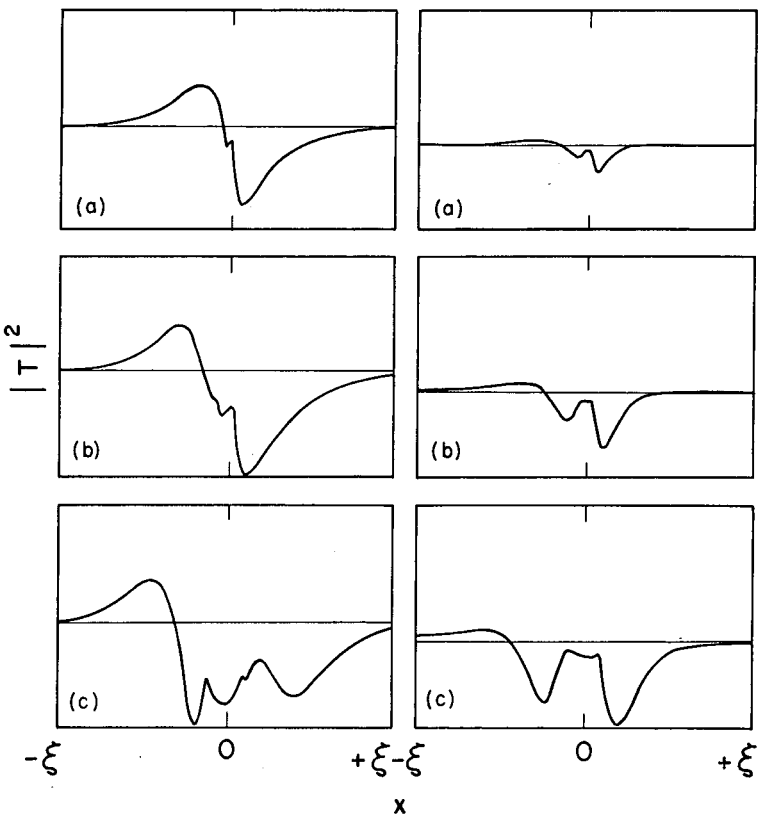

Fig. 17

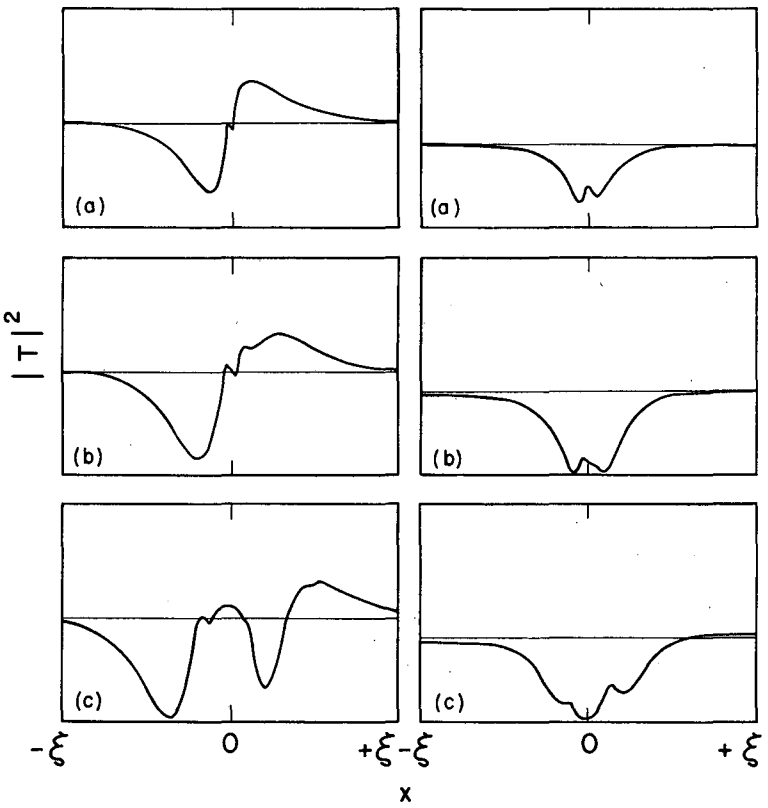

MU-35313

Fig. 18

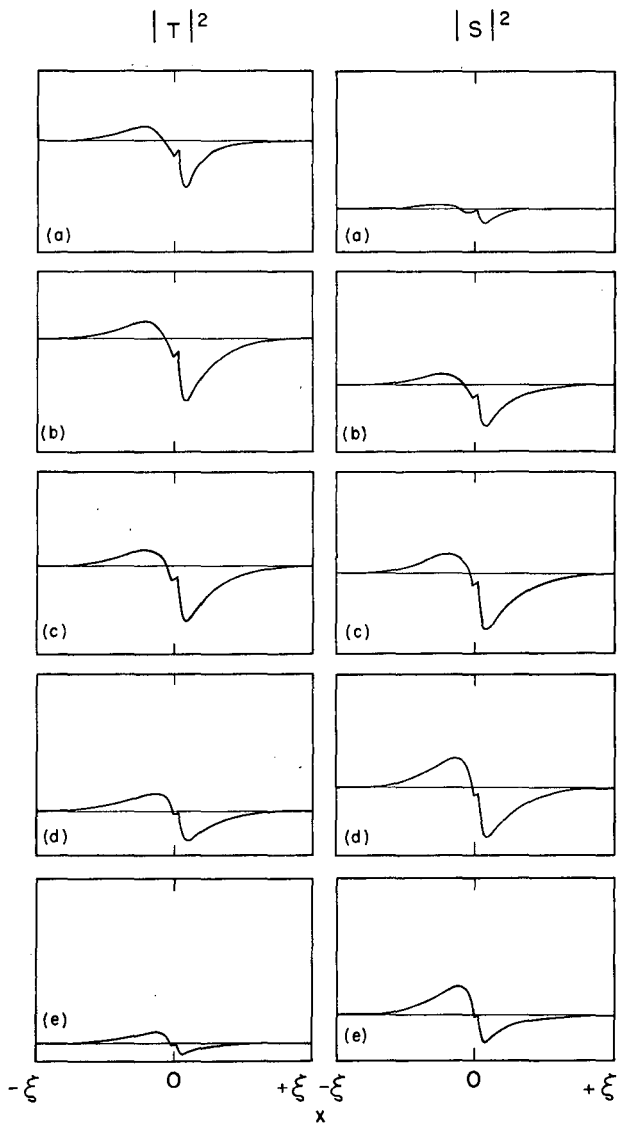

Fig. 19

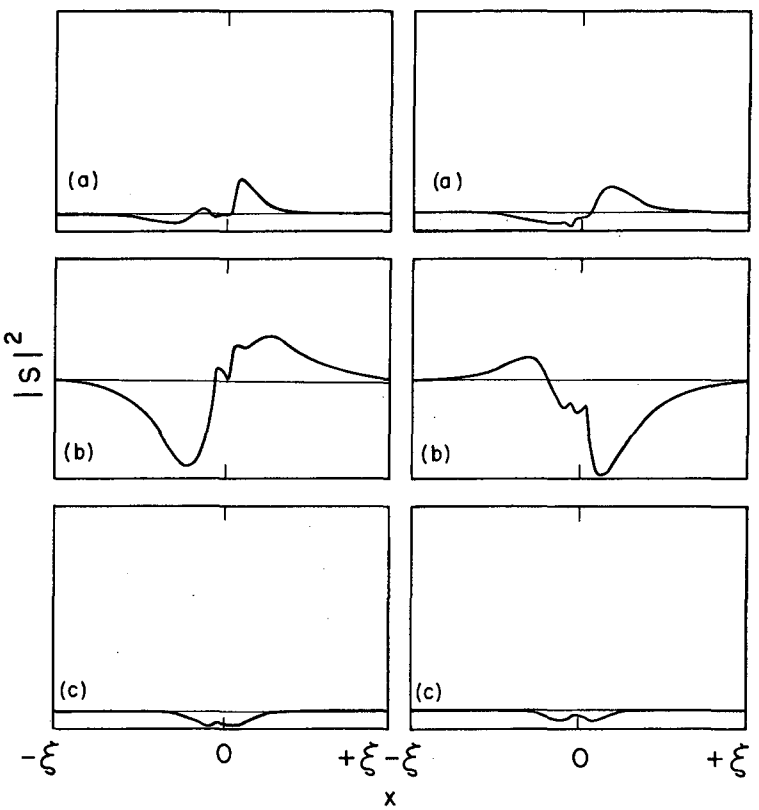

Fig. 20

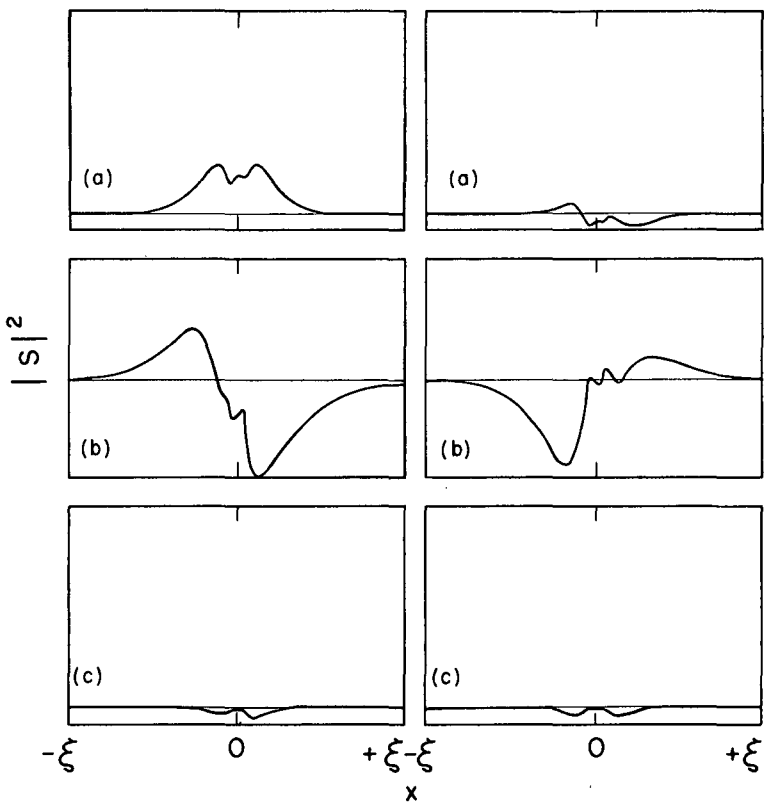

Fig. 21

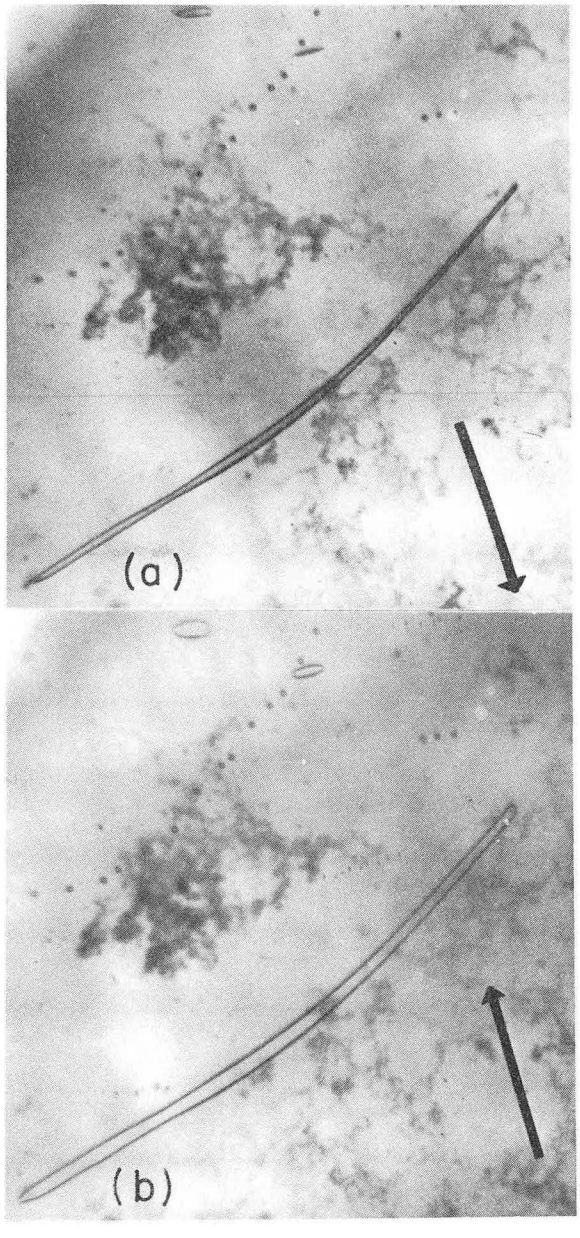

ZN-5323

Fig. 22

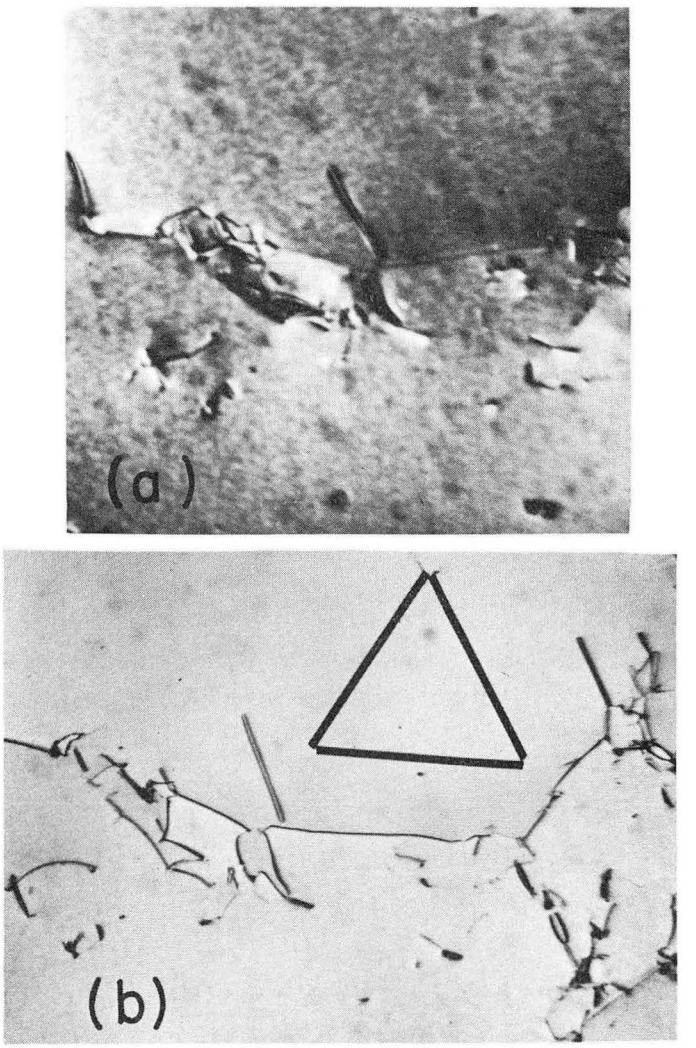

ZN-5324

Fig. 23

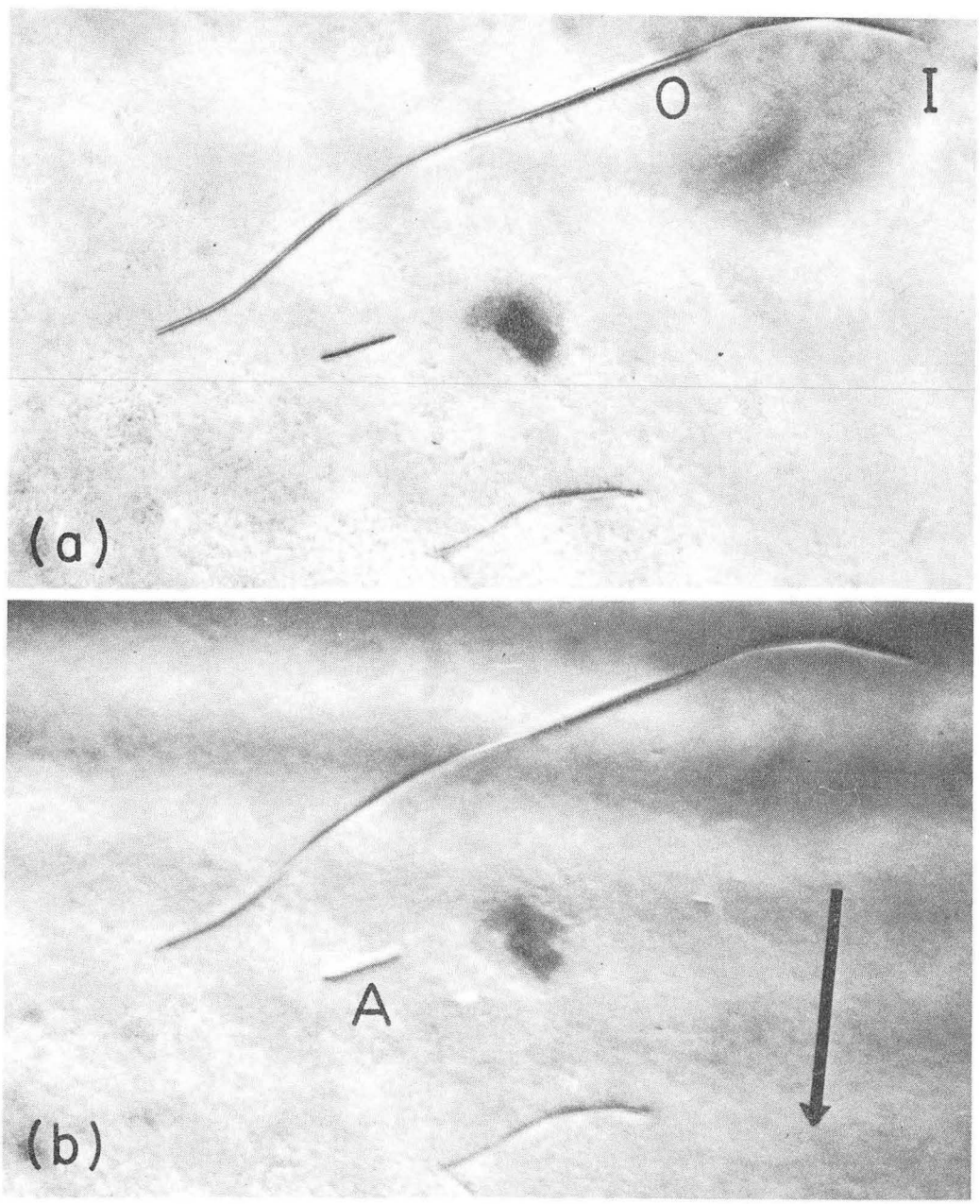

ZN-5325

Fig. 24

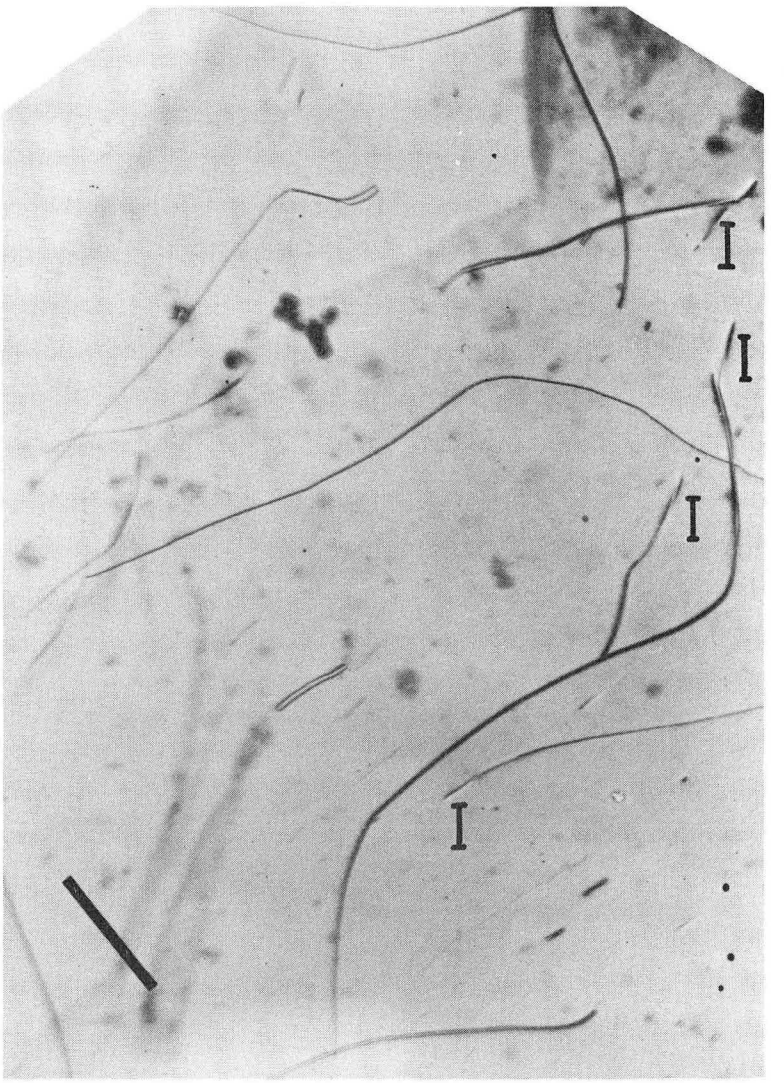

ZN-5326

Fig. 25

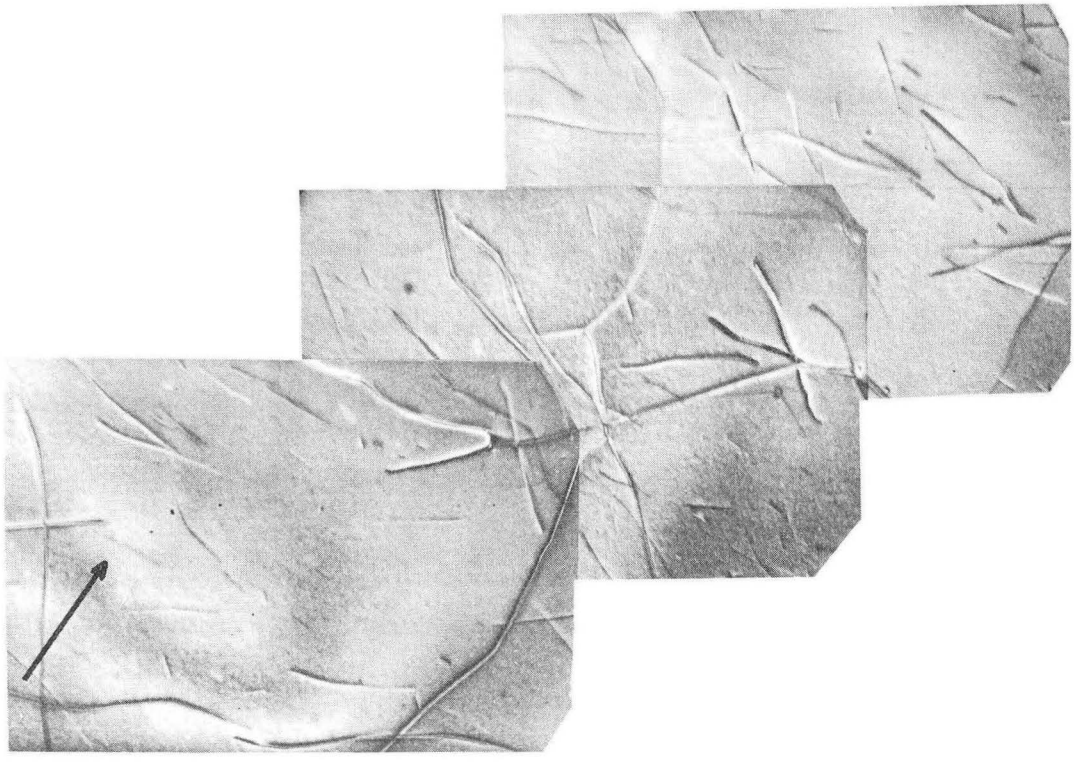

ZN-5327

Fig. 26

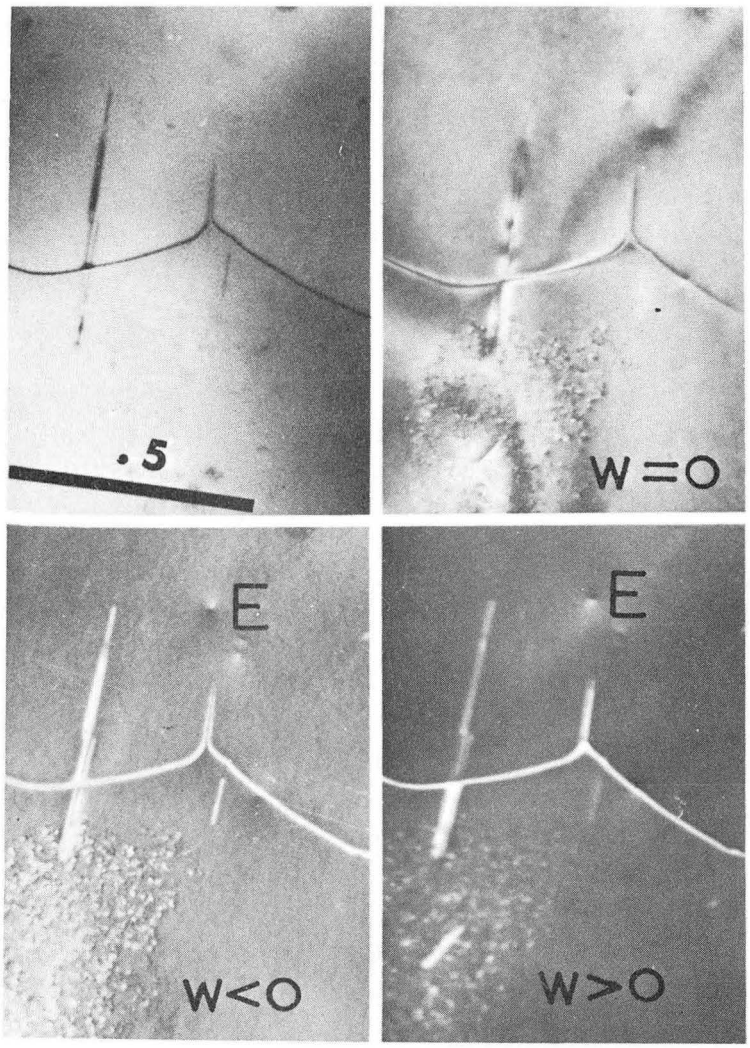

ZN-5328

Fig. 27

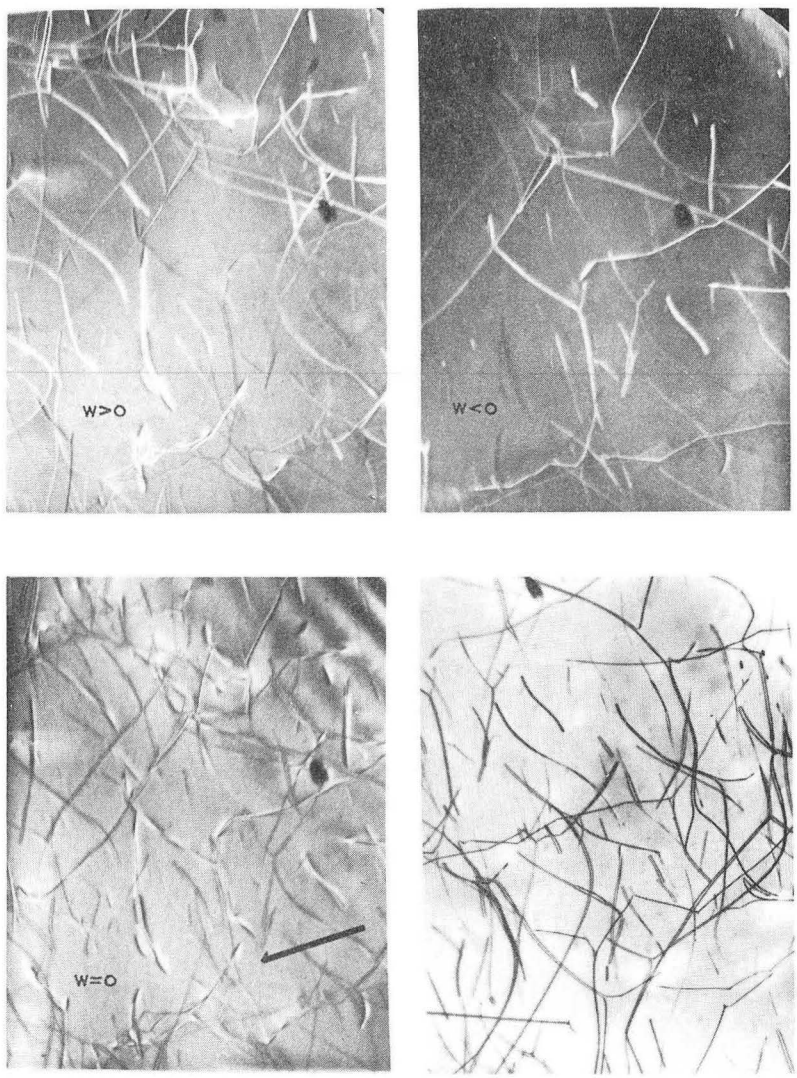

ZN-5329

Fig. 28

CHAPTER 2

DISLOCATION CONFIGURATIONS IN DEFORMED MAGNESIUM OXIDE

Introduction

Having studied the diffraction contrast of dislocation dipoles in detail, we shall now attempt to utilize what has been learned to supply new information on the microscopic features of the plastic behavior of magnesium oxide. Current knowledge of the processes that control the behavior of dislocations in ionic crystals, and therefore determine plastic properties, has come in large part from dislocation etch-pit (for a review see Gilman and Johnston[1]) and transmission electron microscopy[2,3] studies. However, understanding of the motion of dislocations in these materials is based on static observations. For example, the etch-pit technique reveals the positions of the ends of dislocations before and after an increment of plastic strain. Transmission electron microscopy shows the arrangement of dislocations left in the crystal after a slip band has formed. Because dynamic observations generally cannot be made, some uncertainty often remains as to how the observed arrangement of dislocations actually developed.

The most striking result of transmission electron microscopy observations of magnesium oxide has been to show that the largest fraction of the dislocations left in a crystal during formation of a slip band are close pairs of opposite sign or dislocation dipoles. However, uncertainty remains as to the exact ways in which they are formed. The purpose of the present work was to obtain more precise information as to the length, spacing orientation, and type (i.e., interstitial or vacancy) of dipoles and small prismatic loops in deformed magnesium oxide. By studying the effect of varying the temperature of deformation

and ratio of resolved shear stress on primary and cross-slip planes it was hoped that new clues as to the mechanism of dipole formation would be obtained.

A single crystal of magnesium oxide loaded along a <001> direction has four equally stressed {110}<1$\bar{1}$0> systems and unstressed {001} <1$\bar{1}$0> (cross slip) systems. A crystal loaded along a <111> direction has all {110} <1$\bar{1}$0> systems unstressed and three equally stressed {001} <1$\bar{1}$0> systems. A crystal deformed along <001> usually is divided into regions where one of the four possible slip systems has predominated; hence, it is relatively easy to obtain electron microscope specimens from regions that slipped primarily on one system. A difficulty encountered when interpreting dislocation substructures of crystals loaded in a <100> direction is that at the temperatures at which the motion of dislocations on {001} becomes significant, dislocation climb also occurs. Therefore there are alternate mechanisms by which moving dislocations can leave their glide planes. Thus, one is not sure whether it is screw or edge oriented parts of a dislocation loop that escape from the original glide plane. By loading a crystal in a direction near <111>, such that both the normal {110} slip planes and their companion {001} cross-slip planes sustain large resolved shear stresses at a temperature too low for appreciable climb, it may be possible to better evaluate the role of cross-slip.

All previous transmission electron microscopy studies of deformed magnesium oxide have utilized foils with surfaces polished parallel to the {001} cleavage plane. An {001} foil has several disadvantages. The first and perhaps the greatest objection is that only a thin strip of any slip plane, bounded by the two foil surfaces, can be examined.

This is because the {110} slip plane lies at 45° or at 90° to the surface of an {001} foil. The strip of slip plane that is observed is less than one micron wide, and thus, very few long segments of dislocation can be seen. Secondly, any long segment that is included must lie nearly parallel to the surfaces. Therefore, there is a tendency for it to rotate during the chemical thinning of the foil so as to shorten its length by becoming more nearly perpendicular to the foil surfaces. As a result the substructure observed may not be entirely representative of the as-deformed state. Finally, the dislocation substructure is viewed in projection, making it difficult to observe fine details, and to perform and interpret electron diffraction contrast experiments. To avoid these difficulties, the present observations were made on foils cut parallel to an active {110} slip plane. This geometry was not used with high temperature <111> loading axis specimens that deformed primarily by {001} slip. Therefore, observations were made in foils prepared from sections cleaved parallel to the active {001} slip plane.

Experimental Technique

All magnesium oxide crystals examined were obtained from the Muscle Shoals Electrochemical Corporation, Tuscumbia, Alabama. The principal impurities were calcium oxide, aluminum oxide, and silicon oxide resulting in an overall purity of 99.95%. <001> loading axis specimens were cleaved into bars of approximately square cross section. The specimens for <111> loading were diamond-sawed so that two of the four vertical faces were {110} planes. When deviations from the exact <111> axis were required, the axis of rotation was always chosen normal to the {110} vertical faces.

The specimens were chemically polished and then loaded in compression, using the technique of Hulse, et al.[4] All specimens were deformed just past the onset of macroscopic plastic flow, to about 0.5% overall strain, unless otherwise noted.

The deformed <001> loading axis specimens were then etched in two parts H_3PO_4, one part H_2SO_4 to reveal the presence of slip bands; the same etchant was used on the {110} faces of the <111> loading axis specimens. A platelet from the area selected was diamond-sawed parallel to the locally active {110} slip plane. In the case of {001} slip, platelets were cleaved from the selected region. The thickness of the sections was typically 0.050-0.060 inches. Thin foils suitable for transmission electron microscopy were prepared from these platelets by chemical polishing in conc. H_3PO_4 at 150° - 160°C, and were examined in a Siemens Elmiskop I equipped with a two-axis goniometric specimen stage.

An additional benefit of making observations perpendicular to an active slip plane is that contrast phenomena due to dislocations are particularly simple to interpret. The Burgers vector of the dislocations must itself be contained in the plane of the foil. For {110} slip plane sections, the most convenient set of diffracting planes are the {220} family, for which $\underset{\sim}{g} \cdot \underset{\sim}{b} = 2$; dislocation images were always recorded for conditions in which only this beam was responsible for the image contrast.

Experimental Results

I. General Description of the Dislocation Arrangements

Figures 1, 2, and 3 are all slip plane sections of crystals deformed at room temperature. There are several salient features common to these and all other such sections examined. The damage was almost exclusively present as dislocation dipoles of greatly varying width, length, and

orientation. The dipoles longer than a few microns in length had relatively large interdislocation distances, typically about a hundred Burgers vectors. Deviations from edge orientation were frequent, particularly for the longest dipoles; several dipoles were at, or extremely near, pure screw orientation. The long dipoles usually were interconnected at three-fold confluences, and sometimes showed evidence for having had their component dislocations cross over each other. Many of the medium length dipoles, 0.5 to 2 microns long, had both their ends closer to edge orientation than the central part, giving them an "S-shaped" configuration. There was a whole spectrum of dipole widths; the range of separation of the glide planes of the two dislocations being anything between a few interatomic distances up to a few hundred. A correlation also existed between the lengths of dipoles and their spacing and orientation. The shorter the dipole, the narrower its spacing tended to be and the closer it generally lay to edge orientation.

Although single dislocations in edge orientation were seldom seen, the slip plane sections allowed observations to be made on long segments of dislocation in near screw orientation. Figure 3 shows a typical screw dislocation with several cusps along its length. Though only barely visible, there are very narrow dipoles associated with these cusps; this point will be discussed later. Long dislocations, having an average orientation near screw, such as the one in Fig. 3 and those in Fig. 4 often had cusps along their length that pointed in both directions. This effect also observed by Fourie in slip plane sections of copper single crystals[5] is probably caused by the reversal of the shortest dipoles during retreat of the screw dislocation when the external stress is relaxed upon unloading.

II. Presence of Weakly Visible and Invisible Dipoles

The diffraction contrast image due to a dipole must become weaker and finally disappear as the spacing between the two dislocations decreases. Several of these weak images can be seen in Fig. 5. That these images do correspond to fine dipoles having the same Burgers vector as that of the active system was confirmed by showing that they disappear along with all the other images for a {200} reflection. Of the six <110> Burgers vectors there are only two for which the dislocations are out of contrast (i.e.,invisible) for images formed by a {200} reflection. One of the possible dislocations is that of the active system with Burgers vector in the plane of the foil. The other is that having a Burgers vector perpendicular to the foil. plane. Dislocations of this other system were sometimes observed if the specimen happened to be tilted quite far from the exact <110> orientation. However, the frequency of the faint images, the fact that they were often quite far from being parallel to the tract of the perpendicular {110} plane, see Fig. 5, and the fact that they appeared and disappeared along with all the rest of the images due to the active system makes it unreasonable to assume that they have a Burgers vector different from that of the primary system.

The calculations of Chapter 1 have shown that if the spacing of an edge dipole located centrally in a thin foil becomes less than about 40 Burgers vectors, the image width and diffracted intensity begin to decrease rapidly. Physically, the faintness of the image of a narrow dipole is a result of the mutual cancellation of the strain fields of the component dislocations. For the $\underset{\sim}{g} \cdot \underset{\sim}{b} = 2$ case with W = 0, even for a foil having relatively clean flat surfaces, a centrally located dipole having a spacing of less than six Burgers vectors probably will be invisible.

At such narrow dipole spacings, the approximations of the dynamical theory and of linear elasticity are not altogether sound, and also the smallest fluctuation in intensity that could be noticed depends on the uniformity of the background intensity. Thus, the estimate probably is accurate within a factor of two.

Often, the existence of extremely narrow dipoles could be inferred from the appearance of the patent screw dislocation. As the dipole spacing decreases, the dipole image becomes weaker until it finally disappears, being indistinguishable from the background. However, a contrast effect remains at the mouth of the dipole where it is attached to the screw dislocation. By changing the sign of the Bragg angle deviation parameter, W, a dipole image will always shift from inside the dipole to outside, or vice versa. This is true because the image of a dislocation lies to one side of the actual position of the dislocation; changing the sign of W has the effect of changing the side of the dislocation at which the image lies. If the invisible dipole is in inside contrast, there will be a local enhancement of the image width of the screw dislocation at the point of juncture with the dipole. If the dipole is in outside contrast, there will be a diminution of the screw dislocation image width there. This useful effect arises because the dipole spacing gradually increases where it joins the screw dislocation. Thus, even though the majority of the dipole is invisible, a small length at the junction with the screw dislocation becomes sufficiently wide to give observable contrast. Figure 6 at D shows an example of this effect. Similar narrow dipoles would go unnoticed if they were not associated with a screw dislocation, unless, as is the case at N in Fig. 3, they happen to lie close to the foil surface. As was seen in Chapter 1, proximity of a surface to a dipole of any spacing will, in general, widen and strengthen its image.

III. Fine Structure of Dipoles

A fine structure is apparent in the dipoles marked O in Fig. 7. The image width changes abruptly part way along the length. Changing the sign of the Bragg angle deviation parameter, W, by tilting the specimen, has the effect of widening the narrow end of the dipole and vice versa. An example of this is shown in Fig. 8 at O. This diffraction contrast behavior rules out the possibility that the dipole simply changes its spacing at these junctions. For the wide portions of the dipoles at O, the image lies outside both component dislocations; the reverse is true for the narrow portions. Therefore, as a result of specimen tilting, the part that was in outside contrast changed to inside contrast and vice versa. This diffraction contrast behavior suggests that these junctions are the orientation junctions described by Gilman[6]: a region of transition from one stable dipole orientation to the other. Alternatively, they could be "spacing" junctions, where the orientation of the dipole remains unchanged, but the dipole is interstitial type on one side and vacancy on the other. In this case, the dipole spacing decreases until it is zero exactly at the junction, and then increases again, the dipole having changed its nature. Either of these models can explain the contrast results. However, an orientation junction in a dipole of reasonable spacing should have a continuous image in the region of the junction because the two dislocations of the dipole are never close enough to cause complete cancellation of their strain fields. At a spacing junction on the other hand, the dipole image should be discontinuous because the separation actually goes to zero. Strain field cancellation should cause the image to disappear for a short distance. Examples of both types of image are shown in Fig. 9.

IV. Interstitial Versus Vacancy Dipoles

From the point of view of understanding how they are formed, it is of considerable interest to try to determine whether one type or both types of dipole are produced during plastic deformation. An interstitial dipole in edge orientation has its extra half plane in the interior of the dipole; a vacancy dipole has its extra half plane outside the dipole. The results of Chapter 1 indicate that a reversed Ashby-Brown strain contrast criterion[7] should obtain for narrow dipoles situated near a surface. In a 500°C specimen, dark field experiments were carried out to determine whether the narrow dipoles near surfaces were vacancy, interstitial, or both by consideration of the orientation of their black-white image with respect to the operating diffraction vector. In given fields of view, such are shown in Fig. 10, with the foil at the exact Bragg angle, both black-white image orientations were found. Therefore, both types of dipole are present in the as-deformed state.

The accuracy of the above determination depends on the subjective correlation of the intensity of the black-white dipole image with its depth in the foil, i.e., it is assumed that the very strongest images are dipoles within one-half an extinction distance of either surface. Because of this uncertainty, the techniques of Appendix II, Chapter 1, were applied to dipoles that intersected a foil surface. Whenever it was possible to apply more than one of these methods, this was done; consistent results were always obtained. Again, both interstitial and vacancy dipoles were found, so that it would appear that both types of dipole are produced during plastic deformation.

V. Effect of Deformation Temperature on the Dislocation Substructure

Figure 5 shows a section from a crystal deformed at 500°C. No significant differences in the dislocation substructures are evident between this specimen and the ones representative of room temperature deformation. However, many very narrow dipoles can be seen particularly well in the central portions of this micrograph. At temperatures greater than about 700°C, etch-pit studies indicate that grown-in dislocations begin to act as sources of dislocations. Figure 11 shows a sub-boundary that apparently acted as a source for long single dislocations. Attempts to measure the local strain in high temperature glide bands, using the technique of Washburn and Gorum[8], failed because the amount of strain became very small. With many potential sources available, the crystal was filled with dislocations at very small strains. Each source sends off several dislocations, but they do not move very far. New sources are activated on parallel planes before dislocations can completely traverse any given slip plane. Attempts to observe slip offsets by optical and electron replica microscopy also proved fruitless, even though slip offsets were easily visible after an equivalent deformation at lower temperatures. Thin foils of crystals deformed at 750°C showed more screw dislocations and some decrease in the number of dipoles (Fig. 12). Also, the dipoles present were, on the average, much shorter and deviated less from edge orientation than those in specimens deformed at lower temperatures. Screw dislocations still were heavily jogged and dragged many very narrow dipoles (see D in Fig. 12). Examples of both jogged screw dislocations and medium length dipoles can be seen in Fig. 6.

At temperatures above 750°C, the climb of edge segments becomes significant. The advent of climb leads to the breakup of dipoles into

strings of prismatic loops. By annealing a crystal deformed at temperature, at 800°C for one-half hour, it was observed that the breakup of very narrow dipoles usually commenced at their ends. The strings of loops formed from the breakup of dipoles frequently were tapered at one or both ends with the inter-loop spacing and loop diameter decreasing as the ends were approached. Figure 13, of a crystal deformed at 850°C, shows examples. This observation shows that the spacing of the original dipoles was not uniform, and that it usually decreased towards the ends of the dipoles.

As was noted by Groves and Kelly,[9] most, but not all, dipoles commenced to break up into loops at their ends. There are several gaps in the strings of loops visible in Figs. 13 and 14. The presence of a spacing junction as previously described would provide an internal position favorable to the initiation of break up and also would explain the presence of gaps in the strings of loops.

The substructures in crystals deformed at 1000°C showed strings of dislocation loops of varying size and length that has been formed from dipoles which all were rather close to edge orientation. In the specimen geometry used in the present experiments, the Burgers vectors and hence the system of the trails of prismatic loops that occur in specimens deformed above 850°C, can be identified by inspection since they exhibit "double-arc" contrast as described by Bell.[10] The image to be expected from a perfect loop is one that has the strongest contrast from the pure edge segments and the weakest contrast from the mixed orientation segments. In MgO, therefore, the double-arc loop image will be one in which the direction of the line connecting the two segments of the loop in weakest contrast, being parallel to the pure edge components, is perpendicular to the projection of the Burgers vector of the loop onto the surface of the foil.

In addition to the loops present, there were single dislocations threading their way through the thin foil. Many of these were quite short, running from one surface of the soil to the other in less than one micron. Also single dislocations frequently crossed over themselves (Fig. 14). Screw dislocations, when observed were always much smoother than those observed at temperatures up to 750°C. By 1000°C, there is rapid climb of edge segments along with a significant increase in mobility of dislocations on {001}. Figure 15 shows typical substructures from a crystal deformed at 1600°C. One must search a long time for any deformation substructure in such specimens for not only is the dislocation density, as determined by etch-pit methods, quite low, 2 $10^6/cm^2$, but also very few dislocations segments lie on any {110} plane for a long distance. The dislocations shown are prismatic loops of very wide spacing, accurately aligned in the pure edge orientation. At J, (Fig. 15) one can see two large jogs. Because of the easier glide of segments on {001} at this high temperature, it is expected that such "super-jogs" could form by the gliding together of many smaller jogs.

VI. Effect of a Large Stress on the {001} Cross-Slip Plane

Figure 16 shows an etched {110} face of a crystal loaded at 600°C in a direction about 5° from <111>. This arrangement gives a resolved shear stress for the {001} $\langle 1\bar{1}0\rangle$ cross-slip system that is about six times the resolved shear stress acting on the normally operative {110} $\langle 1\bar{1}0\rangle$ system. Although the observed slip band traces are still nominally those of a {110} plane, it is evident that the dislocation paths often deviated from {110}. Slip lanes sections prepared from this specimen showed several interesting features. Figures 17 and 18 should be compared with Fig. 7, a specimen loaded along <100> at approximately the same

temperature. Long dipoles were much less numerous and the short ones that were present were often wide at their centers and pointed at their ends, or terminated by intersection with one or both surfaces of the foil. This suggests that the individual screw dislocations and even the dipoles in this specimen have many more small jogs than in the normally loaded specimens. They no longer lie as close to a given {110} plane. Different parts of the same line often appear to have moved quite different distances from the original {110} glide plane, so that when segments of opposite sign meet, they cross over each other rather than form a dipole. The dislocation just to the left of the micron marker in Fig. 18 seems to be stopped in the process of "crossing-over" itself; thus the spacing of its two segments normal to {110} must be many hundreds of Angstroms.

Larger ratios of stress on {001} to that on {110}, obtained by loading in a direction even closer to an exact <111> orientation, produced more indistinct etch patterns, see Fig. 19. However, {110} slip plane sections were much less useful when definite slip bands were no longer recognizable on the etched crystal faces. In this case, the lengths of dipoles and individual dislocation could no longer be determined because they usually intersected one or both surfaces of the foil after a short distance.

The straight rows of etch pits in Fig. 19 are traces of {001} slip planes whose {110} cross-slip planes were only weakly stressed. Wavy rows of etch pits only occurred when, as a result of mutual stressing, dislocations were able to move on both {110} and {001} planes. When the loading axis is deviated from an exact <111> orientation, the {110} planes are stressed; only at the exact <111> orientation are the {110} planes unstressed. Errors in orienting the loading axis along an exact

<111> direction made it experimentally impossible to attain specimens that deformed purely by {001} slip at 600°C. By increasing the temperature of deformation, the ratio of the stress to cause glide on {001} to the stress necessary for {110} glide is decreased.[4] Thus, at sufficiently high temperatures it became possible, in spite of the orientation errors, to obtain specimens that deformed primarily by {001} slip. Figure 20 shows such a specimen.

The etch- pits of Fig. 20 are arranged in tangles and polygonized walls that were developed in a <111> loading axis specimen deformed to 10% strain at 1300°C. The plane of observation in Fig. 20 is a {001} cleavage plane; the edges of the micrographs are parallel to <001> directions. As determined from the weak residual birefringence in regions of incomplete polygonization (see the two right micrographs), the locally active slip plane was a {001} plane perpendicular to the plane of observation. The tangles of dislocations visible in such regions were aligned approximately parallel to the trace of the active slip plane, whereas the rows of dislocations in the areas of more complete polygonization were perpendicular to the slip plane (see the two left micrographs).

{001} slip plane sections prepared from the specimen of Fig. 20 showed that tangles of edge dislocations (Fig. 21) and subboundaries (Fig. 22) were the most recurrent features of the substructures. Diffraction experiments indicated several {001} systems participated in the deformation. No dipoles or strings of prismatic loops were ever found. Dipoles are formed during glide on{110} because of the lack of mobility of dislocation segments on {001}. In the case of {001} glide, however, segments can easily move on {110}, and dipoles should not occur. In fact, it should be common for dislocations gliding on {001} to leave

their glide plane and lie in the {110} cross-slip plane. There are several places in Fig. 21 where dislocations lie parallel to the trace of the {110} cross-slip plane, i.e., lie in screw orientation. At such locations, {001} glide dislocations probably can readily cross-glide to the {110} plane.

Discussion

Most of the information obtained in the present experiments can be interpreted directly in terms of the dipole formation mechanism of Washburn (see ref. 3, p. 317). However, there also are certain features of the dislocation substructure which will be dealt with in more detail because they were not treated explicitly in the earlier work. We shall begin by describing the dipole formation mechanism. Consider a length of screw dislocation that has acquired a jog of several Burgers vectors. Continued motion of such a dislocation results in the growth of a dipole. Frequently, the spacing of fine dipoles was shown (by their diffraction contrast) to change continuously along their lengths. This can only be explained if new jogs are formed frequently on the screw parts of the loop and are able to glide to the growing dipoles. Fine dipoles can be terminated by this process, since it is only necessary that the numbers of jogs of opposite sense that have run into it become equal. It is not reasonable to suppose that the rates of advance of the two loops of dislocation on either side of a growing dipole will always remain the same. Therefore, some trailing dipoles will turn away from pure edge orientation as they extend. If one of the loops gets far enough ahead of the other, the dipole will find itself in pure screw orientation. For small spacings of only a few Burgers vectors, this will always result in annihilation of the screw dipole by cross-slip, leaving the edge-oriented part of the

dipole closed at both ends. The forward loop of dislocation now can continue to expand in the direction parallel to the Burgers vector and will run rapidly along the screw dislocation, terminating any attached dipoles by annihilation of the connecting screw segments until it encounters another forward segment of the line having a significant edge component. Here a long new segment of dipole will be formed where the two edge dislocations of opposite sign that have followed different paths through the crystal meet. The net result of the above process is that several dipoles of small spacing have been terminated, a new length of screw dislocation quite free of jogs, has been laid down a few microns ahead of its former position, and a long new segment of dipole, having a spacing which includes the algebraic sum of all those that were terminated, has been formed. The entire process can then repeat itself.

Only dipoles of relatively small spacing can be terminated by this mechanism. When the distance between the glide planes of the two dislocations exceeds a critical distance, the mutual attraction of the two dislocations is not large enough to cause cross-glide on {001} even for the segments of dipole lying in pure screw orientation. Therefore, according to this mechanism, dipoles of spacing greater than some critical value should be very long and irregular in shape, even having segments that lie in pure screw orientation. This is indeed the case (see for example Fig. 3). On the basis of the present experiments the minimum spacing for very long dipoles containing segments in pure screw orientation was estimated to be 40 Burgers vectors which corresponds to a critical stress for cross-slip or glide on {001} about 35 times greater than the critical stress for {110} glide in the same crystal. The maximum spacing to which a dipole can grow is of course determined by the applied stress.

It is given by the spacing at which the applied stress can separate the two parallel dislocations. Growth of a few dipoles to this upper critical spacing is thought to be the mechanism by which a slip band widens in a crystal having a few dislocation sources. The lack of long dipoles of wide spacing in specimens deformed at temperatures greater than about 700°C lends further support to this idea. The activation of grown-in dislocations as sources precludes the need for the generation of sources by the growth of a few dipoles; it also yields a length of screw dislocation greater than at low temperatures. Because the strain in such crystals is uniformly distributed, i.e., the local strain is approximately the macroscopic strain, it can be concluded that each screw segment must not, on the average, move across a very large area of its slip plane. This is in distinction to the situation at lower temperatures when the sources are presumably wide dipoles; in this case, the strain in a slip band may be an order of magnitude greater than the macroscopic strain.

According to Washburn's model, long dipoles should curve frequently, sometimes having segments in pure screw orientation. Some of these kinks may subsequently straighten out, the regions of sharp curvature being eliminated by glide. There was evidence that some dipoles with no predominantly screw segments remaining may once have had them: The long dipoles often contained junctions at which there was a change from one of the stable orientations of an edge dipole to the other. In the projection onto the glide plane, the dislocations cross each other at such a junction. These cross-over or orientation junctions will only be formed easily when a part of the dipole is brought at least momentarily into a mixed screw-edge orientation (see the Appendix). Two edge dislocations that are driven together by an applied stress to form a dipole will not

be able to pass as viewed in the slip plane projection, and will be held up by their strong mutual interaction just past the first of the two stable positions. However, when two dislocations of screw orientation are driven together by a stress they will cross over one another. As viewed in the slip plane section, the equilibrium position corresponding to zero applied stress occurs when one screw dislocation is directly above the other; this configuration is retained even for dipoles that have about equal edge and screw components. The applied stress will drive the dislocations beyond this equilibrium configuration to an extent that is determined by the deviation from the pure screw orientation. Thus, for a curving dipole, the segments where there are about equal parts of edge and screw component will take up the second of the two stable configurations rather than the first. However, the portion of the dipole near pure edge orientation will still be in the first configuration. Once an orientation junction has been nucleated it may glide along the dipole under the action of the applied stress. Therefore the entire dipole eventually may be changed over to the second orientation. Orientation junctions might be expected to become trapped where there are jogs on the dislocations or where local internal stresses oppose the applied stress.

As a result of contrast experiments, it was determined that both vacancy and interstitial dipoles were present in deformed crystals of magnesium oxide. This conclusion is consistent with the geometrical nature of the dipole formation mechanism. There should be no preference for the nucleation of one type of dipole over the other because the nucleation depends only on the probability of the collection of a few jogs of the same sign; as long as both types of jog are present, both types of dipole should be formed.

The apparent absence of single edge dislocations is caused by the difference in velocities of screw and edge dislocations at a given stress level. Screw dislocations travel at a velocity about two orders of magnitude slower than that of edge dislocations moving under the same stress.[1] The many dipoles associated with the screw dislocations exert a drag that accounts for the retardation. As a dislocation loop expands from a source it will rapidly become very much elongated in the direction of the active Burgers vector; the loop will be almost entirely in screw orientation with only a short length of edge orientation near each end. Thus segments of single edge dislocation should be rarely seen.

The effect of a high resolved shear stress on the {001} cross-slip plane was to decrease the number of fine dipoles and increase the spacing of those that were formed. Also, both individual dislocations and dipoles often lay at a small angle to the {110} plane. They frequently passed from top surface to bottom surface of a {110} slip plane section in a distance less than ten times the thickness of the foil. This means that the lines contained a high density of small jogs of the same sense. No evidence was obtained for the formation of pairs of large jogs as would be expected from the double cross-slip mechanism. The low temperature deformation substructure and the changes in structure due to high cross-slip stress seem more consistent with the assumption that the basic mechanism by which a pure screw dislocation leaves its original glide plane is the nucleation and separation of a pair of jogs of length equal to a unit Burgers vector. Because of the high density of narrow dipoles, it would seem that this process must occur frequently. Impurity atoms may play an essential role in the process. A high stress on the cross-slip plane should aid this event by helping to separate the two jogs when

they happen to be of the right signs. It should also assist their glide off the screw part of the loop, making the nucleation of a new dipole less frequent. A screw dislocation should tendto drift farther and farther away from its original {110} layer of atoms.

The effect on the deformation substructure of increasing the deformation temperature above 700°C was very similar to the effect of high cross-slip stress. Fewer fine dipoles were formed and those that were found were of larger and larger spacing as the deformation temperature increased. An increase in temperature should also increase the frequency of jog-pair formation on screw segments and increase the glide mobility of jogs. However, interpretation of the changes in deformation substructure are complicated by the fact that dislocation climb and operation of elements of the grown-in dislocation network as sources begin to become important in about the same temperature range. For the high temperature and high cross-slip stress experiments, it also was virtually impossible to achieve conditions where only one slip system operated. Therefore, dislocation intersections may also contribute jogs to the moving screw dislocations. It seems highly unlikely that dislocation intersections can be responsible for all the large number of fine dipoles that are formed during the low temperature deformation of a good crystal on a single system and for their gradual changes in spacing. However, the possibility cannot be completely discounted in the high temperature and high cross-slip stress specimens..

APPENDIX

Calculation of the Equilibrium Configuration of a Mixed Orientation Dipole

We shall consider only dipoles whose component dislocations are parallel. The component of force per unit length of dipole between the two component dislocations of a pure screw orientation dipole, resolved into the glide plane, is $F_s = -\frac{Gb^2}{4\pi D}\sin 2\theta$.[11] . For a pure edge dipole, the force is $F_e = -\frac{Gb^2}{4\pi(1-\nu)D}\sin 2\theta \cos 2\theta$.[11] . Here, G is the shear modulus, D is the perpendicular spacing between the slip planes of the individual dislocations of the dipole, ν is Poisson's ratio, b, the magnitude of the Burgers vector and θ, the angle between the perpendicular connecting the two dislocations and the slip plane. If ψ is the acute angle, in the slip plane, between the Burgers vector of the dipole and the dislocation lines, the inter-dislocation force of a mixed orientation dipole resolved into the glide plane is,

$$F_M = -\frac{Gb^2}{4\pi D}\sin 2\theta\left[\cos^2\psi + \frac{\cos 2\theta \sin^2\psi}{(1-\nu)}\right] \qquad (1)$$

When $\psi = 0$, Eq. (1) represents the screw dipole case, and the edge dipole case when $\psi = \frac{\pi}{2}$. In order to determine the equilibrium configuration for an arbitrary ψ, we must find the equilibrium angle, θ_E, that corresponds to a configuration with zero glide force between the component dislocations. For a pure screw dipole ($\psi = 0$), the dislocations are one above the other and $\theta_E = 90°$. As the edge component increases, θ_E remains 90° until a value of ψ_o such that $\cot^2\psi_o = \frac{1}{1-\nu}$ is reached. In the case of magnesium oxide, $\psi_o = 42.2°$. As ψ increases past ψ_o, θ_E decreases, rapidly at first and then more slowly. Finally, when $\psi = 90°$, $\theta_E = 45°$. Figure 1 portrays the behavior described above. The equilibrium

angle, θ_E, and the lateral dislocation spacing in units of the vertical glide plane spacing are plotted as a function of the orientation of the dipole. It should also be noted that up to ψ_o, there is only one equilibrium position. For $\psi > \psi_o$, however, there are two equilibrium configurations, symmetrical to the glide plane normal, at θ_E and $180° - \theta_E$.

The energy per unit Burgers vector length of a mixed orientation dipole can also be found from the relevant formulae for pure edge and screw orientation dipoles.[11] The result is

$$E = \frac{Gb^2}{2\pi}\left[(\ell n\, D/b + \ell n\, 1/\sin\theta)\left(\frac{1-\nu\cos^2\psi}{1-\nu}\right) - \frac{\cos 2\theta \sin^2\psi}{2(1-\nu)}\right] \qquad (2)$$

For a given value of ψ, the energy has a minimum at θ_E and $180°-\theta_E$, corresponding to the equilibrium configurations. This is a very deep minimum for a pure screw dipole ($\psi = 0$). As the edge component is increased, the energy minimum becomes increasingly shallower. Up to $\psi \leq \psi_o$, the dislocations remain one above the other, but they become more weakly bound at this relative position as $(\psi_o - \psi)$ decreases. Exactly at $\psi = \psi_o$, $\frac{\partial E}{\partial \theta}(\theta)$ is zero to second order in $(\theta - \theta_E)$, and the dislocations can easily be displaced laterally with respect to each other. For $(\psi-\psi_o) > 0$, two energy minima, separated by an energy maximum, occur. The position of the maximum is at $\theta = 90°$. As $(\psi - \psi_o)$ increases, the height of that maximum and the depth of the minima increase. The difference in energy between the energy minimum and energy maximum, i.e., the energy barrier that must be surmounted in going from one position of stable equilibrium to the other, is $\Delta E = E(90°)-E(\theta_E) =$

$$= \frac{Gb^2}{2\pi(1-\nu)}\left[\cos^2\theta_E \sin^2\psi - \ell n\left(\frac{1}{\sin\theta_E}\right)\left(1 - \nu\cos^2\psi\right)\right] \qquad (3)$$

Figure 2 shows ΔE as a function of the dipole orientation angle ψ.

Because there is only one equilibrium configuration up to $\psi = \psi_o$, $\Delta E = 0$ for $\psi \leq \psi_o$. $\Delta E\ (\psi = 45°) = 2 \times 10^{-3} Gb^3$ per unit Burgers vector length of dipole, but increases repidly after that.

In conclusion, because the attractive force between the dislocations of a screw dipole is greater than the attractive force between the dislocations of an edge dipole, the equilibrium orientation of a mixed dipole remains that of a pure screw orientation dipole up to an orientation $\psi_o = 42°$. For ψ near ψ_o, the applied stress can greatly affect the relative positions of the two dislocations. When $\psi \lesssim \psi_o$, a shallow single energy minimum is present, and the dislocations will prefer to be one above the other. When $\psi \gtrsim \psi_o$, two shallow energy minima separated by a small energy maximum are present; in this case, it should be very easy for the applied stress to flip the dipole from one stable orientation to the other. Thus, the nucleation of an orientation junction by the applied stress should readily take place for dipole orientations close to ψ_o.

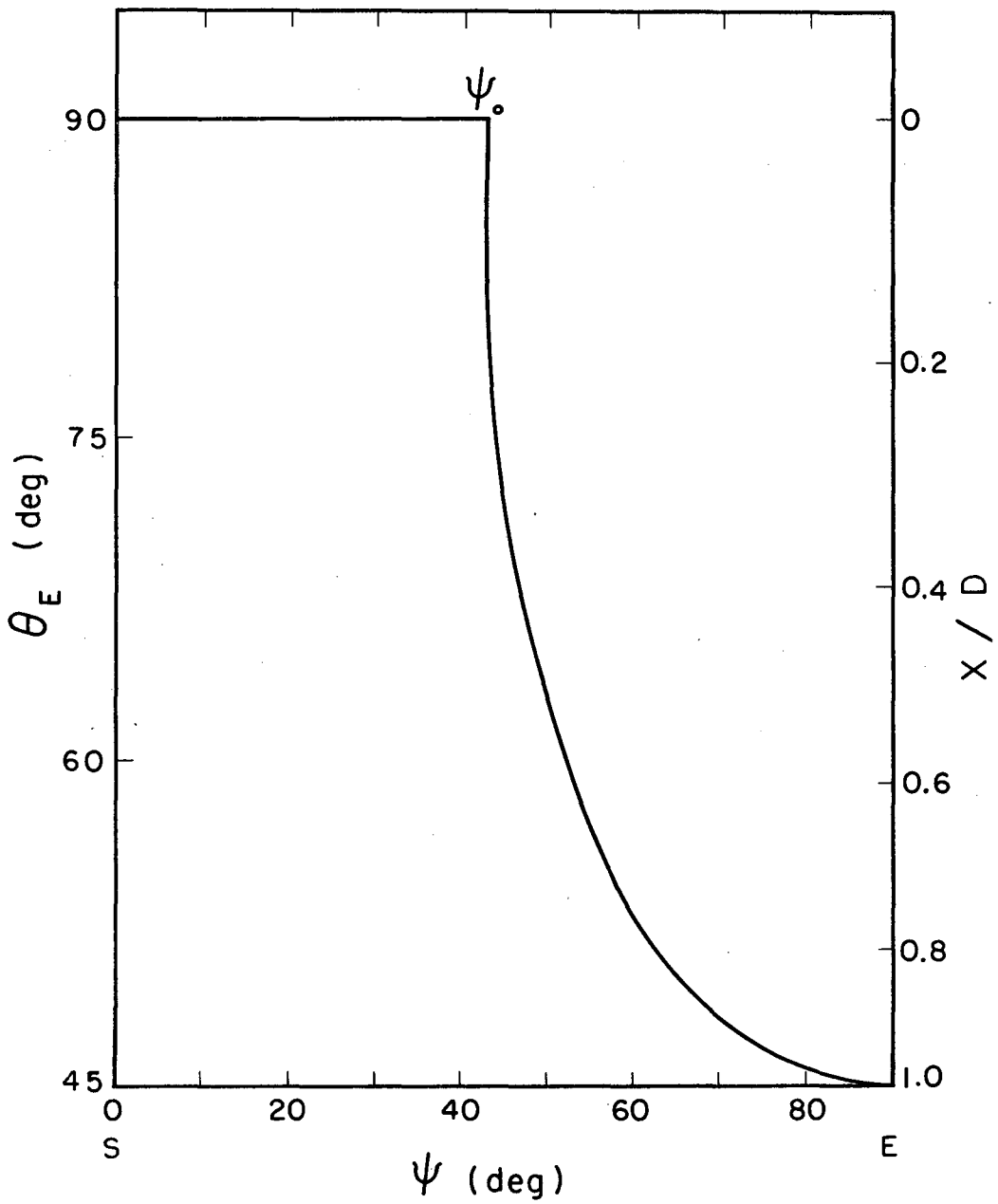
ψ_o
90
75
60
45
θ_E (deg)
0
0.2
0.4
0.6
0.8
1.0
X / D
0
20
40
60
80
S
E
ψ (deg)
MUB-7910

Fig. 1

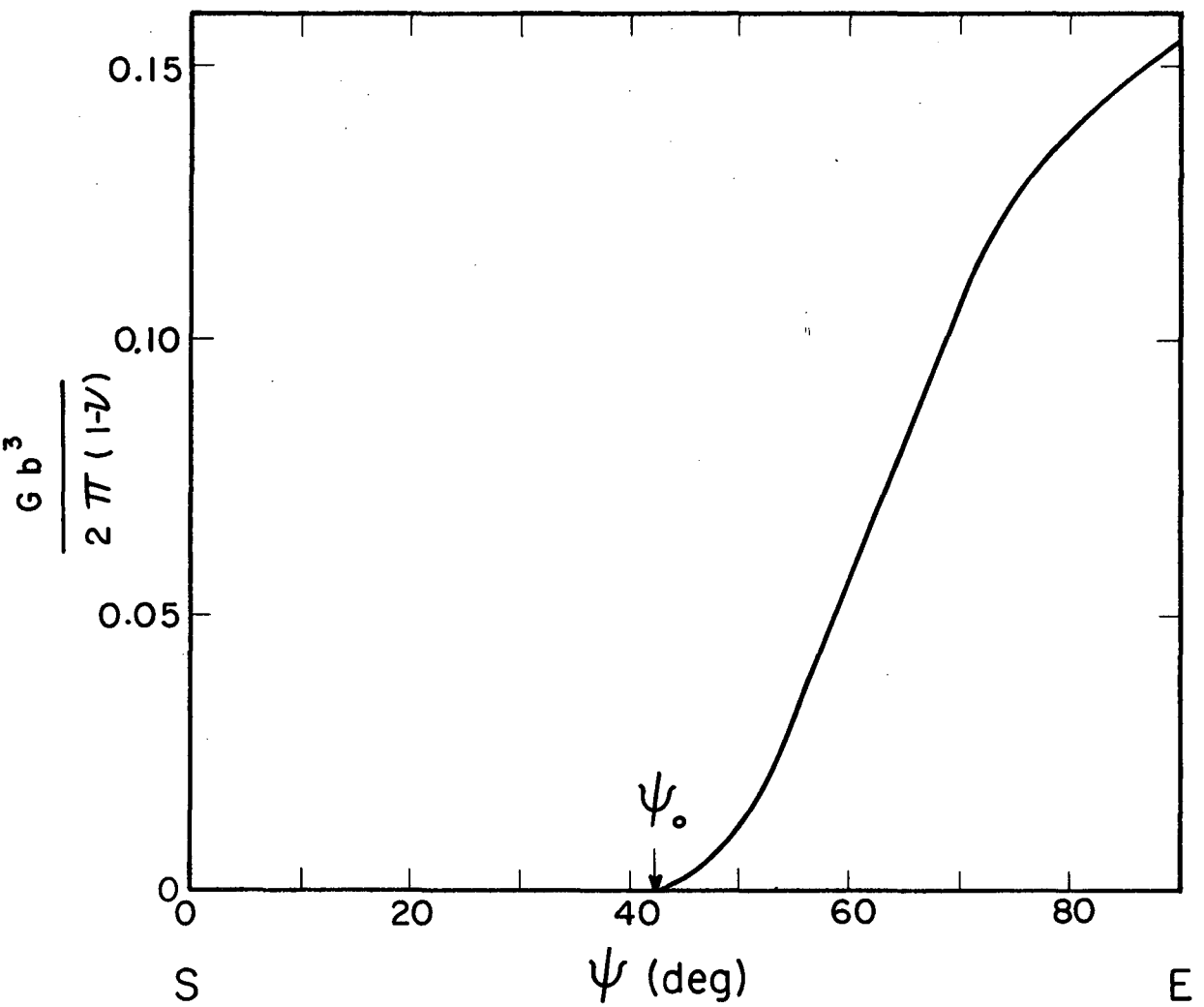
0.15
0.10
0.05
0
$\frac{G b^3}{2\pi(1-\nu)}$
0
20
40
60
80
ψ_o
S
ψ (deg)
E
MUB-7909

Fig. 2

ACKNOWLEDGEMENTS

The author is deeply grateful to Professor Jack Washburn for his quidance, encouragement, and understanding during the course of this research. Thanks are also due to Professors Gareth Thomas and Joseph Pask for several stimulating discussions, Mr. Norman Olson for assistance in carrying out the compression tests, Mr. John Blunden of the Technical Photography Division for the photographic pring work, and Edna Williams of the Mathematics and Computing Division for her patient work in programming the computations.

This work was done under the auspices of the United States Atomic Energy Commission through the Inorganic Materials Research Division of the Lawrence Radiation Laboratory.

REFERENCES

1. J. J. Gilman and W. G. Johnston, Solid State Physics, Vol. 13, Editors F. Seitz and D. Turnbull, Academic Press, New York (1962).

2. J. Washburn, G. W. Groves, A. Kelly, and G. K. Williamson, Phil. Mag., 5, 991 (1960).

3. J. Washburn, Ch. 6, Electron Microscopy and the Strength of Crystals, Editors G. Thomas and J. Washburn, Interscience, New York (1963).

4. C. G. Hulse, S. M. Copley, and J. A. Pask, J. Amer. Ceram. Soc., 46, 317 (1963).

5. J. T. Fourie, Phil. Mag., 10, 1027 (1964).

6. J. J. Gilman, J. Phys. Soc. Japan, 18, Supplement I, 172 (1962).

7. M. F. Ashby and L. M. Brown, Phil. Mag., 8, 1083 (1963); Ibid, 8, 1649 (1963).

8. J. Washburn and A. E. Gorum, Rev. Met., 57, 67 (1960).

9. G. W. Groves and A. Kelly, J. Appl. Phys., 33, Supplement, 456 (1962).

10. W. Bell, M. S. Thesis, University of California, Berkeley, California, UCRL - 16024 (1965).

11. J. Friedel, Dislocations, Pergamon Press, Oxford (1964).

FIGURE CAPTIONS

1. Slip plane section of a crystal deformed at room temperature. Note the deviation from edge orientation of the dipoles, three-fold dipole confluences, and weakly visible dipoles.

   (Note: All slip plane sections are parallel to (110), unless otherwise noted. In all electron micrographs, except Figs. 21 and 22, the black line is parallel to both the active Burgers vector in the plane of the foil and the diffraction vector. It is one micron long, unless otherwise noted).

2. Slip plane section of a crystal deformed at room temperature.

3. Slip plane section of a crystal deformed at room temperature. Very narrow dipoles, attached to a single dislocation in near screw orientation, are denoted by D. Long dipoles, some isolated from the screw dislocation, are at N.

4. Slip plane section of a crystal deformed at 500°C showing long dislocations in predominately screw orientation.

5. Slip plane section of a crystal deformed at 500°C. Note many faint dipole images in central portion of figure.

6. Slip plane section of a crystal deformed at 750°C (dark field). Narrow dipoles are at D. Several of the medium length dipoles have their ends close to edge orientation. Note effect of changing the diffraction conditions on the apparent spacing of the dipoles.

7. Slip plane section of a crystal deformed at 500°C. Dipole junctions where the image changes from inside to outside contrast are at O.

8. Slip plane section of a crystal deformed at 750°C (dark field). As the sense of the Bragg angle deviation is changed, the dipole image at O reverses.

9. Slip plane section of a crystal deformed at 750°C. Two expected dipole junction images are present. The lower dipole may be starting to break up into prismatic loops at its end.
10. Slip plane section of a crystal deformed at 500°C. The sense of the {220} diffraction vector is denoted by the arrow head (dark field).
11. Slip plane section of a crystal deformed at 1000°C. Many long dislocations are apparently emanating from the subboundary.
12. Slip plane section of a crystal deformed at 750°C. Some of the smallest dipoles are at D. A dislocation tangle is beginning to develope where another slip system intersects the plane of the foil.
13. Slip plane section of a crystal deformed at 850°C. Several of the strings of prismatic loops have gaps in the spacing of loops.
14. Slip plane section of a crystal deformed at 1000°C. Many segments of dislocation line have climbed considerably, while others apparently have remained nearly parallel to the plane of the foil.
15. Slip plane section of a crystal deformed at 1600°C. The only stable dislocation pairs remaining in the crystal are quite wide and are accurately in edge orientation. Note the large jogs at J.
16. Dislocation etch pits on a {110} face of a crystal deformed at 600°C with a ratio of stress on the {001} system to the stress on the {110} system with common Burgers vector of 6:1.
17. Slip plane section prepared from crystal shown in Fig. 15.
18. Slip plane section prepared from crystal shown in Fig. 15.
19. Dislocation etch pits on a {110} face of a crystal deformed at 600°C along a loading axis within 2° of <111>.
20. Dislocation etch pits on a {001} face of a crystal deformed 10% at 1300°C along a <111> loading axis. A polygonized substructure develops at these large strains.

21. {001} slip plane section from crystal shown in Fig. 20. Tangles of dislocations and reactions between dislocations with different Burgers vectors are apparent.

22. {001} slip plane section from crystal shown in Fig. 20. A well developed sub-boundary viewed in two different diffracting conditions.

APPENDIX - CHAPTER 2

Fig. 1 Equilibrium angle, θ_E, and lateral spacing $\frac{x}{D}$, as a function of the dipole orientation angle ψ.

Fig. 2 Energy barrier separating the two positions of stable equilibrium as a function of the dipole orientation angle ψ.

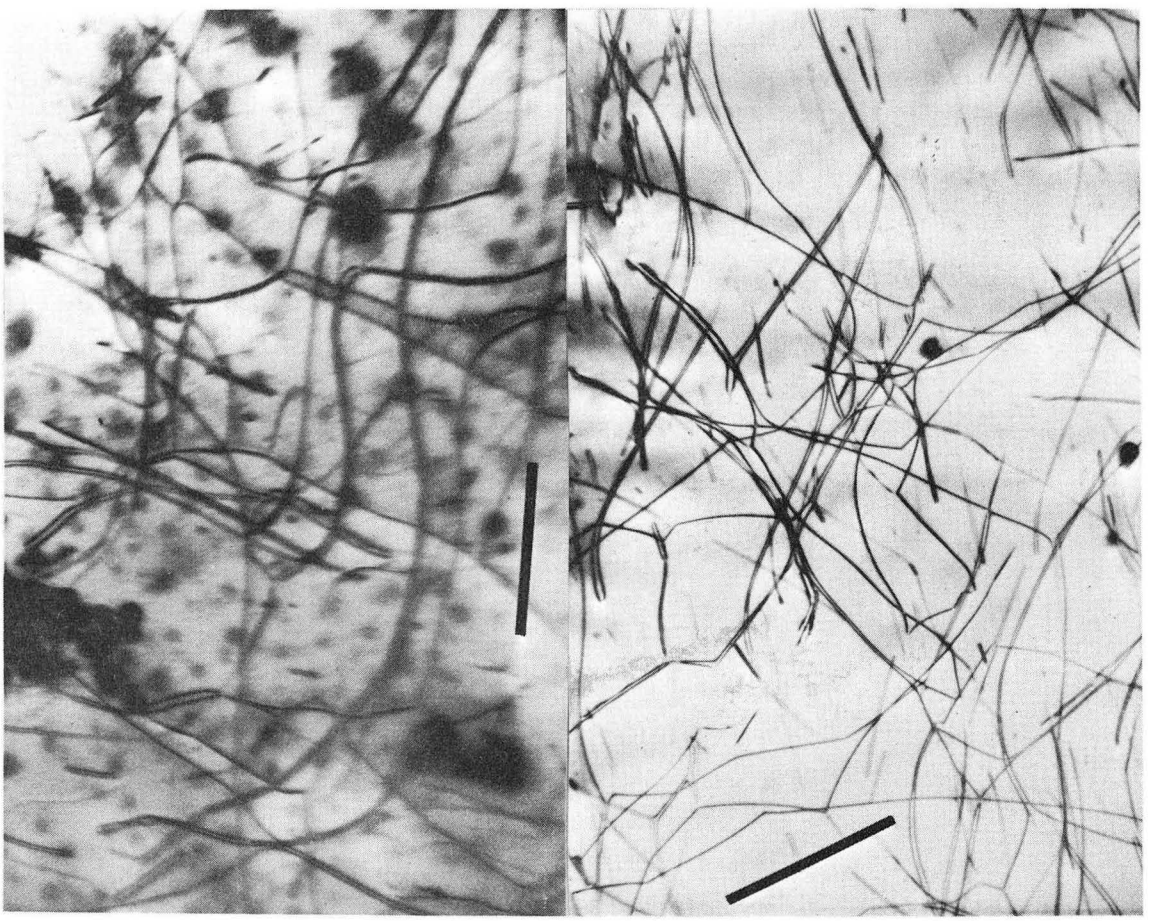

ZN-5330

Fig. 1

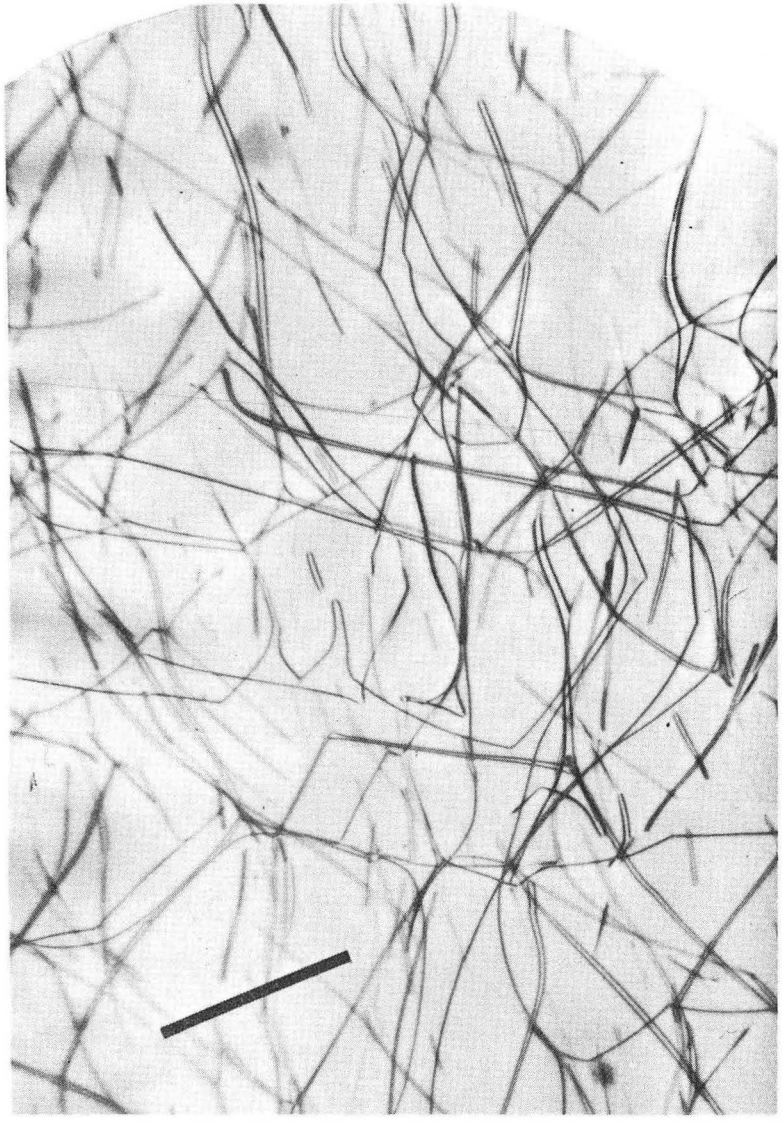

ZN-5331

Fig. 2

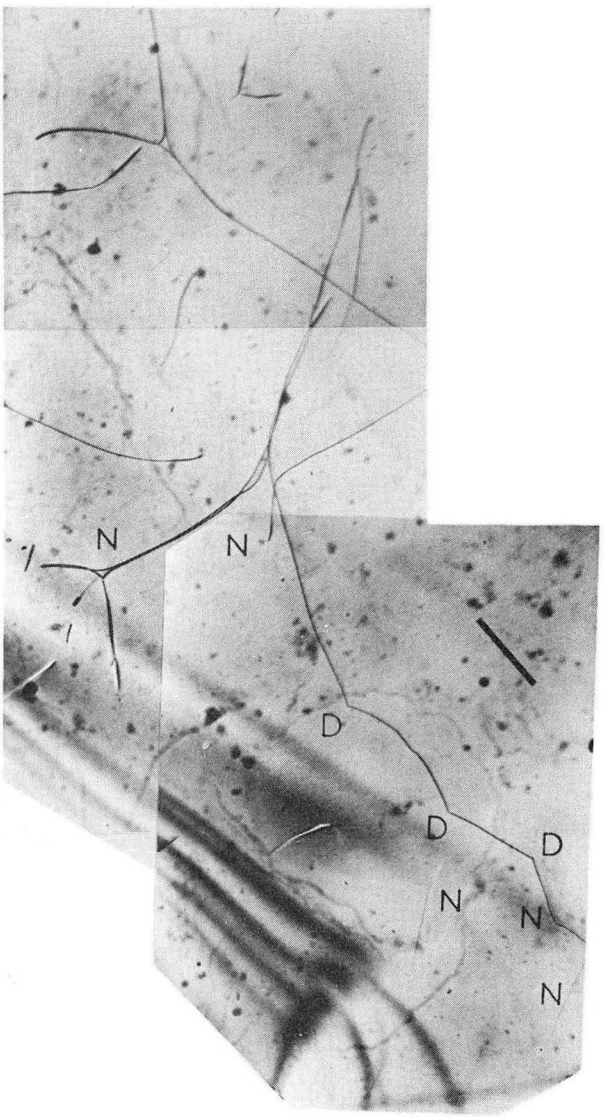

ZN-5332

Fig. 3

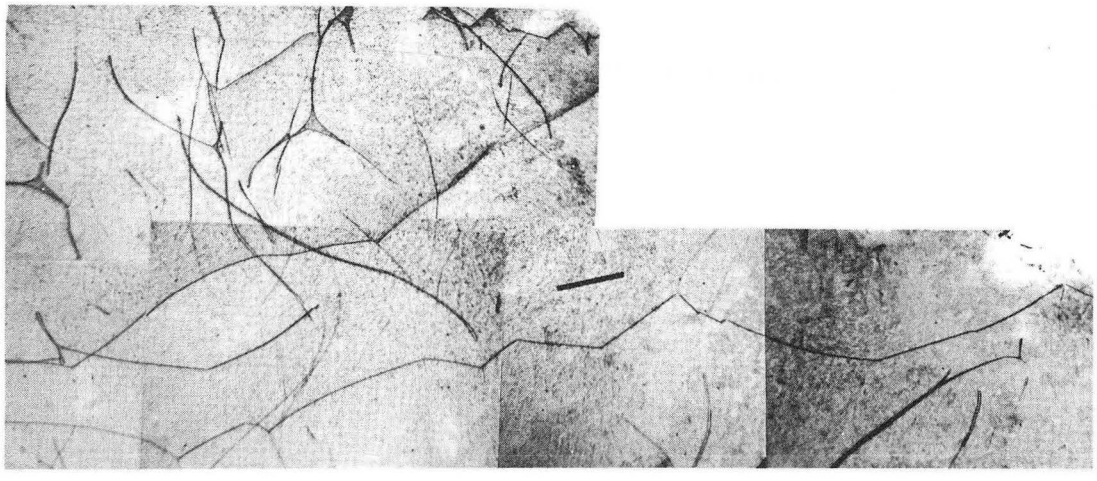

ZN-5333

Fig. 4

ZN-5334

Fig. 5

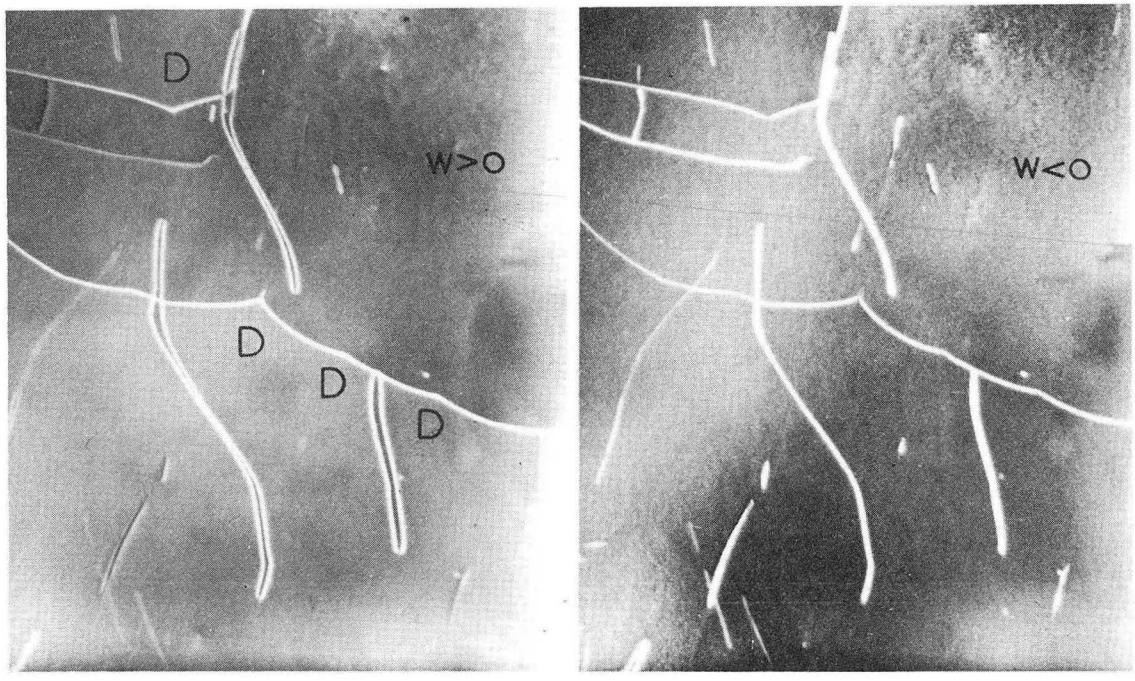

ZN-5335

Fig. 6

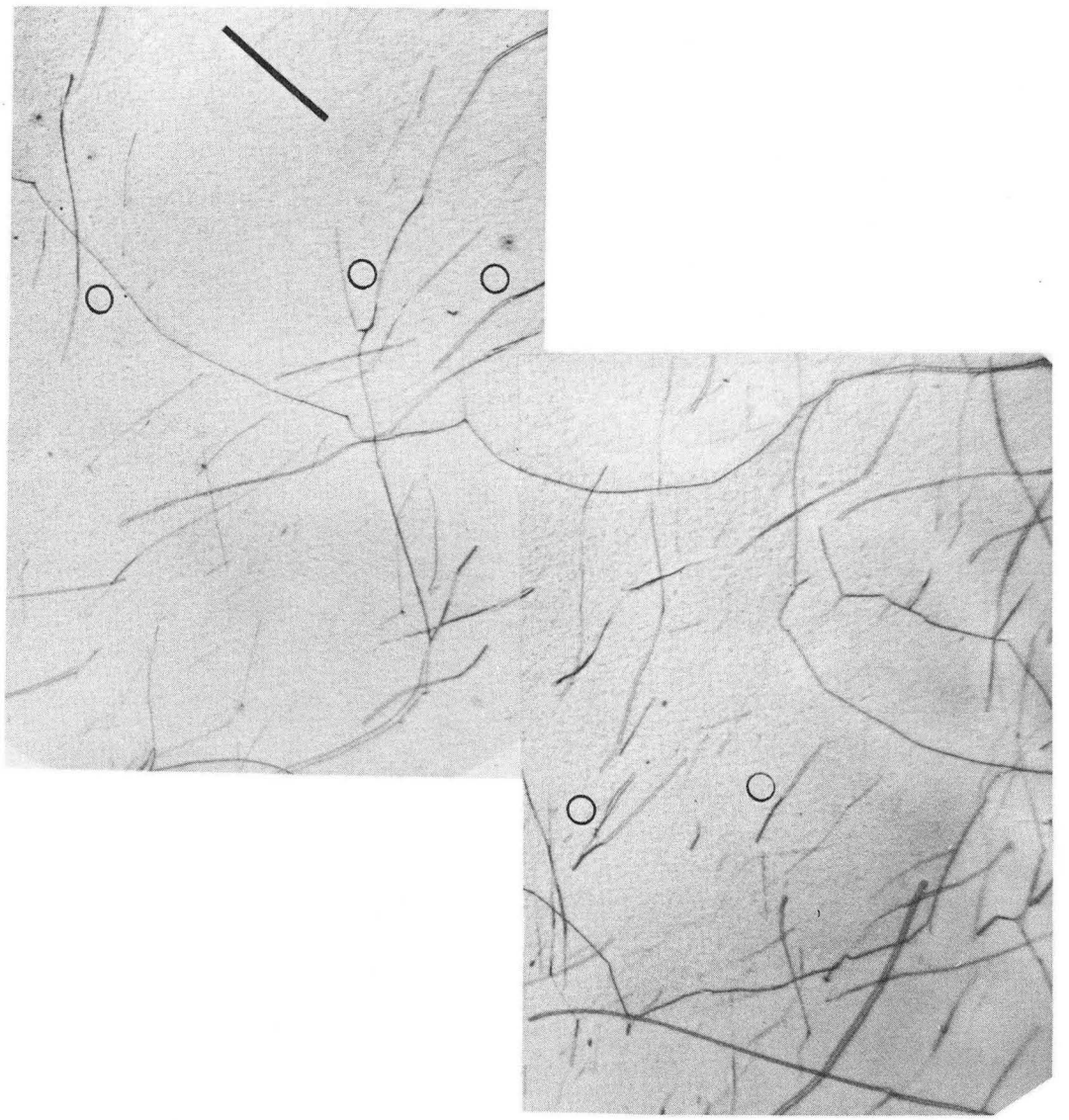

ZN-5336

Fig. 7

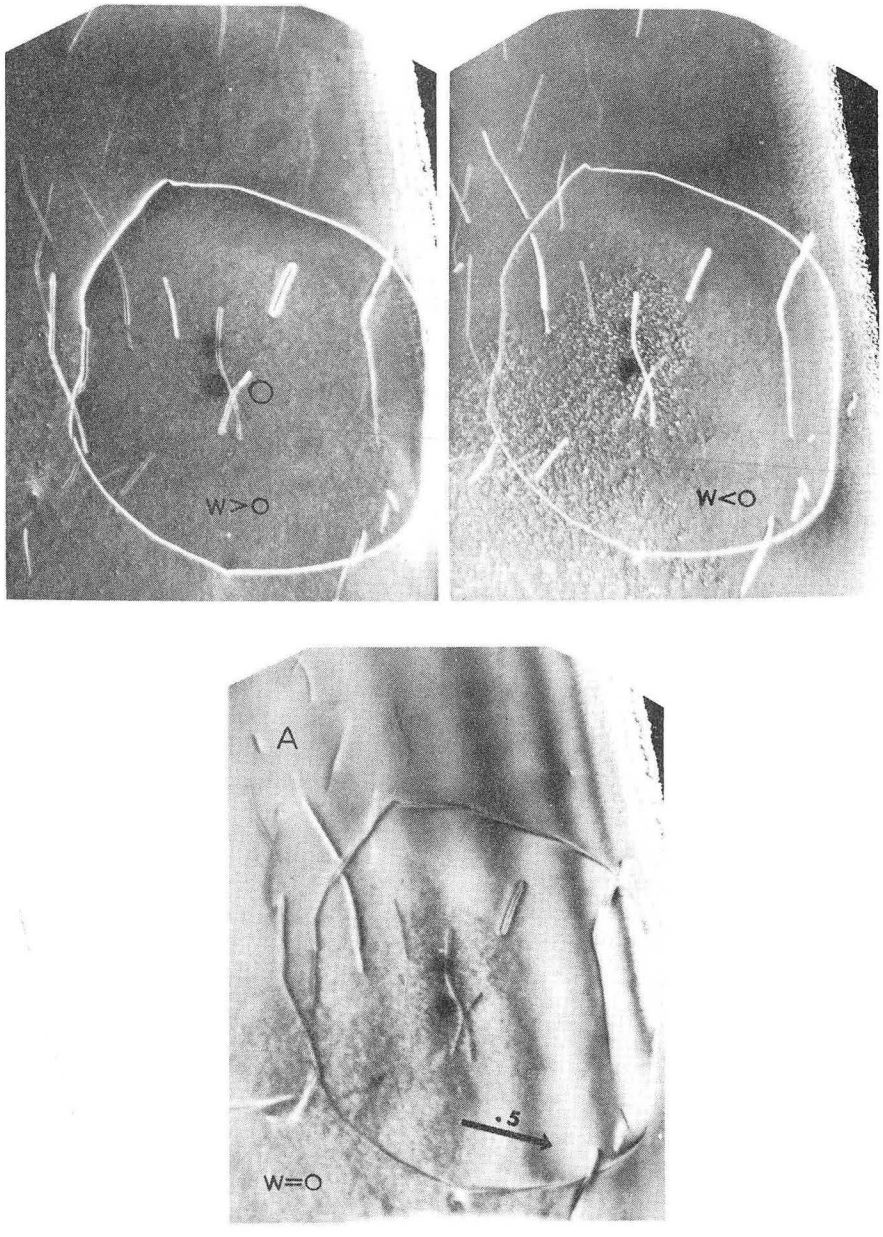

ZN-5337

Fig. 8

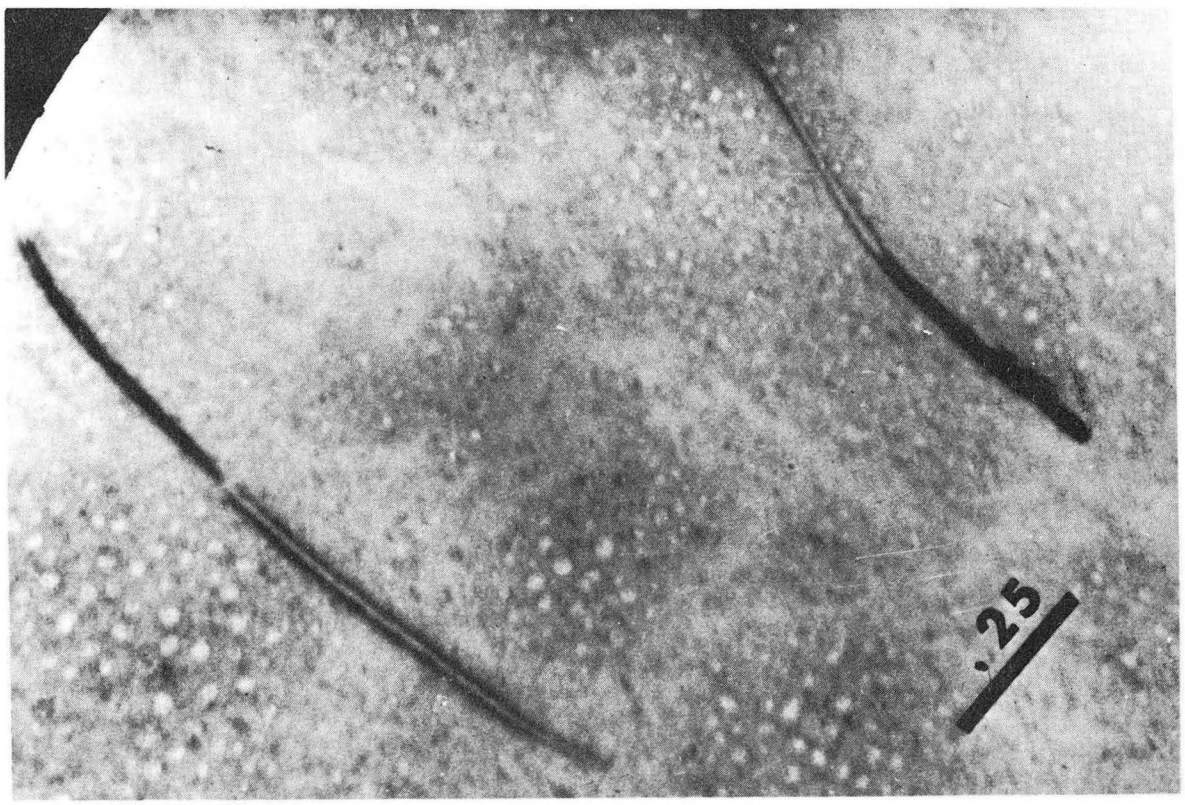

ZN-5338

Fig. 9

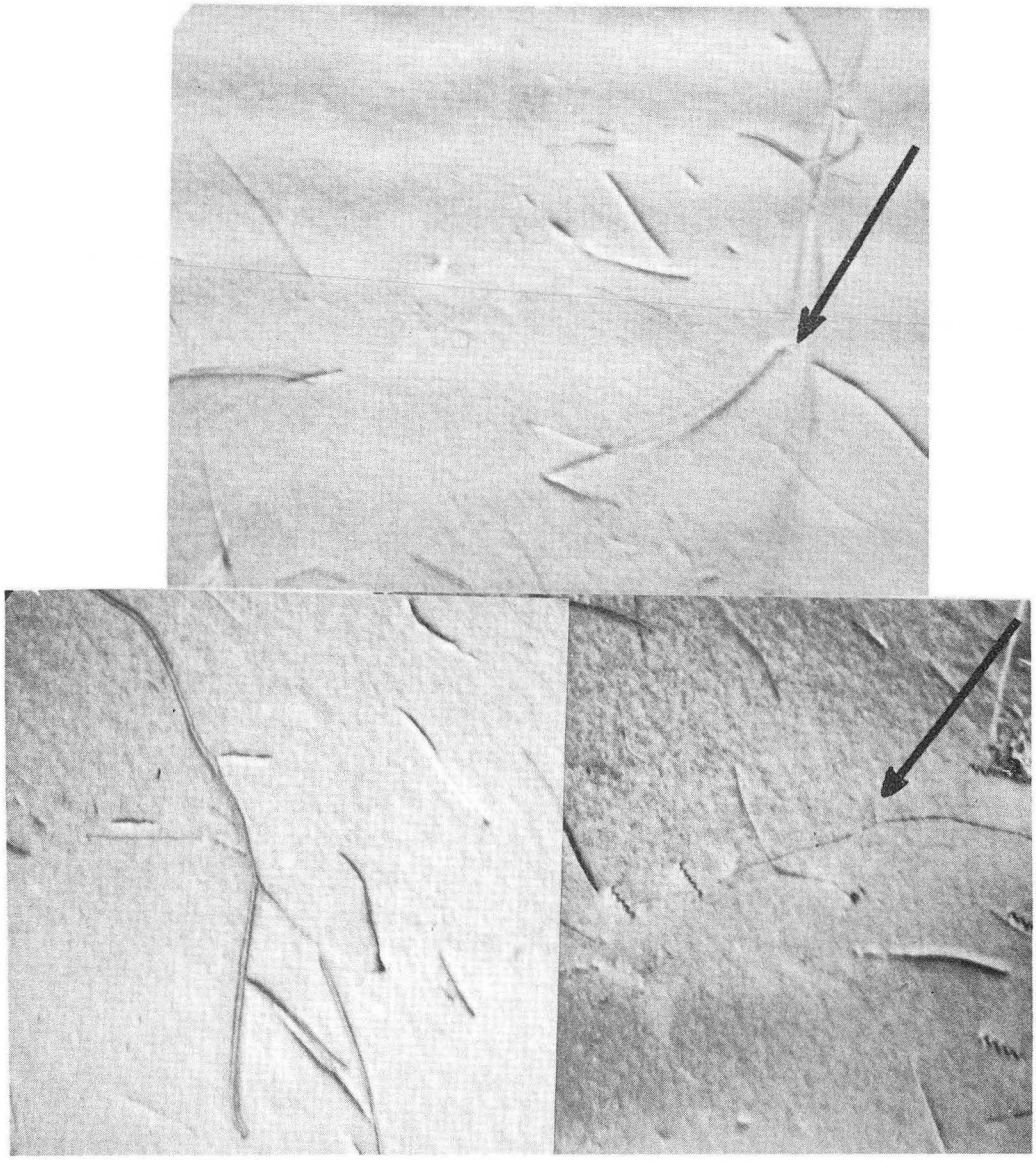

ZN-5339

Fig. 10

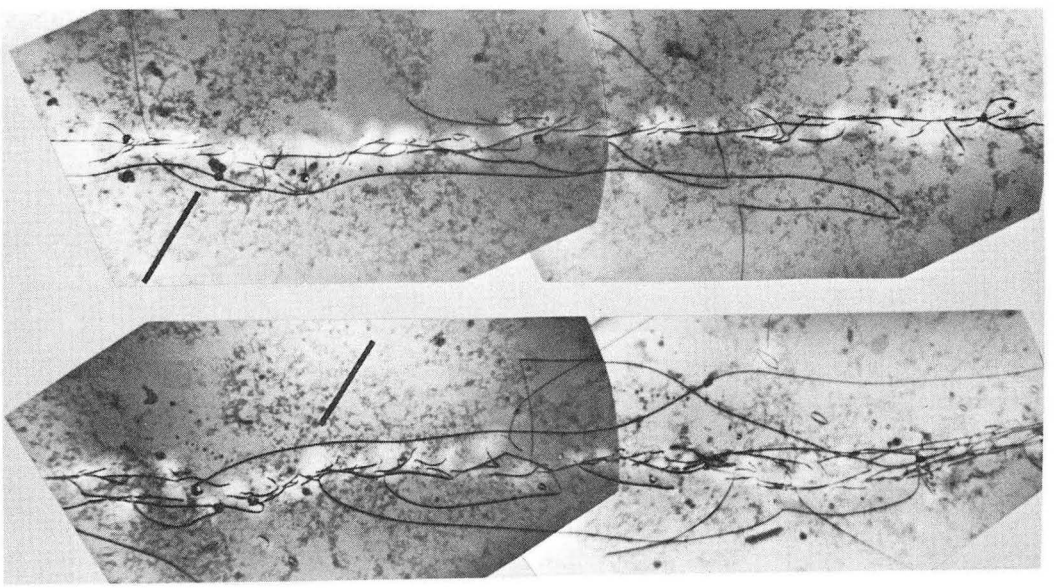

ZN-5340

Fig. 11

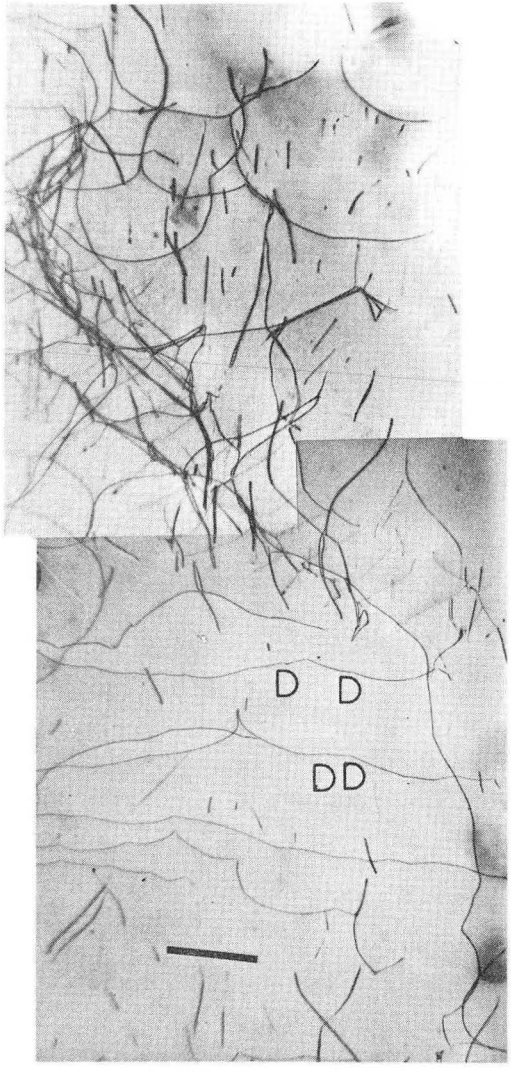

ZN-5341

Fig. 12

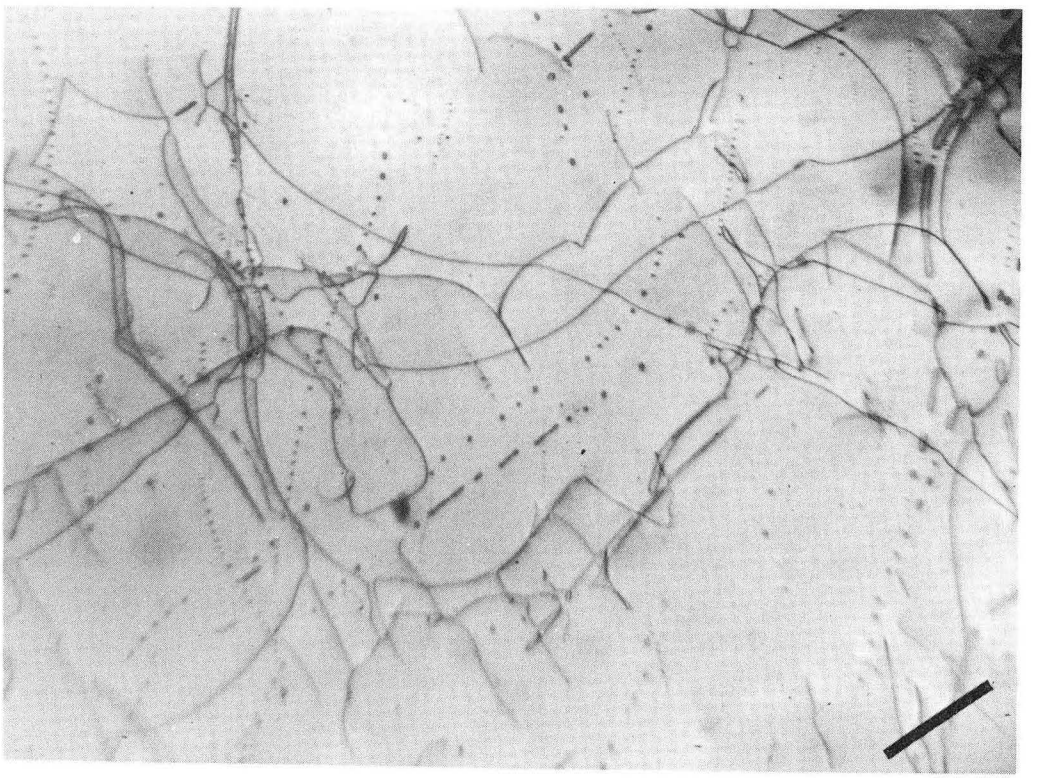

ZN-5342

Fig. 13

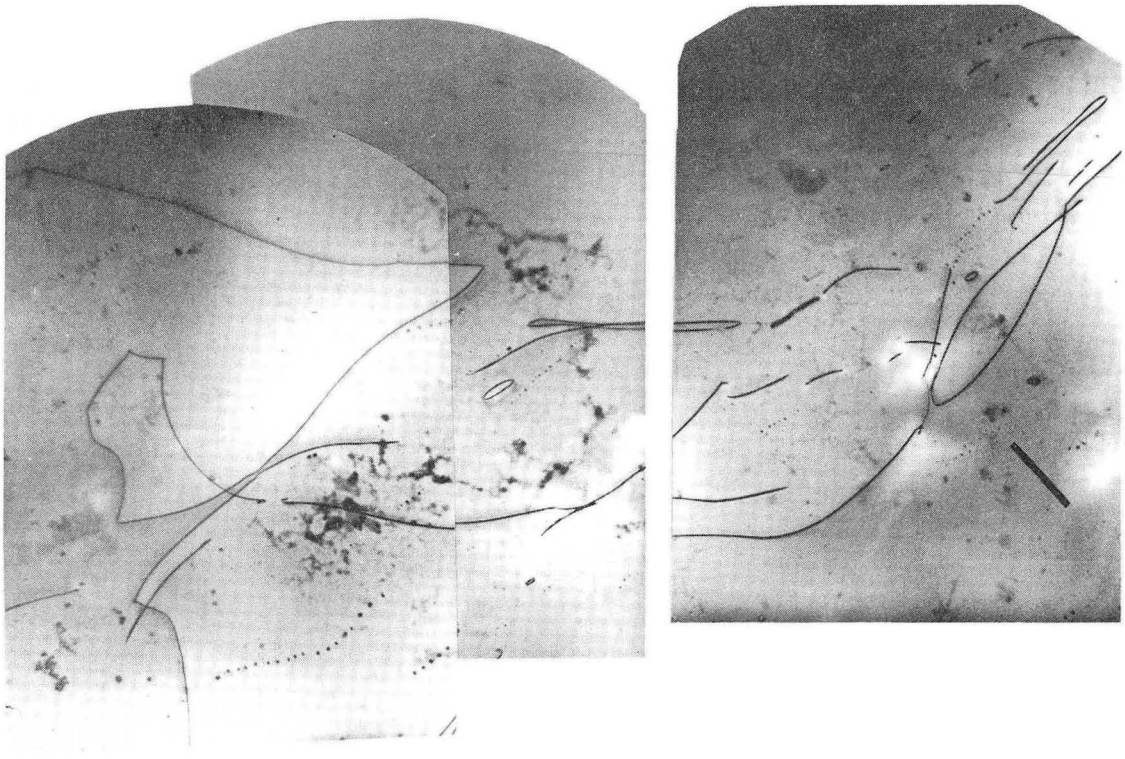

ZN-5343

Fig. 14

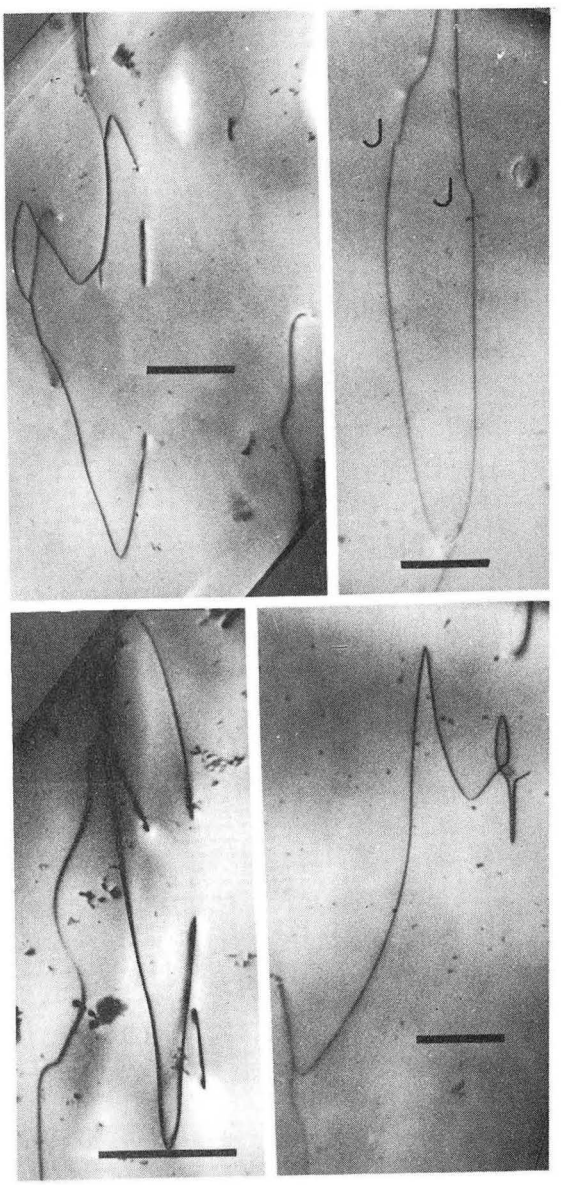

ZN-5344

Fig. 15

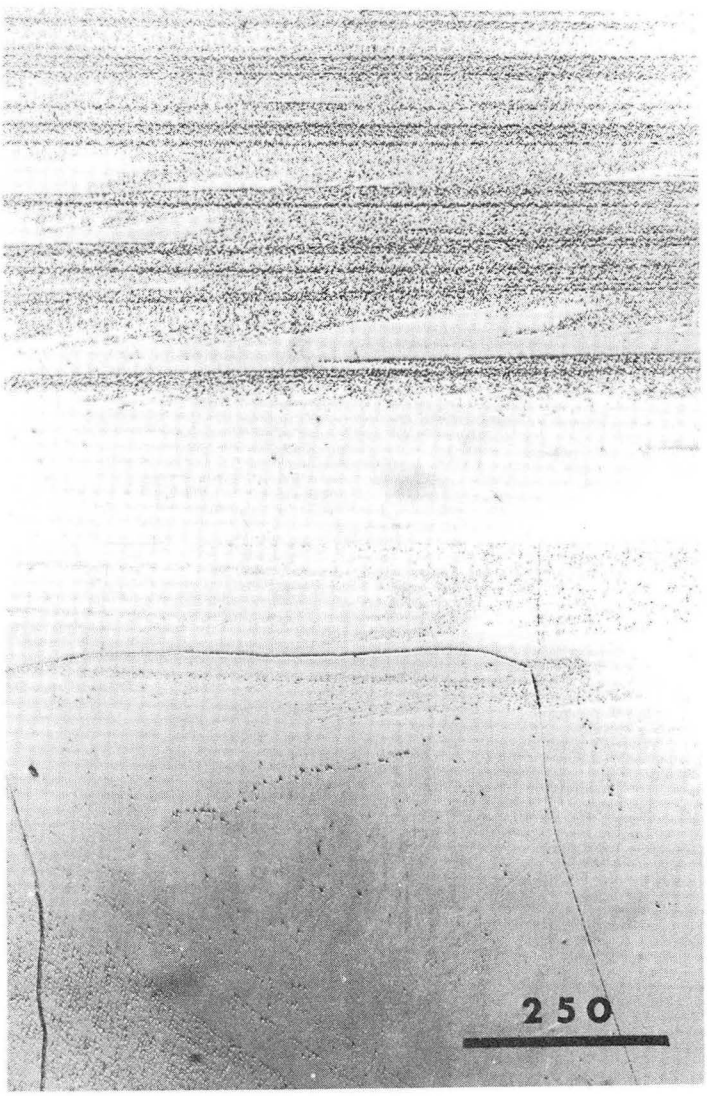

ZN-5345

Fig. 16

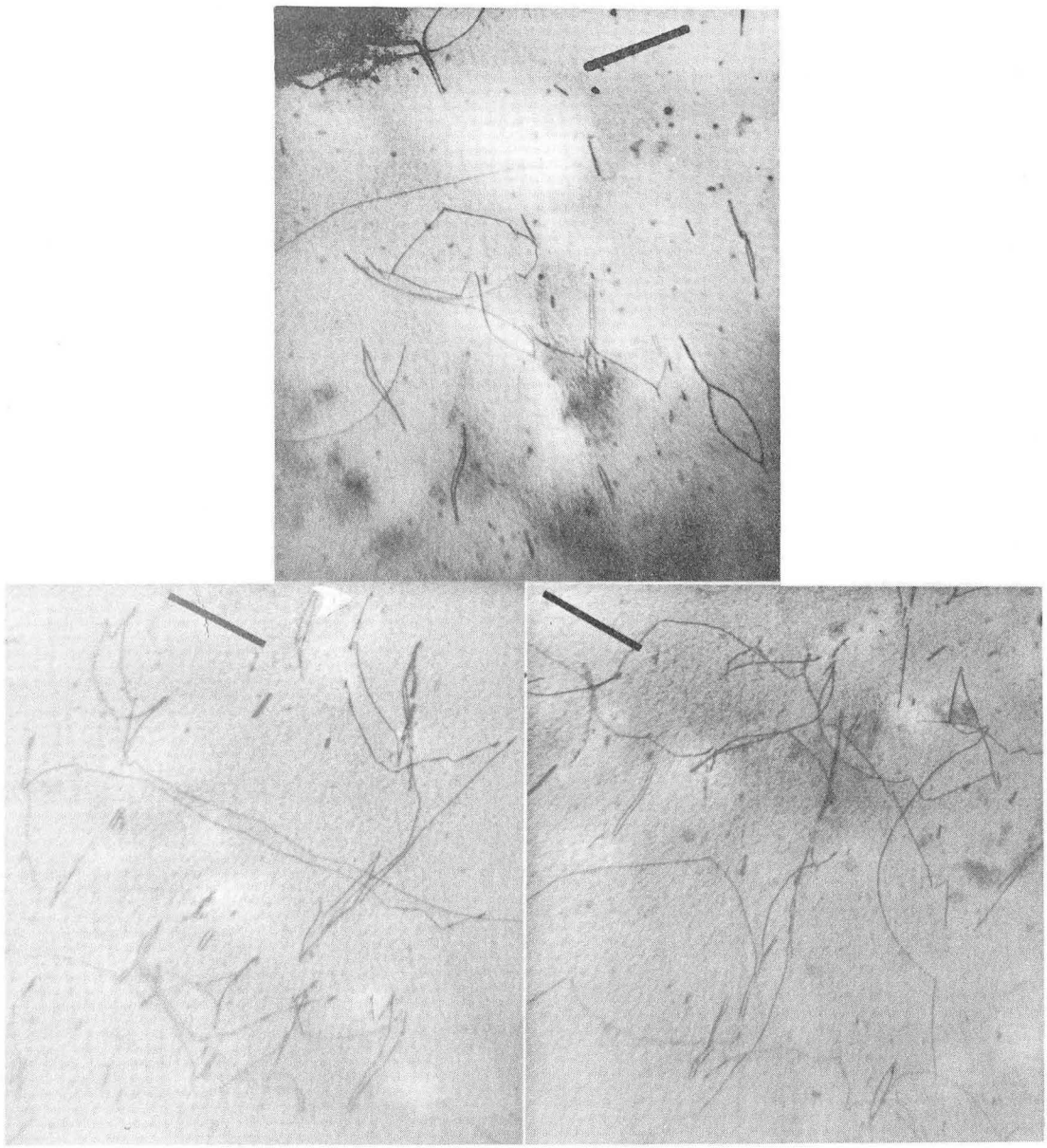

ZN-5346

Fig. 17

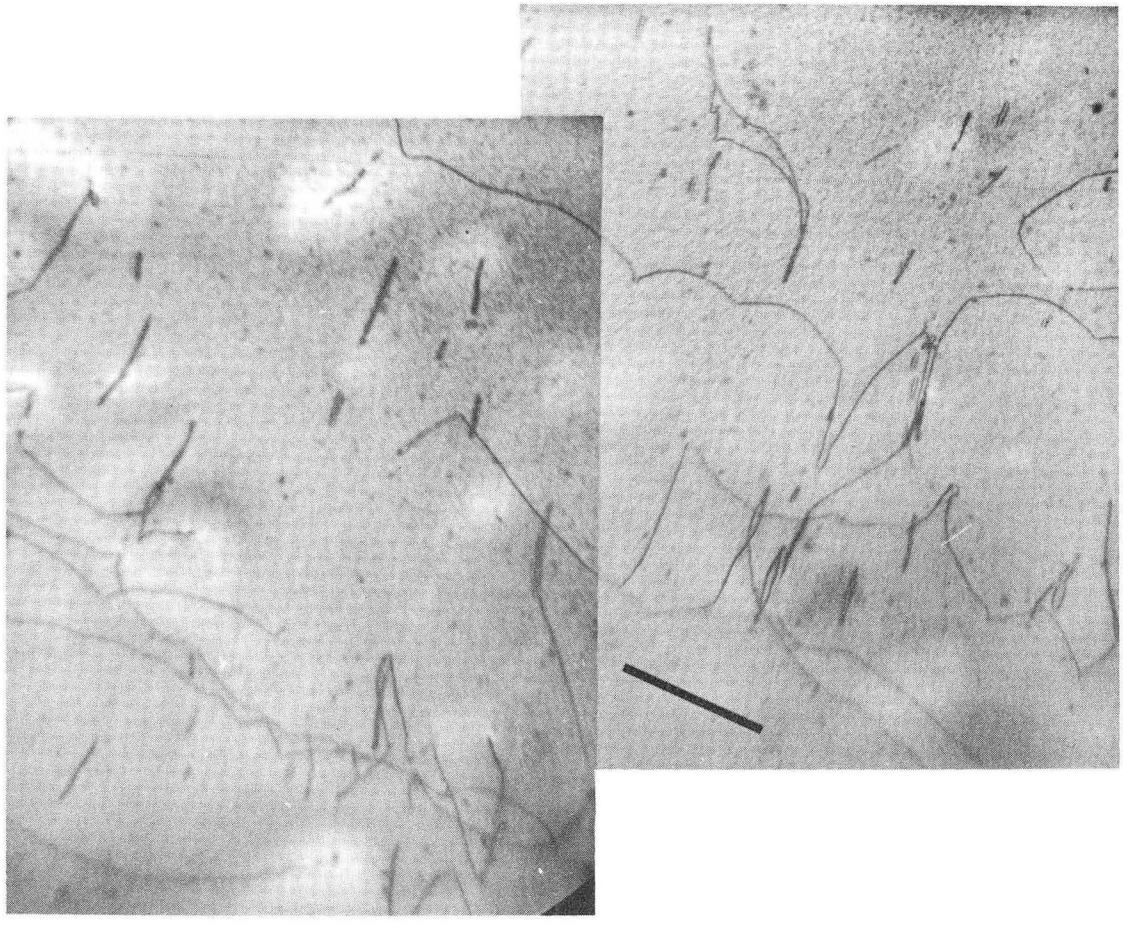

ZN-5347

Fig. 18

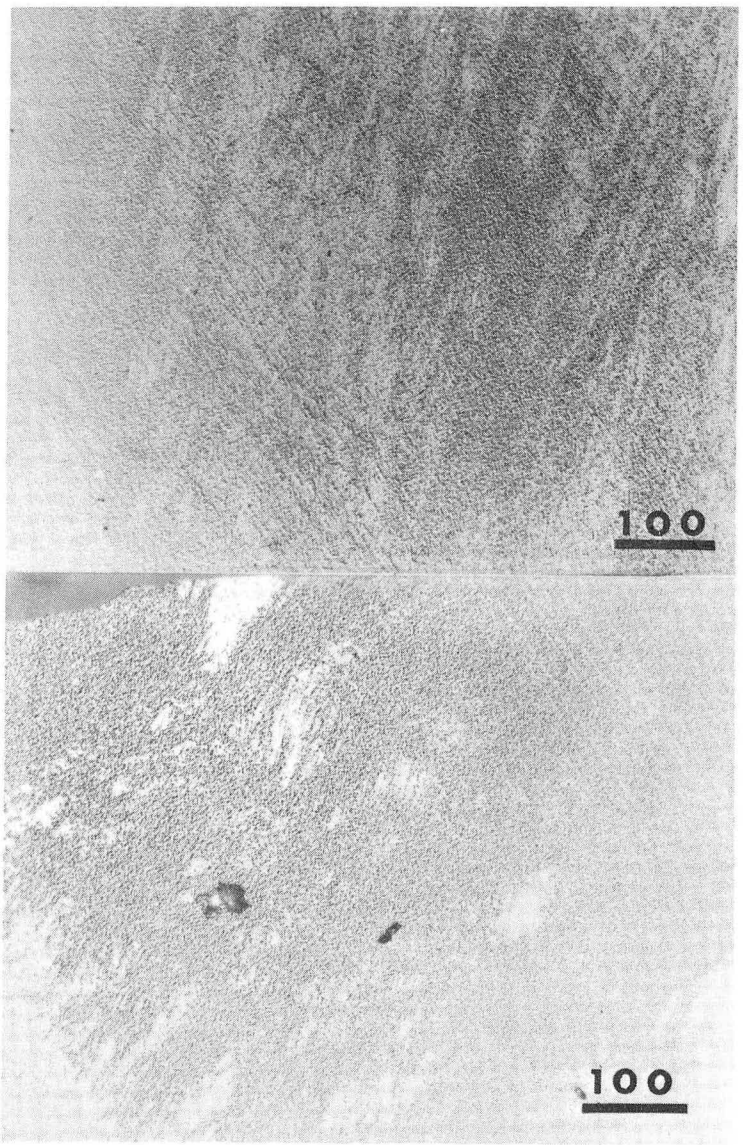

ZN-5348

Fig. 19

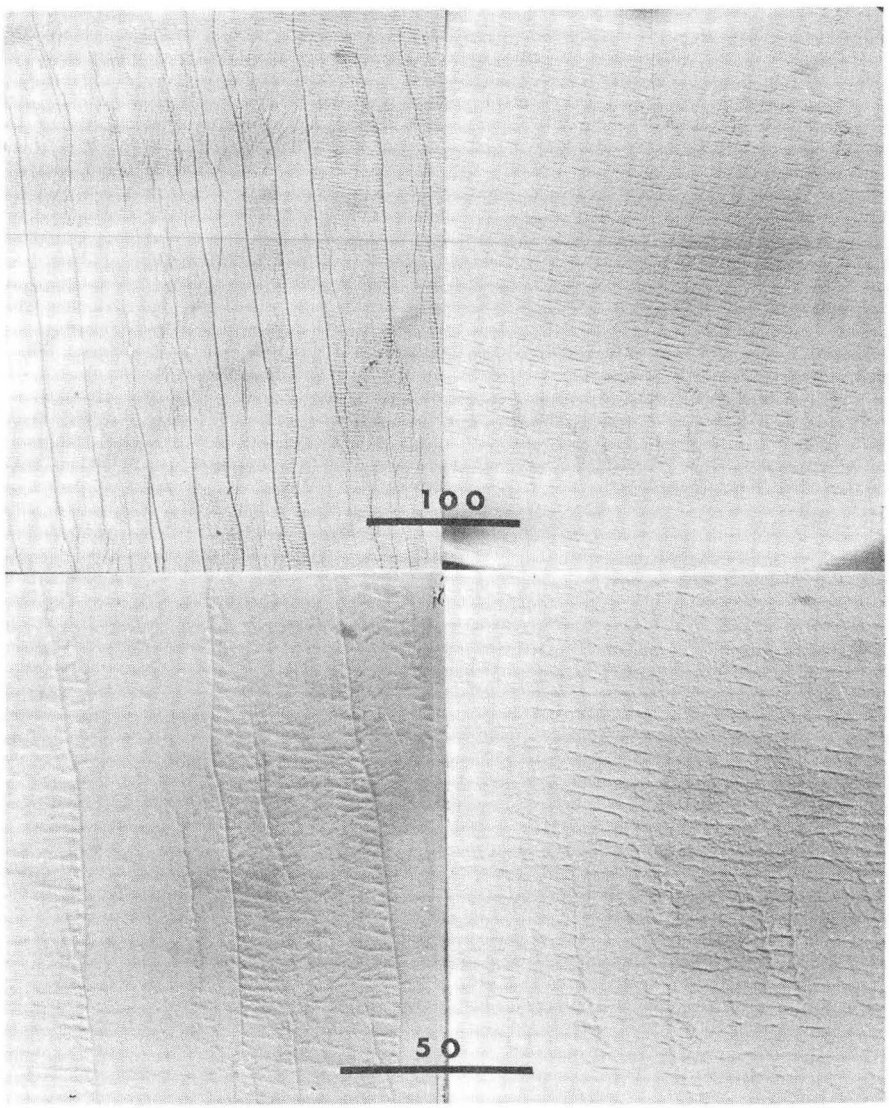

ZN-5349

Fig. 20

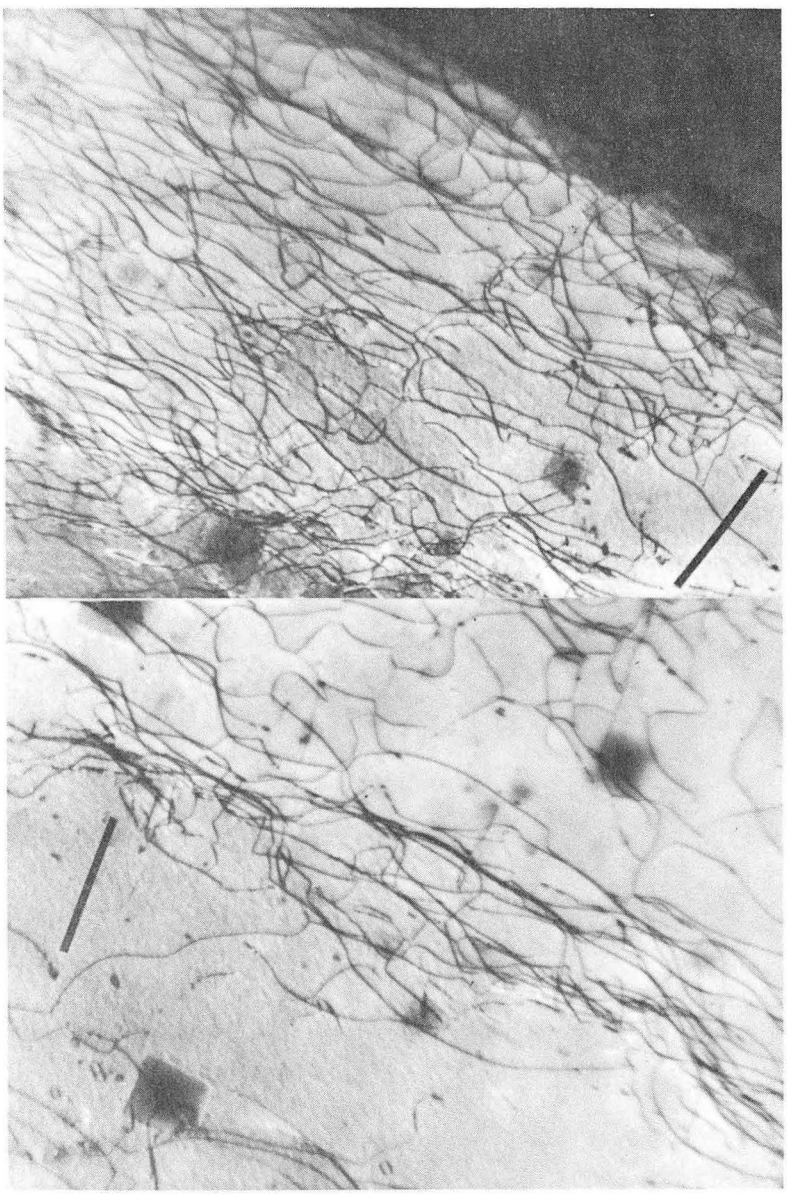

ZN-5350

Fig. 21

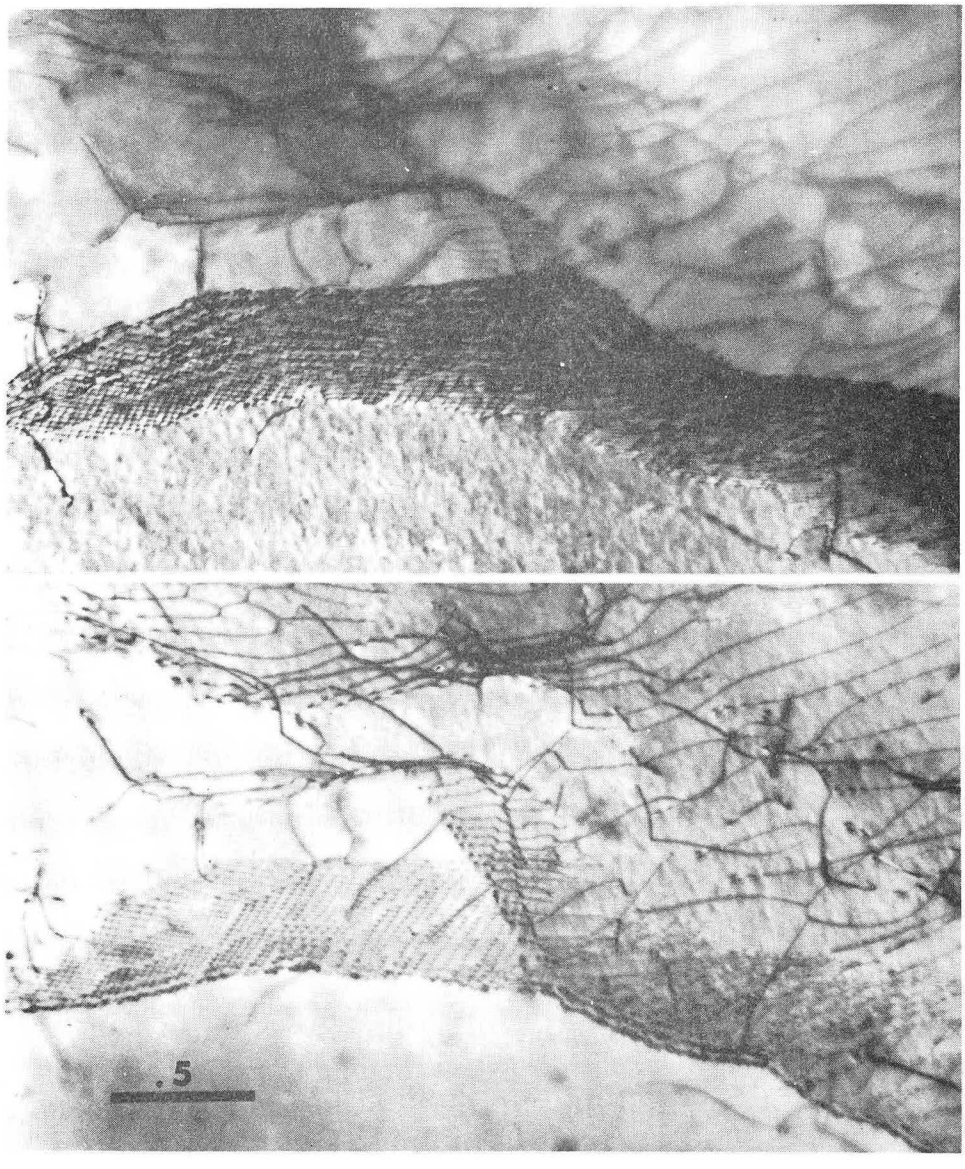

ZN-5351

Fig. 22